ELECTRON TRANSPORT IN SINGLE-MOLECULE TRANSISTORS BASED ON HIGH-SPIN MOLECULES

A Dissertation

Presented to the Faculty of the Graduate School

of Cornell University

in Partial Fulfillment of the Requirements for the Degree of

Doctor of Philosophy

by

Jacob Ebenstein Grose

August 2007

© 2007 Jacob Ebenstein Grose

ALL RIGHTS RESERVED

ELECTRON TRANSPORT IN SINGLE-MOLECULE TRANSISTORS BASED ON HIGH-SPIN MOLECULES

Jacob Ebenstein Grose, Ph.D.

Cornell University 2007

In this dissertation, I will focus on the magnetic properties of single-molecule transistors. Of the two types of high-spin molecules I used in these devices, one has a high degree of magnetic anisotropy while the other is roughly isotropic. Devices made from each of these types of molecules exhibit distinctive transport characteristics. I will also discuss side-projects involving electrochemical techniques.

After reviewing the molecular electronics literature and explaining some experimental methods, I will discuss the theory of Coulomb blockade in single-molecule transistors based on anisotropic single-molecule magnets along with simulations of electronic transport in such devices. I will present low-temperature measurements of transistors made using single-molecule magnet (Mn_{12}) complexes. While both the experimental and simulated transport spectra show signatures of magnetism, including signs of magnetic anisotropy, the experimental spectra do not exhibit hysteresis in low-bias experiments as predicted by the simulations. Possible reasons for this discrepancy are explored.

I will also discuss low-temperature measurements made on transistors based on the high-spin endofullerene, $N@C_{60}$. Conductance spectra from these devices show two signatures of isotropic magnetism. First, the ground-state spin of the molecule in the device changes as a function of applied magnetic field. Second,

excited-state conductance peaks terminate in other excited-state peaks, as opposed to terminating in ground-state peaks as is common in non-magnetic spectra.

In addition to experiments involving single-molecule transistors, I report that the electrical conductance between closely-spaced gold electrodes in acid solution can be turned from off to on to off again by monotonically sweeping a gate voltage applied to the solution in a way that mimics polyaniline transistors, and I present an electrochemical synthesis of alkali-doped-C_{60} superconductors which may lead to the creation of new fullerene superconductors. Ideas for future experiments will also be presented.

BIOGRAPHICAL SKETCH

Jacob Ebenstein Grose was born in New York City (the Bronx) on April 30, 1979. A few months later, he decided that he was too tough for that town and moved to the rough-and-tumble suburb of Irvington, NY. It was there that he won one of the most coveted awards in all of science, the "Regents rock," given to the most promising eighth-grade Earth science student in the Irvington public school system. After graduating from Irvington High School as valedictorian in 1997, he moved on to the green pastures of Harvard University. It was while singing in the Harvard-Radcliffe Collegium Musicum that he met Maya, whom he married in 2002. Despite having attended the Aspen Music School in music composition for a number of summers, Jacob, like many disaffected youths of his era, chose to study physics in college. During his time at Harvard, Jacob benefited from the patience of David Goldhaber-Gordon, who kindly put up with his assistant's ignorance while teaching him the basics of nanofabrication. Sustained by many late night runs to Tommy's House of Pizza, Jacob graduated *magna cum laude* in 2001. That summer, he and Maya traveled to Cornell University where Jacob joined Dan Ralph's group in the physics department. Six years later, Jacob was tempted to accept a postdoc in solid-state chemistry, but he realized that he was spending too much time following the stock market to pursue a career in academic science. After obtaining his Ph.D. in the summer of 2007, Jacob will be looking for a job in finance.

To Maya, for her love and support.

ACKNOWLEDGEMENTS

My doctorate in experimental physics was much more about struggling with leaky dilution fridges and painfully separating real data from experimental artifacts than about the thesis contained in these pages. To the extent that I was successful in my Ph.D., my success was due to the many people who have supported me, both professionally and personally, during my brief scientific career, and it is a pleasure to thank them all here.

First of all, I would like to thank my advisor, Dan Ralph. In addition to supporting me and my research, you have always shown faith in me as a scientist, even at those times when things in lab were not going well. I will forever count myself fortunate to have worked for such a rigorous experimenter who also has the insight to grasp the greater significance of any experiment.

During my graduate career, nobody has been more supportive of me than Héctor Abruña. You have always made me feel like one of your own students, and your inspiring enthusiasm for our research flowed from you during every encounter we had. I have learned so much through my time with your group that has shaped the way I think about science, and I know countless more students will benefit from your espresso-fueled passion in the future.

I want to thank my committee, particularly Piet Brouwer who has always patiently provided answers to any theoretical questions I could come up with. Thanks to Jim Sethna for agreeing to proxy my B-exam. Thanks to George Malliaras for his constant encouragement, to Rich Galik and Don Holcomb for teaching me how to teach physics, and to Keith Schwab and Dave Lee for making H-corridor such a friendly place. I also want to thank David Goldhaber-Gordon for putting up with me as an undergrad and helping guide me to Dan's group.

Thanks to Mandar and Ed for starting the Ralph group off on the right foot, and to Alex Corwin for making the basement seem much less intimidating. Thanks to Jason and Abhay for pulling me up from the depths of ignorance. You two are so different and yet so brilliant; I am in awe of both of you. Thanks to Alex Champagne for thoughtful and entertaining discussions, to Kirill for his artistic style and warm personality, to Jack for keeping group meetings fun and to Ferdinand for his constant experimental advice and general engineering mastery. Thanks to Josh for keeping me abreast of current events; I might have completely lost track of Paris Hilton if it weren't for our ping-pong games. Thanks to Eugenia for being both an ideal collaborator and a hardcore NBA fan. Thanks to Sufei for his insights on China and to Kiran and Yongtao for being great labmates. Thanks also to the Ralph group postdocs, especially Sergey and Janice, and to all the undergrads who helped me, especially Radek and Jane.

When I think back on the projects that I've most enjoyed during my time at Cornell, they were all done in equal collaboration with Burak Ülgüt. I have learned a tremendous amount about chemistry (and about Turkey) from our work together. You have been a great friend, and I wish you the best of luck in England and beyond. Thanks to Geoff Hutchison, who has always been able to put my wild conjectures on firm theoretical footing. Pittsburgh is lucky to have you. Many additional thanks to the rest of the Abruña group including Jay, Yasu, Samuel, Jamie and Jing for accepting me as a surrogate labmate.

Thanks to John Read for being a truly remarkable person. Some of my best times in Ithaca were spent talking with you about science or art or music or current events or, most commonly, all of the above. I also enjoyed the dinners with you, Pat and Yuanjia. Thanks to Ethan Bernard for great conversations, to Jeff and Yulong

from the Malliaras group for help early on, to Sara and John from the van Dover group for helping us with the SQUID, to Stephan Braig for help with theoretical simulations and to Jiwoong, Markus, Xinjian, Nathan and all the members of the McEuen group who have helped me along the way.

Thanks to my collaborators outside of Cornell, including Moon-Ho Jo, Hongkun Park, Jeff Long, Evan Rumberger, David Hendrickson, Carsten Timm, Michael Scheloske and Wolfgang Harneit.

The staff at Cornell are some of the nicest, most helpful people one could hope to meet. Thanks to Eric Smith for countless pieces of low-temperature wisdom, to Mick Thomas for helping me with the SEM and to Dave Wise for making so many glass pieces for us. Thanks to Monica Plisch for organizing the CIPT program. Thanks to Stan and the pro shop guys for machining so much for me, to John Sinnott, Ron Kemp and Jon Shu for helping me with the facilities and to Win, Bobby and the research service guys for keeping the basement running so smoothly. Thanks also to Deb Hatfield and the administrative staff for making Cornell physics the most organized place I have ever worked and to Douglas Milton for helping me track down rogue professors.

Thanks to Anne and Zhen for many enjoyable times in Ithaca and to Michael McGuire for being a great classmate during our first year. Tremendous thanks to Omar Nazem for being a great friend and for goading me into my new career path. Thanks to my cousins, to my sister and to oma and opa for their love and support. Thanks to my parents for putting up with my many calls home and for all the love and advice along the way. Finally, thanks and love to Maya who warmed both Ithaca and me with her spirit when we were at our most cold and desolate.

TABLE OF CONTENTS

Biographical Sketch iii

Dedication iv

Acknowledgements v

List of Figures xi

List of Abbreviations xiii

1 Introduction 1
- 1.1 Perspective . . . 1
- 1.2 Molecular electronics . . . 2
  - 1.2.1 Nomenclature . . . 2
  - 1.2.2 Metal complexes and clusters . . . 3
  - 1.2.3 π-conjugation . . . 5
  - 1.2.4 Molecular materials I: metals and superconductors . . . 6
  - 1.2.5 Molecular materials II: semiconductors and magnets . . . 9
- 1.3 Single-molecule electronics . . . 11
  - 1.3.1 A word of caution . . . 12
  - 1.3.2 Scanned-probe experiments . . . 14
  - 1.3.3 Mechanical break junctions . . . 16
  - 1.3.4 Transistor geometries . . . 17
- 1.4 Single-molecule transistors made via electromigration . . . 17
  - 1.4.1 Electromigrated break junctions . . . 17
  - 1.4.2 Vibration-assisted tunneling . . . 18
  - 1.4.3 The Kondo effect in single-molecule transistors . . . 19
- 1.5 Organization of this thesis . . . 20

References 21

2 Nanofabrication and experimental details 25
- 2.1 Overview of fabrication . . . 25
- 2.2 Thin (10nm) wires . . . 29
- 2.3 Platinum vs. gold wires . . . 32
- 2.4 Characteristics of molecules that will lead to successful experiments 33
- 2.5 Depositing the molecules . . . 35
- 2.6 Low-temperature measurements . . . 38

References 42

3 Theory of Coulomb blockade in a single-molecule transistor based on a single-molecule magnet 43
3.1 Theory of Coulomb blockade in single-molecule transistors 43
3.1.1 Definitions and assumptions 44
3.1.2 Ground state transitions 48
3.1.3 Excited state transitions 52
3.2 Theory of single-molecule magnets 55
3.2.1 Magnetic characteristics 57
3.2.2 Hamiltonian and zero-field splitting 59
3.2.3 Hysteresis and quantum tunneling of the magnetization . . . 60
3.3 Simulations of Coulomb blockade in single-molecule magnets 63
3.3.1 Assumptions related to tunneling rates 64
3.3.2 Transition rates via Clebsch-Gordon coefficients 65
3.3.3 Steady-state simulations of magnetic randomization and anisotropy 69
3.3.4 Iterative simulations of hysteresis and magnetic relaxation via tunneling 73

References 80

4 Coulomb blockade in single-molecule transistors based on single-molecule magnet (Mn_{12}) compounds 81
4.1 Introduction 81
4.2 Control experiments, deposition and electromigration 82
4.3 Zero-field splitting and possible *in situ* degradation of Mn_{12} 84
4.4 Anisotropy 89
4.5 No observation of hysteresis 89
4.6 Other phenomena 91

References 95

5 Coulomb blockade in single-molecule transistors based on the high-spin endofullerene, $N@C_{60}$ 96
5.1 Introduction 96
5.2 Negative controls, deposition and electromigration 100
5.3 Changes in ground-state spin at high fields 101
5.4 Signatures of isotropic magnetism at zero-field 110
5.5 Other conductance peaks that intersect the ground state 111
5.6 Summary 115

References 116

6 Side projects: electrochemical experiments in molecular electronics 117
6.1 Gold nanoparticles mimicking polyaniline transistors 117
6.1.1 Acid-gated polyaniline transistors 118
6.1.2 Transistor behavior via gold nanoparticles 120
6.2 Electrochemical synthesis of fullerene superconductors 126
6.2.1 Theory 127
6.2.2 Experiment 131

References 138

7 Future directions 140
7.1 Hysteresis in single-molecule transistors based on single-molecule magnets 140
7.2 Ferromagnetic electrodes in N@C_{60}-based single-molecule transistors 141
7.3 Optical experiments 141

References 146

LIST OF FIGURES

1.1 Examples of metal complexes 4
1.2 Superconducting alkali-doped fulleride crystal 8
1.3 Examples of semiconducting and magnetic organic molecules 10
1.4 Experimental techniques in single-molecule electronics 15
1.5 Vibration-assisted tunneling and the Kondo effect in SMTs 19

2.1 Schematic of lithography 26
2.2 Schematic and SEM images of nanowires 28
2.3 SEM images of failed attempts at thin wires 30
2.4 SEM images of thin Pt wires before and after electromigration . . . 31
2.5 Breaking curves of 10 nm and 16 nm gold wires 32
2.6 Breaking curves of 10 nm gold and platinum wires 34
2.7 Schematic of deposition process 36
2.8 Photographs of mounted chip and dilution refrigerator 38
2.9 Schematic of measurement setup 39

3.1 Single-electron transistor circuit diagram 44
3.2 Energy scales in a single-molecule transistor 45
3.3 Toy model illustrating charging energy and level spacing 47
3.4 Example of "quantum" Coulomb blockade 48
3.5 Cartoon of electron transport in a single-electron transistor 49
3.6 Simulation of ground-state transport in a single-molecule transistor 51
3.7 Cartoon of excited states in a single-molecule transistor 53
3.8 Simulation of excited states in a single-molecule transistor 54
3.9 Deducing the energy of an excited state 56
3.10 Structure of $Mn_{12}Ac$ 57
3.11 Magnetization of single-molecule magnet crystals during cooling . . 59
3.12 Mn_{12} energy-level diagram 60
3.13 Thermal relaxation of the magnetization in single-molecule magnets 61
3.14 Quantum tunneling of the magnetization in $Mn_{12}Ac$ crystals 62
3.15 Simulation of zero-field splitting in Mn_{12} tunneling spectra 70
3.16 Cartoon of magnetic randomization in a Mn_{12} single-molecule transistor 72
3.17 Simulation of anisotropy in Mn_{12} tunneling spectrum 73
3.18 Iterative simulations of Mn_{12} tunneling spectra 76
3.19 Explanation of the disappearance of hysteresis at high biases . . . 77
3.20 Iterative simulations at various field angles 78

4.1 Conductance plots of zero-field splitting in Mn_{12} tunneling spectra 85
4.2 Conductance plot of magnetic anisotropy in Mn_{12} tunneling spectrum 88
4.3 Low-bias tunneling current measurements and simulation 90
4.4 "Reverse" zero-field splitting in Mn_{12} tunneling spectra 92
4.5 High field suppression of low energy peaks in Mn_{12} tunneling spectrum 93

5.1 Cyclic voltammograms of N@C_{60} and C_{60} 98
5.2 Schematic diagram of an N@C_{60} single-molecule transistor 100
5.3 Conductance plots illustrating a change of spin of the ground state 102
5.4 Theory of the change of spin of the ground state 104
5.5 Low-energy states in Carsten's model 107
5.6 Conductance plots illustrating ETE peaks 109
5.7 Energy diagrams explaining ETE peaks 112

6.1 Schematic of acid-gated break junction 119
6.2 Plots of current vs. source and gate voltages in solution-gated transistors 121
6.3 SEM images of a break junction before and after voltage cycling in acid 124
6.4 Crystal structure of alkali-doped fullerene superconductors 128
6.5 Variation of T_c with lattice parameter a_o for alkali-doped fullerene superconductors 130
6.6 "Shake-and-bake" synthesis of alkali-doped fullerene superconductors 132
6.7 Cyclic voltammogram of C_{60} in dichloromethane 133
6.8 Schematic of proposed electrochemical synthesis of alkali-doped fullerene superconductors 133
6.9 UV-vis absorbance spectra of alkali-doped fullerenes 136

7.1 Optical setup 142
7.2 Photographs of ice build-up in the optical cryostat 144

LIST OF ABBREVIATIONS

6T	sexithiophene
AC	alternating current
ADC	analog to digital converter
AFM	atomic force microscope (or microscopy)
Alq_3	tris(8-hydroxyquinoline) aluminum
bct	body-centered tetragonal (lattice)
BEEM	ballistic electron emission microscope (or microscopy)
BNC	bayonet Neill Concelman (connector)
CNF	Cornell NanoScale Science & Technology Facility
DAC	digital to analog converter
DC	direct current
DFT	density functional theory
EDX	energy dispersive X-ray
EELS	electron energy loss spectroscopy
EPR	electron paramagnetic resonance
ETE	excited-state [peaks] terminating in excited-state [peaks]
fcc	face-centered cubic (lattice)
FET	field-effect transistor
HOMO	highest occupied molecular orbital
HP	Hewlett-Packard
LUMO	lowest unoccupied molecular orbital
MBJ	mechanical break junction
Mn_{12}	a class of single-molecule magnet compounds with the chemical structure: $Mn_{12}O_{12}(O_2C\text{-}R)_{16}(H_2O)_4$
$Mn_{12}Ac$	a Mn_{12} compound where R = CH_3
$Mn_{12}Cl$	a Mn_{12} compound where R = $CHCl_2$
MRI	magnetic resonance imaging
NDR	negative differential resistance
NMP	N-methylpyrrolidone
NMR	nuclear magnetic resonance
OFET	organic field-effect transistor
OLED	organic light-emitting diode
PANI(-CSA)	polyaniline (doped with camphor sulfonic acid)
Ph	phenyl (ligand)
PTCDI	perylene-3,4,9,10-tetracarboxylic diimide
QD	quantum dot
QTM	quantum tunneling of the magnetization
SAM	self-assembled monolayer
SECM	scanning electrochemical microscope (or microscopy)
SEM	scanning electron microscope (or microscopy)
SET	single-electron transistor
SMA	subminiature version A (connector)

SMM	single-molecule magnet
SMT	single-molecule transistor
SQUID	superconducting quantum interference device
STM	scanning tunneling microscope (or microscopy)
TCNE	tetracyanoethylene
TCNQ	7,7′,8,8′-tetracyanoquinodimethane
TEM	transmission electron microscope (or microscopy)
TMTSF	tetramethyltetraselenafulvalene
TTF	tetrathiafulvalene
UV/vis	ultraviolet-visible (spectroscopy)
XPS	X-ray photoelectron spectroscopy

Chapter 1

Introduction

1.1 Perspective

This year marks the 60^{th} anniversary of the discovery of the transistor by Shockley, Bardeen and Brattain in 1947. In almost every electronic device built since that time, active components such as transistors and diodes have been made from inorganic semiconductors, usually crystalline silicon. The main reason for this is that silicon-based devices work really well, i.e. they are very reliable under a wide range of environmental conditions. When one considers that silicon is also relatively inexpensive and easy to process, it is no wonder that silicon-based electronic devices can be found in every country in the world.

A crystal of silicon (like any covalently-bonded single crystal or alloy) has two natural length scales: its macroscopic dimensions and its atomic dimensions. Polycrystalline inorganic materials (including the metals found in many passive electronic components) have an additional level of structure: grain size. However, this grain size often varies within a single material and can be as large as several millimeters. Molecular materials, on the other hand, have a well defined substructure on the *molecular* scale. It follows that "molecular electronics" refers to a class of electronic components with a well-defined substructure on the molecular scale, through the use of molecular materials or single molecules.

So why study molecular electronics when inorganic semiconductors and metals dominate the technologies of today? One answer is that scientists are always looking for the technologies of tomorrow. While most knowledgeable people do not

believe that molecular electronics will ever completely replace conventional electronics, there are many niche applications where molecular electronic devices can compete on such factors as cost or customized characteristics. However, the main motivation behind the work presented in this thesis is that the field of molecular electronics is fascinating as basic science. The electronic properties of molecular materials often have entirely different physical origins than those of conventional materials. Single-molecule electronics teaches us about the quantum mechanics of current flow through the smallest of objects: a single molecule. Although molecular electronics-based devices may never be as ubiquitous as those based on silicon, there is still a great deal to learn.

1.2 Molecular electronics

1.2.1 Nomenclature

As mentioned in the last section, the term "molecular electronics" refers to a class of electronic components with a well-defined substructure on the molecular scale. But what do I mean when I say "well-defined substructure"? For the purposes of this thesis, I will require that the substructure 1) not be covalently bonded to other identical substructures and 2) have a chemical formula with a definite number of atoms. I feel these requirements are necessary to preserve a "molecular" character, even though they exclude devices based on two important materials in carbon nanoelectronics, graphene and carbon nanotubes, since neither can be represented by a chemical formula with a definite number of atoms. Although graphene and nanotubes have respectively one and two nanoscale dimensions, there is a sense in which these materials are no more "molecules" than a single-crystal silicon wafer is.

Similarly, devices based on long chain conducting polymers are excluded (although conducting polymer oligomers, such as sexithiophene (6T), still fall under this definition). Devices based on metal clusters will be considered, provided that every cluster has a well defined number of atoms (Au_{16}^- clusters as opposed to Au nanoparticles with a given diameter).

Now that I have defined what I mean by "molecular electronics," I will divide the field into two categories. The first category consists of devices made from molecular materials—materials with a well-defined substructure on the molecular scale. Molecular materials can be either van der Waals or ionic crystals, but in most commercial devices they are amorphous films. The second category, single-molecule electronics, refers to electronic devices in which the active element is a single molecule. These devices will be reviewed in Section 1.3.

The molecules that form the basis of molecular electronics devices are diverse, but most of them fall into one of two categories: 1) metal complexes and clusters and 2) π-conjugated molecules. Each of these categories will be discussed in the subsections below. The physical and device properties of molecular materials formed from these molecules will be discussed in Subsections 1.2.4 and 1.2.5.

1.2.2 Metal complexes and clusters

Metal complexes (see Figure 1.1) are molecules formed by the combination of ligands and metal ions. Metal clusters are one category of metal complexes consisting of molecules containing three or more metal atoms. While strictly speaking metal clusters must contain two or more direct metal-metal bonds, in much of the literature the term is used to describe any molecule with more than two metal atoms, and this will be the definition that I will use in this thesis.

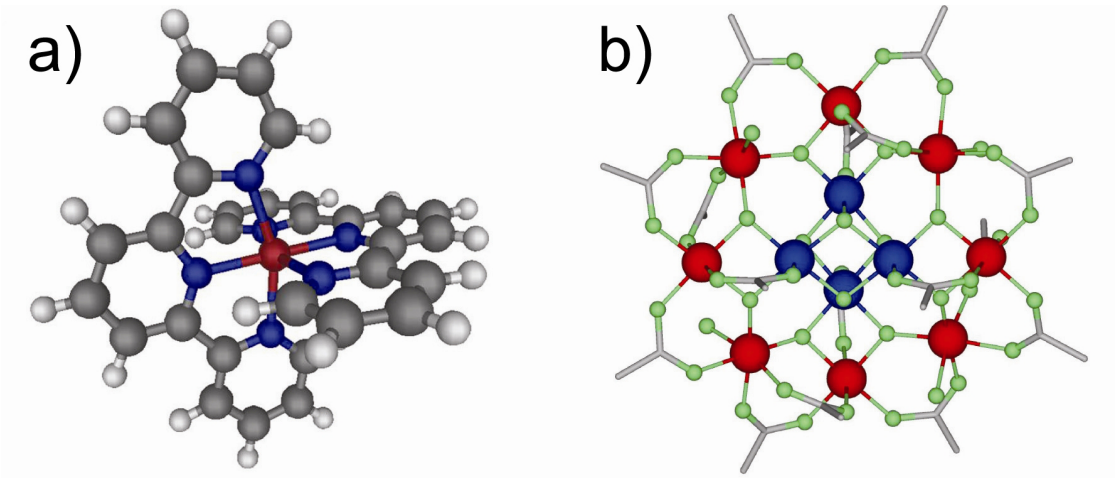


Figure 1.1: a) Example of a metal-tppz complex like those used in [65] (courtesy Abruña group). b) SMM cluster, $Mn_{12}Ac$.

Historically, the biggest discovery in the field of cluster-based molecular materials was the discovery of superconductivity in the Chevrel phases (for a review, see [1]). While there is some recent work on clusters with metal-metal bonding [2], there is more excitement about a class of molecular materials based on metal clusters without any direct metal-metal bonding. These materials are called single-molecule magnets (SMMs) [3] due to their intramolecular ferromagnetic properties at low temperature. Experiments on van der Waals crystals of SMMs will be reviewed in more detail in Section 3.2.

Individual metal complexes have been imaged in STM studies (see Subsection 1.3.2), and metal complexes and clusters have both found their way into single-molecule transistors (SMTs) (see Subsection 1.4.3 and Section 4.1). However, although there has been much recent work on single-electron transistors based on noble metal nanoparticles [4, 5], ferromagnetic nanoparticles [6] and superconducting aluminum nanoparticles [7], I am not aware of any single-molecule experiment based on well-defined metal clusters with direct metal-metal bonding. This is most likely because most metal clusters are created in the gas phase without pro-

tective ligands (e.g., [8,9]) so they would probably be absorbed into the electrodes in a single-molecule experiment.

1.2.3 π-conjugation

The field of carbon-based electronics is dominated by π-conjugated materials. π-conjugation refers to alternating single and double bonds between sp^2-bonded carbon atoms [10]. π-conjugation can lead to the delocalization of the $2p\pi$ orbitals in the planes above and below the σ-bonding plane. Some molecules are stabilized by their delocalized π-bonds. Examples of this are the aromatic molecules, π-conjugated molecules such as the polyacenes and the fullerenes which follow the Hückel $4n + 2$ rule [10]. Alternatively, π-conjugation can lead to a degeneracy which causes an electronic instability to an asymmetric state (known as a Jahn-Teller distortion) that can be strong enough to overcome lattice stiffness, especially in one-dimensional systems. This is the case in molecules satisfying the Hückel $4n$ rule for anti-aromaticity [10].

In the solid state, a distortion caused by degenerate states at the Fermi level is known as a Peierls distortion or charge density wave. It is a Peierls distortion that causes an undoped polyacetylene chain, which should be metallic if undistorted, to be insulating (although it can be doped to a metallic state). Infinite polyacene chains, though stiffer than polyacetylene chains, are still vulnerable to second-order Peierls distortions. However, higher dimensional systems, like graphene and carbon nanotubes, have too much lattice stiffness to be Peierls distorted. Indeed, we find that graphene is a semimetal while nanotubes are either metallic or semiconducting depending on how they are "rolled up" (i.e. their chiral vectors).

Almost all carbon-based electronic materials, including graphene, carbon nan-

otubes, fullerenes, conducting polymers, organic semiconductors, organic magnets and radical-ion salts, exhibit extensive π-conjugation [11]. The electronic structure of certain other materials, such as the photosynthetic pigments β-carotene (vitamin C) and chlorophyll and the inorganic superconductors MgB_2 and $(SN)_x$, are inextricably related to the fact that these materials are π-conjugated as well. However, for the remainder of this thesis, I will focus only on π-conjugated molecules and molecular materials used in molecular electronics. Molecular materials based on π-conjugated molecules will be reviewed in Subsections 1.2.4 and 1.2.5. Single-molecule experiments based on π-conjugated molecules will be reviewed in Subsections 1.3.2, 1.3.3, 1.3.4 and 1.4.2.

1.2.4 Molecular materials I: metals and superconductors

Molecular materials can be metals, superconductors, semiconductors or ferromagnets depending on the molecules from which they are made. Metals and superconductors, which are studied on the level of basic science, will be reviewed in this subsection. Semiconductors and magnets, which are of more practical interest in terms of devices, will be reviewed in Subsection 1.2.5.

When discussing carbon-based metals, it is important to note that there are very few examples that are truly metallic. In fact, even "metallic" nanotubes have a small, but measurable bandgap due to their curvature [12]. One experimental measure of metallicity is the temperature dependent DC resistivity ratio $\rho_r = \frac{\rho(1.4\,\mathrm{K})}{\rho(300\,\mathrm{K})}$, with ρ_r serving as an "effective order parameter" for the metal-insulator transition [13]. By this definition, the most "metallic" doped conducting polymer films prepared before 1998 were polypyrrole doped with PF_6 ($\rho_r \approx$ 4-8) and polyaniline doped with camphor sulfonic acid (PANI-CSA) ($\rho_r \approx$ 3-5), despite the fact

that oriented iodine-doped polyacetylene films had the highest room temperature conductivity of all conducting polymers by more than an order of magnitude ($\sigma(300\text{ K}) \approx 5000\text{-}8000$ S/cm) [14]. More recently, truly metallic PANI-CSA films were prepared with $\rho_r = \frac{\rho(5\,\text{K})}{\rho(300\,\text{K})} \approx 0.4$ [15]. Additionally, FETs that can be doped into the metallic regime via a gate electrode were made using a thiophene derivative [16].

With these caveats, I will move on to discuss molecular metals. Many of the molecular superconductors, including the Chevrel phases, the alkali-doped fullerenes and some organic radical-ion salts, are very conductive ($\sigma \gg 1$ S/cm) at room-temperatures, as are many non-superconducting organic radical-ion salts [11]. However, few if any of these materials are truly metallic. Ioffe and Regel [17] argued that, as the mean free path in a material becomes less than $1/k_F$, coherent metallic transport becomes impossible. Thus we have the Ioffe-Regel criterion that for good metals: $k_F l \gg 1$, where k_F is the Fermi wave number and l is the mean free path. By this definition, both the alkali-doped fullerenes and the first organic radical-ion salt known to be highly conductive, TTF-TCNQ[1], are "bad" metals [11].

As mentioned above, there are many superconducting molecular materials. The Chevrel-phase $PbMo_6S_8$ has a relatively high T_c of 15 K [1]. The first organic radical-ion salt found to be superconducting, $(TMTSF)_2PF_6$, is a quasi-one dimensional superconductor with T_c of 1 K under 12 kbar of pressure [11]. More recently, alkali-doped C_{60} (ionic) crystals (see Figure 1.2) were found to be superconducting with a maximum T_c of 33 K at atmospheric pressure ($RbCs_2C_{60}$) or 40 K at high pressure (Cs_3C_{60}) (for a review of superconducting fullerides, see [18]).

[1]See page xii for molecule abbreviations.

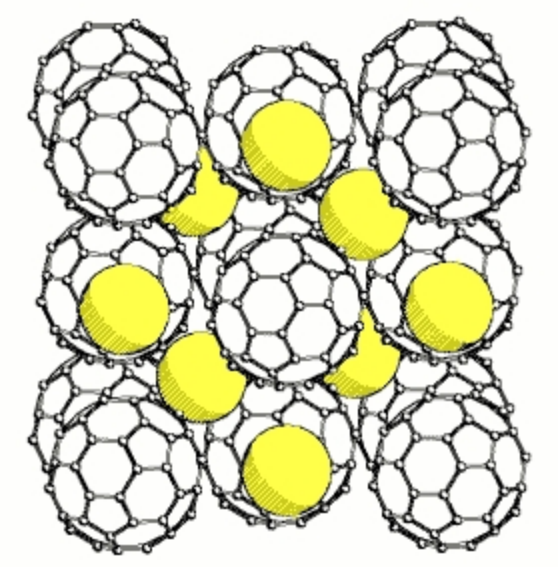


Figure 1.2: Superconducting alkali-doped fulleride crystal (courtesy V. H. Crespi).

Note that the maximum T_c of the fullerides is comparable to that of the most popular π-conjugated superconductor, MgB_2 ($T_c = 39$ K) [19], and is much higher than that of doped graphite (CaC_6 has $T_c = 11.5$ K) [20]. On the down side, fulleride superconductors are extremely air sensitive and are much more expensive than MgB_2.

Although superconductivity in the fullerides will be discussed in more detail in Section 6.2, it is important to mention here that there have been reports, now discredited, of gate-induced superconductivity in C_{60} derivatives with T_c as high as 117 K, by Jan Hendrik Schön, formerly of Bell Labs. Schön's malfeasance was not limited to superconducting fullerenes; he also reported, among other things, record mobilities in pentacene-based FETs. In 2002, an independent investigative committee headed by Malcolm Beasley of Stanford found that at least 17 of Schön's papers were based on fraudulent data [21]. Since then, many of his papers have been retracted and, in my opinion, no paper bearing his name should be believed.

1.2.5 Molecular materials II: semiconductors and magnets

Organic molecular semiconductors (see Figure 1.3a-e), which have the highest mobilities of all organic semiconductors, differ from conventional semiconductors in that they are typically undoped. They are labeled as p-type or n-type based on whether they have a higher mobility in terms of hole or electron transport. Most organic molecular semiconductors are p-type, and some of the best thin-film molecular semiconductors in terms of mobility are the p-type semiconductors based on pentacene ($\mu = 6$ cm^2/Vs) and 6T ($\mu = 1$ cm^2/Vs) [22]. Two of the best n-type thin-films are C_{60} and certain perylene derivatives (e.g. PTCDI). Excitations in molecular semiconductors are different than those in long-chain polymers. In long-chain polymers with a degenerate ground state (e.g. polyacetylene, the PNB base of polyaniline), there can be topological defects known as solitons (uncharged), while charged excitations in all long-chain polymers are known as polarons. Molecular semiconductors are often structurally incapable of topological excitations. Instead, uncharged excitations are known as Frenkel excitons if the electron and hole are on the same molecule, charge-transfer excitons if the electron and hole are on neighboring molecules and Wannier-Mott excitons if the electron and hole are separated by many molecules [11]. Charged excitons are known as charge-transfer states and usually involve crystals or films composed of two separate molecular species: a "donor" and an "acceptor".

There are many devices based on organic molecular semiconductors, including OFETs based on pentacene and 6T [22], OLEDs based on small molecules such as Alq_3 [23], photovoltaics based on thiophene:fullerene (p-type:n-type) films [24], sensors based on phthalocyanine films and, of course, liquid crystal displays [11]. Often, devices based on organic semiconductors have certain advantages over con-

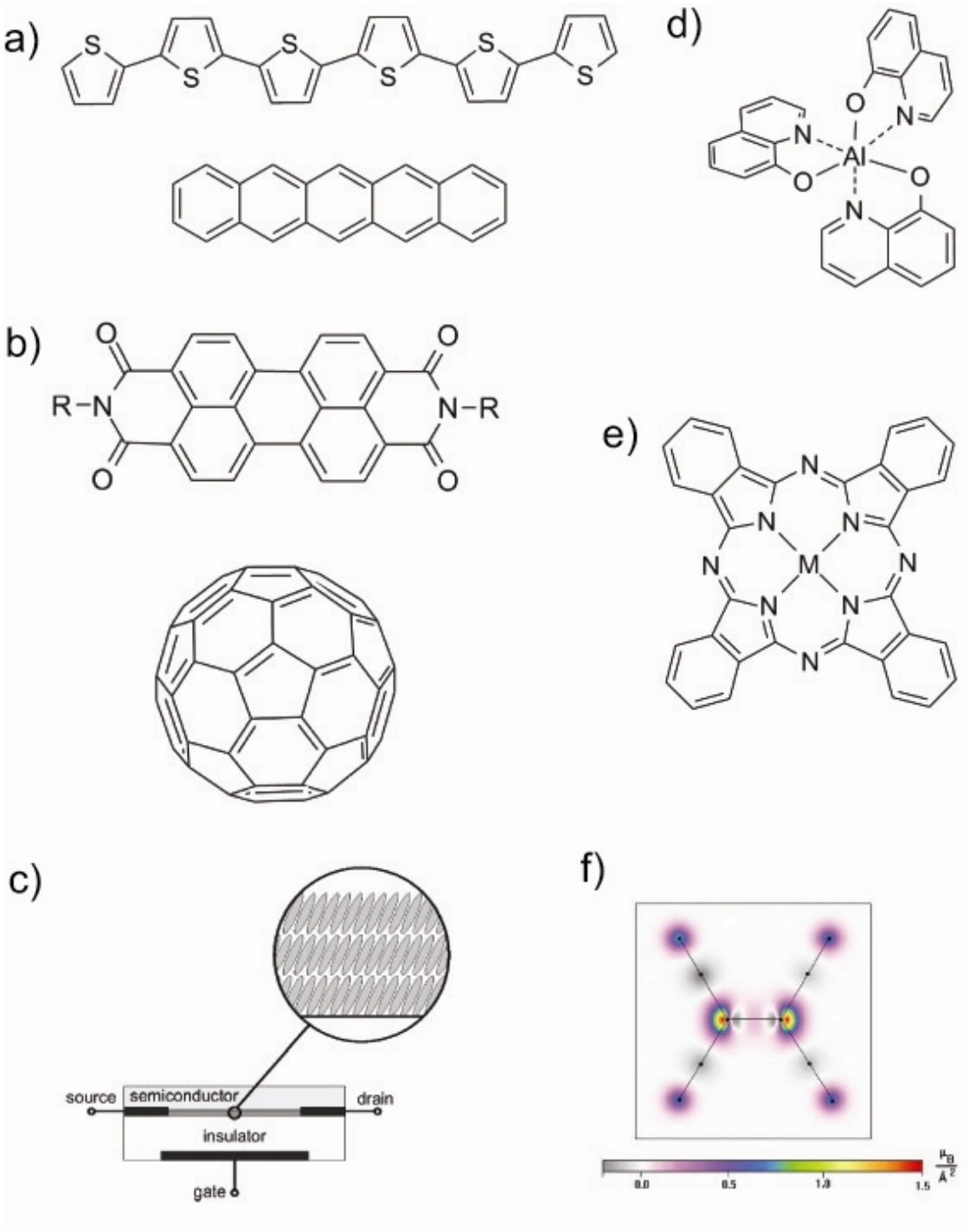


Figure 1.3: Semiconducting and magnetic organic molecules: a) p-type semiconductors 6T (above) and pentacene. b) n-type semiconductors PTCDI (above) and C_{60}. c) Cartoon of an OFET based on a molecular semiconductor (from [22]). d) OLED molecule, Alq_3. e) Sensor molecule, phthalocyanine. f) Spin density distribution of the molecular magnet anion, $TCNE^{-}$ (from [25]).

ventional silicon devices in that they might 1) be cheaper (especially for applications involving large displays), 2) be able to be processed at lower temperatures, 3) have advantageous physical properties (such as flexibility) or 4) have unique optical properties. However, as of the present, organic semiconductors cannot compete with silicon-based devices in performance or durability. In addition, many sensors made from organic semiconductors lack the specificity necessary to be useful in practical applications.

There has been a lot of work in the past decade on magnetic molecular materials with the goals of creating magnets which are smaller, have lower-temperature processing, are more bio-compatible or have greater tunability than traditional magnets. On the inorganic side, single-molecular magnets such as the Mn_{12} complexes have generated interest both theoretically in terms of quantum tunneling of magnetization and as candidates for data storage [3]. Experiments on crystals of SMMs will be discussed in Section 3.2. On the organic side, materials based on the organic radical-ion TCNE (spin 1/2, see [25], Figure 1.3f) have demonstrated interesting properties from ferromagnetism with a Curie temperature of 16 K (a combination of TCNE and C_{60}) [26] to photo-induced increases in the magnetic susceptibility below 75 K [27].

1.3 Single-molecule electronics

In this section, I will review experiments based on single-molecule electronics. Although there are many experiments which measure the conductance of a number of individual molecules measured in parallel, making use of either Langmuir-Blodgett films or self-assembled monolayers (SAMs), due to space constraints I will restrict my discussion to experiments which make measurements on single molecules. The

main challenge in doing single-molecule experiments is figuring out how to be certain one is making electrical contact to the molecule under examination, since it is often difficult to image the device *in situ*. Different experimenters have used different techniques to accomplish this goal, and experiments based on three of these techniques are reviewed later in this section. Yet before I begin my review, I feel the need share a word of caution regarding the history of single-molecule experiments.

1.3.1 A word of caution

Ever since Richard Feynman foretold the development of nanotechnology [28], there has been a great deal of excitement at the prospect of single-molecule electronics. This excitement grew more palpable when Aviram and Ratner first proposed how to make a rectifier out of a single molecule [29]. In the first years of the new millennium, it seemed like every issue of *Nature* and *Science* contained at least one single-molecule experiment. Unfortunately, many researchers got caught up in the excitement and published questionable results. This work, unlike the fraud perpetrated at Bell Labs (see Subsection 1.2.4), was not done with the intention to deceive, though it is clear that the researchers should have exercised more caution. Below, I will give two examples that illustrate the importance of skepticism in this field.

In 1999, Mark Reed, Jim Tour and coworkers published an article [30] claiming to have observed negative differential resistance (NDR) in devices made from SAMs of a π-conjugated molecule. A year later, Fraser Stoddart and Jim Heath [31] observed NDR in devices based on SAMs made from a different class of molecule. Later experiments strongly suggested that the NDR in both experiments was

caused by gold atoms migrating from the electrodes through the SAMs to cause short-lived electrical shorts [32]. More recently, NDR was observed in single-molecule STM studies in silicon substrates [33]. However, a later paper attributed the NDR in such systems to random configuration changes driven by inelastically scattered electrons [34].

Beginning in the late 1990s, there was a lot of work involving transport through single DNA molecules. In January of 2001, a paper [35] reported proximity-induced superconductivity in DNA and implied that DNA remains very conductive down to millikelvin temperatures. Later that year, two very respected scientists wrote an enthusiastic review which claimed that DNA showed "apparent coherent [electron] transfer over distances as long as 4 nm" [36]. Needless to say, all this optimism proved unfounded when multiple experiments (including [37]) showed that DNA was indeed an insulator. It is my understanding that there are few scientists in the field who still believe that DNA is good conductor.

These cautionary tales are to some degree the growing pains of an interdisciplinary field which requires detailed knowledge of both physics and chemistry, and they serve to illustrate how challenging it is to make good electrical contact to an object that is only a few nanometers in diameter. Despite these setbacks, there is a great deal of good work in the field of single-molecule electronics, much of it highlighted in the next few subsections. However, a person new to the field may rightly ask how to tell the good experiments from the bad ones.

A good rule of thumb in single-molecule experiments is to be initially skeptical of any experiment which only measures a two-terminal conductance, because such a measurement is very dependent on the contacts, and short circuits (very common in gold electrodes due to weak gold-gold bonding) can be easily mis-

interpreted. More reliable measurements have at least one additional technique to distinguish transport through a single molecule from other artifacts (see Subsections 1.3.2, 1.3.3 and 1.3.4, as well as Section 1.4). Such techniques include observing transport modulated by a gate electrode, an optical probe or an applied magnetic field. Other approaches are to use a setup which will allow for thousands of identical experiments to be performed in rapid succession, so that averaging can be used to sort out random fluctuations from more reproducible effects, or to directly image the molecule during the measurement using STM. Another rule of thumb is to avoid experiments where voltages of more than 100 mV are dropped across a molecule during measurement because electric fields this strong often cause the electrodes to become unstable.

However, no matter what precautions are taken, in every experiment it is **absolutely vital** to perform negative control experiments without the molecule present (or, if necessary, with an inert molecular spacer) in order to establish a background. This simple act could have prevented all the misinterpretations outlined above and has prevented me from publishing many such mistakes.

1.3.2 Scanned-probe experiments

Since both STM and conducting AFM involve conductive probes which are sharp on molecular scales, it is natural to use such probes as electrodes in single-molecule devices. Although some of the earliest STM work involves single-atom spectroscopy, these experiments are beyond the scope of my thesis. Instead, I begin my STM review with a paper which first showed that π-conjugated "molecular wires" could short out SAMs based on non-conjugated alkanethiols [38]. The first demonstration of an electromechanical oscillator based on a single C_{60} molecule

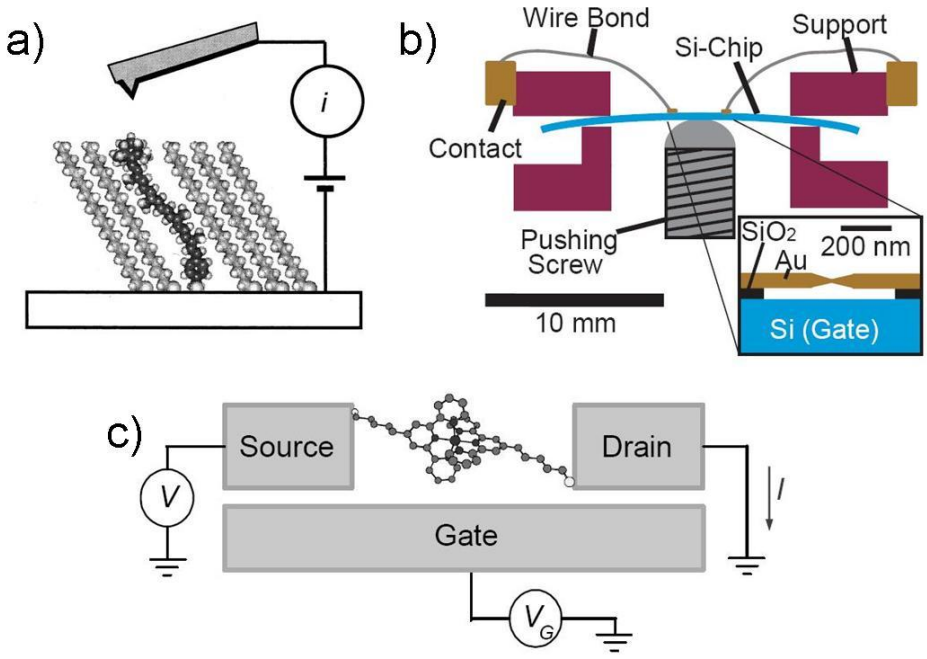


Figure 1.4: Experimental techniques in single-molecule electronics. a) Conducting AFM (from [47]). b) MBJ (from [55]). c) SMT made using electromigration (from [62]).

occurred a year later [39]. Following this, there were a number of beautiful papers imaging individual π-conjugated molecules, first by Wilson Ho's group [40,41] (the molecule in [41] is a copper phthalocyanine, which is a metal complex surrounded by a π-conjugated ligand) and later by other groups [42–44]. More recently, the conductance of a molecule was modulated by moving the molecule in relation to a dangling bond (charged impurity) on a silicon surface [45], and two π-conjugated n-type semiconductors were probed using BEEM [46].

One of the first single-molecule conducting AFM studies was similar to the first STM experiment described above, in that it was a measurement of the conductance of conductive π-conjugated carotene molecules trapped in an insulating alkanethiol SAM [47] (see Figure 1.4a). This was followed by measurements which extrapolated

conductivities of molecules by averaging over many repeated measurements. The first of these was another paper by Stuart Lindsay's group on non-conjugated (insulating) alkanethiol molecules [48], followed by work by N. J. Tao's group on π-conjugated molecules [49, 50]. In all of the conductive AFM work mentioned so far, the molecules to be measured were first made into SAMs on gold surfaces using a thiol-gold (S-Au) bond. This bond, though strong, is non-specific in that the sulfur can bond to 1-, 2- or 3-fold hollow sites in the gold surface. This leads to different metal-molecule contacts with different resistances, and, since the contact resistance often dominates the measurement, this causes wide spreads in the measured resistances of a single molecular species. Recently, researchers at Columbia have found a way around this problem by using the more specific amine-gold (NH_2-Au) bonding instead of thiol-gold bonding [51, 52].

1.3.3 Mechanical break junctions

Mechanical break junctions (MBJs) can be used to make nanometer-spaced electrodes from a continuous wire. The wire is fabricated on a flexible substrate, weakened at some central point and then separated into two distinct electrodes by bending the substrate underneath. The first single-molecule experiment using the MBJ technique was a room-temperature measurement of the conductance of benzene dithiol, a π-conjugated molecule with a large HOMO-LUMO gap (bandgap), by Reed and coworkers [53]. This was followed by a low-temperature measurement of a single hydrogen molecule between platinum electrodes which showed almost perfect conductance (nearly $2e^2/h$) at 4.2 K [54]. MBJs can also be used to study the dependence of electronic characteristics of single-molecule devices on the interelectrode spacing. Experiments in this category include low temperature

measurements of C_{60} showing mechanically adjustable features (see Figure 1.4b) of both Coulomb blockade [55] and the Kondo effect [56]. The Kondo effect in SMTs will be discussed in Subsection 1.4.3.

1.3.4 Transistor geometries

A SMT is a three terminal device in which a single-molecule is contacted on two sides by metallic "source" and "drain" electrodes, and underneath by a "gate" electrode which is separated from the molecule by an insulating oxide layer. SMT experiments usually involve looking for quantum effects at low temperature, either for Coulomb blockade (see Section 3.1) and/or for the Kondo effect (see Subsection 1.4.3).

Most SMT experiments to date have come from electrodes made via electromigration. These experiments will be reviewed in the next section. Recently, a different technique involving electrodes made from carbon nanotubes cleaved with an oxygen plasma was used to measure a variety of π-conjugated molecules [57]. This technique has the advantage of avoiding the need for electromigration which could damage the molecule under study (see Subsection 1.4.1).

1.4 Single-molecule transistors made via electromigration

1.4.1 Electromigrated break junctions

The most common way to make a SMT is to use the electromigration technique developed by Hongkun Park and collaborators [58]. In this technique, a thin wire is fabricated on top of a gate electrode, and then current is flowed through the wire until it fails due to electromigration. This produces electrodes separated by only a

few nanometers. To make a SMT, the molecules are drop-cast from solution onto the wire before electromigration. Then, during the breaking process, molecules are somehow drawn into the gap formed between the electrodes (see Figure 1.4c). Temperatures of gold wires during this process can reach around 500 K [59], so the molecules chosen for these experiments must be stable up to these temperatures (see Section 2.4).

The first SMT ever measured was made using the electromigration technique [60]. For practical advice as to how to make and measure SMTs using electromigration, the best places to look are two wonderful theses by Abhay Pasupathy of the Ralph group [61] and Jiwoong Park of the McEuen group [62], as well as Chapter 2 of this thesis.

1.4.2 Vibration-assisted tunneling

While electrons in SMTs can elastically tunnel through the ground state of a molecule, they can also tunnel inelastically, coupling to vibrational modes in the molecule via the equivalent of electron-phonon coupling. These low lying excitations (typically 1-50 meV) are easily seen in low-temperature Coulomb blockade tunneling spectra (see Figure 1.5a, Section 3.1). Vibrations were observed in the conductance spectra of the first SMT based on C_{60} [60] and as satellite peaks to Kondo resonances in C_{60} [63]. More recently, the excitations in a simple "dumbbell" molecule (C_{140}) were systematically compared with a Frank-Condon model [64].

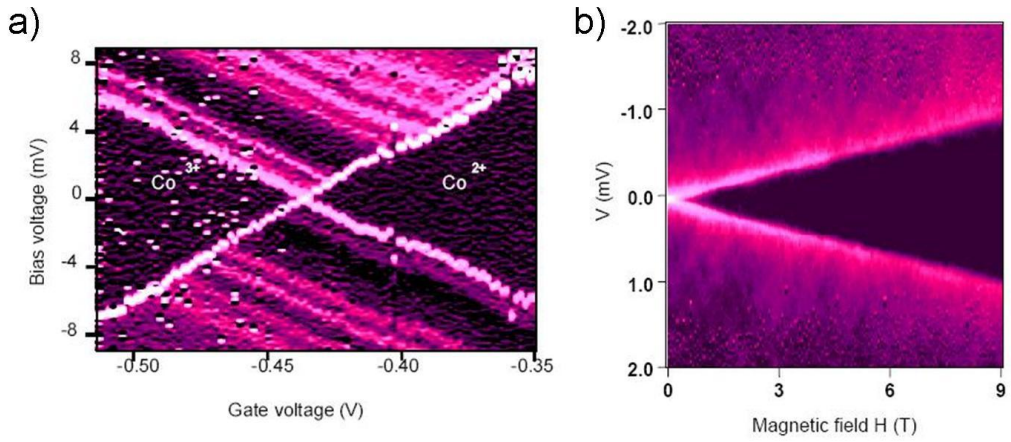


Figure 1.5: a) Vibrational excited states and b) the Kondo effect in SMT conductance spectra (from [61]).

1.4.3 The Kondo effect in single-molecule transistors

The Kondo effect is a higher-order scattering process due to a magnetic impurity whereby the conduction electrons try to "screen" the spin (for a more rigorous treatment of the Kondo effect in SMTs, see [61]). Unlike the Kondo effect in bulk metals where this impurity scattering leads to lower conductance values, the Kondo effect in SMTs leads to a peak in the conductance spectra around zero voltages (see Figure 1.5b) below a Kondo temperature characteristic to the system. A common sense explanation for why there is a conductance increase rather than a decrease is that the current through an SMT is essentially a "scattering" process in and of itself in contrast to conductance in a bulk metal, so additional scattering should lead to more, not less, current. The Kondo effect was first observed in SMTs in a pair of experiments on metal complexes [65, 66], and later in C_{60} [67]. More recently, the Kondo effect was observed in a C_{60}-based SMT with ferromagnetic (nickel) electrodes leading to negative values for the magnetoresistance [68].

1.5 Organization of this thesis

In this introduction, I have reviewed the basic properties of the materials used in molecular electronics, as well as some of the most relevant experiments in single-molecule electronics. The rest of this thesis is organized as follows.

The second chapter describes some fabrication and measurement techniques useful for experimentalists looking to make and measure SMTs.

The third chapter describes some theory behind both Coulomb blockade and SMMs, and then goes on to describe Mathematica simulations of hysteresis and magnetic relaxation in SMTs based on SMMs.

The fourth chapter describes both previous and new experimental results from SMTs made from anisotropic, high-spin SMM compounds known collectively as Mn_{12} compounds. Discrepancies between experiment and theory will be addressed.

The fifth chapter describes experimental results from SMTs made from isotropic, high-spin endofullerene ($N@C_{60}$) compounds. Some background on endofullerenes will also be presented here.

The sixth chapter describes two side projects I have done having to do with electrochemistry. The first involves gold nanoparticles mimicking polyaniline transistors, while the second involves electrochemical synthesis of fullerene superconductors.

The seventh chapter provides some conclusions from the first six chapters and gives some ideas for future experiments.

REFERENCES

[1] R. Chevrel in S. Foner, B. B. Schwartz (Eds.), *Superconductor Materials Science: Metallurgy, Fabrication and Applications*, Plenum, New York, 1981.

[2] M. Yuan *et al.*, Chem. Mat. **18**, 4296 (2006).

[3] D. Gatteschi and R. Sessoli, Angew. Chem. Int. Ed. **42**, 268 (2003).

[4] K. I. Bolotin, F. Kuemmeth, A. N. Pasupathy and D. C. Ralph, Appl. Phys. Lett. **84**, 3154 (2004).

[5] J. R. Petta and D. C. Ralph, Phys. Rev. Lett. **89**, 156802 (2002).

[6] S. Guéron, M. M. Deshmukh, E. B. Myers and D. C. Ralph, Phys. Rev. Lett. **83**, 4148 (1999).

[7] D. C. Ralph, S. Guéron, C. T. Black and M. Tinkham, Physica B **280**, 420 (2000).

[8] J. Li, X. Li, H.-J. Zhai and L.-S. Wang, Science **299**, 864 (2003).

[9] D. E. Bergeron, P. J. Roach, A. W. Castleman Jr., N. O. Jones and S. N. Khanna, Science **307**, 231 (2005).

[10] J. K. Burdett, *Chemical Bonding in Solids*, Oxford University Press, New York, 1995.

[11] M. Pope and C. E. Swenberg, *Electronic Processes in Organic Crystals and Polymers*, Oxford University Press, New York, 1999.

[12] M. Ouyang, J.-L. Huang, C. L. Cheung and C. M. Lieber, Science **292**, 702 (2001).

[13] A. J. Heeger, Physica Scripta **T102**, 30 (2002).

[14] R. Menon, C. O. Yoon, D. Moses and A. J. Heeger in T. A. Skotheim, R. L. Elsenbaumer and J. R. Reynolds (Eds.), *Handbook of Conducting Polymers, 2nd edition*, Marcel Dekker, New York, 1998.

[15] K. Lee *et al.*, Nature **441**, 65 (2006).

[16] A. S. Dhoot *et al.*, Proc. Nat. Acad. Sci. **103**, 11834 (2006).

[17] A. F. Ioffe and A. R. Regel. Progr. Semicond. **4**, 237 (1960).

[18] O. Gunnarsson, Rev. Mod. Phys. **69**, 575 (1997).

[19] J. Nagamatsu, N. Nakagawa, Y. Z. Murakana and N. Akimitsu, Nature **410**, 63 (2001).

[20] T. E. Weller, M. Ellerby, S. S. Saxena, R. P. Smith and N. T. Skipper, Nat. Phys. **1**, 39 (2005).

[21] M. R. Beasley, S. Datta, H. Kogelnik, H. Kroemer and D. Monroe, *Report of the Investigation Committee on the Possibility of Scientific Misconduct in the work of Hendrik Schön and Coauthors* (2002).

[22] G. Horowitz, J. Mater. Res. **19**, 1946 (2004).

[23] J. C. Scott and G. G. Malliaras in P. F. van Hutten and G. Hadziioannou (Eds.), *Semiconducting Polymers: Chemistry, Physics and Engineering*, Wiley-VCH, Weinheim, 1999.

[24] Y. Kim *et al.*, Nat. Mat. **5**, 197 (2006).

[25] A. Zheludev *et al.*, J. Am. Chem. Soc. **116**, 7243 (1994).

[26] P. M. Allemand *et al.*, Science **253**, 301 (1991).

[27] D. A. Pejaković, C. Kitamura, J. S. Miller and A. J. Epstein, Phys. Rev. Lett. **88**, 057202 (2002).

[28] R. P. Feynman, Engineering and Science **23**, 22 (1960).

[29] A. Aviram and M. A. Ratner, Chem. Phys. Lett. **29**, 277 (1974).

[30] J. Chen, M. A. Reed, A. M. Rawlett and J. M. Tour, Science **286**, 1550 (1999).

[31] C. P. Collier *et al.*, Science **289**, 1172 (2000).

[32] R. F. Service, Science **302**, 556 (2003).

[33] N. P. Guisinger, M. E. Greene, R. Basu, A. S. Baluch and M. C. Hersam, Nano Lett. **4**, 55 (2004).

[34] J. L. Pitters and R. A. Wolkow, Nano Lett. **6**, 390 (2006).

[35] A. Y. Kasumov *et al.*, Science **291**, 280 (2001).

[36] C. Dekker and M. A. Ratner, Phys. World **14**, 29 (2001).

[37] C. Gómez-Navarro *et al.*, Proc. Nat. Acad. Sci. **99**, 8484 (2002).

[38] L. A. Bumm *et al.*, Science **271**, 5256 (1996).

[39] C. Joachim and J. K. Gimzewski, Chem. Phys. Lett. **265**, 353 (1997).

[40] B. C. Stipe, M. A. Rezaei and W. Ho, Science **280**, 1732 (1998).

[41] G. V. Nazin, X. H. Qiu and W. Ho, Science **302**, 77 (2003).

[42] X. Lu, M. Grobis, K. H. Koo, S. G. Louie and M. F. Crommie, Phys. Rev. Lett. **90**, 096802 (2003).

[43] J. Repp, G. Meyer, S. M. Stojković, A. Gourdon and C. Joachim, Phys. Rev. Lett. **94**, 026803 (2005).

[44] M. Grobis *et al.*, Phys. Rev. Lett. **94**, 136802 (2005).

[45] P. G. Piva *et al.*, Nature **435**, 658 (2005).

[46] A. Bannani, C. Bobisch and R. Möller, Science **315**, 1824 (2007).

[47] G. Leatherman *et al.*, J. Phys. Chem. B **103**, 4006 (1999).

[48] X. D. Cui *et al.*, Science **294**, 571 (2001).

[49] B. Xu and N. J. Tao, Science **301**, 1221 (2003).

[50] B. Q. Xu, X, L. Li, X. Y. Xiao, H. Sakagucki and N. J. Tao, Nano Lett. **5**, 1491 (2005).

[51] L. Venkataraman *et al.*, Nano Lett. **6**, 458 (2006).

[52] L. Venkataraman, J. E. Klare, C. Nuckolls, M. S. Hybertsen and M. L. Steigerwald, Nature **442**, 904 (2006).

[53] M. A. Reed, C. Zhou, C. J. Muller, T. P. Burgin and J. M. Tour, Science **278**, 252 (1997).

[54] R. H. M. Smit *et al.*, Nature 419, 906 (2002).

[55] A. R. Champagne, A. N. Pasupathy and D. C. Ralph, Nano Lett **5**, 305 (2004).

[56] J. J. Parks *et al.*, arXiv:cond-mat/0610555v1 (2007).

[57] X. Guo *et al.*, Science **311**, 356 (2006).

[58] H. Park, A. K. L. Kim, J. Park, A. P. Alivisatos and P. L. McEuen, Appl. Phys. Lett. **75**, 301 (1999).

[59] T. Taychatanapat, K. I. Bolotin, F. Kuemmeth, and D. C. Ralph, Nano Lett. **7**, 652 (2007).

[60] H. Park *et al.*, Nature **407**, 57 (2000).

[61] A. N. Pasupathy, *Electron Transport in Molecular Transistors*, Ph.D. thesis, Cornell University, 2004.

[62] J. Park, *Electron Transport in Single Molecule Transistors*, Ph.D. thesis, University of California, Berkeley, 2003.

[63] L. H. Yu *et al.*, Phys. Rev. Lett. **93**, 266802 (2004).

[64] A. N. Pasupathy *et al.*, Nano Lett. **5**, 203 (2005).

[65] J. Park and A. N. Pasupathy *et al.*, Nature **417**, 722 (2002).

[66] W. Liang, M. P. Shores, M. Bockrath, J. R. Long and H. Park, Nature **417**, 725 (2002).

[67] L. H. Yu and D. Natelson, Nano Lett. **4**, 79 (2004).

[68] A. N. Pasupathy *et al.*, Science **306**, 86 (2004).

Chapter 2

Nanofabrication and experimental details

In this chapter, I will describe some of the nanofabrication, electromigration, molecular deposition and measurement techniques involved in single-molecule transistor experiments. Although these techniques were originally developed by Hongkun Park and coworkers [1, 2], the specific techniques I used were taught to me by Abhay Pasupathy and are outlined in chapters 2 and 3 of his thesis [3]. In order to avoid redundancy, I will only mention in detail the aspects of my techniques which differ from Abhay's. I should note that I did all of the fabrication discussed in this thesis in the old CNF facility, Knight Laboratory, as opposed to the newer facility in Duffield Hall.

2.1 Overview of fabrication

A schematic of the fabrication process I used is pictured in Figure 2.1. The goal of this process is to make Au or Pt nanowires roughly 150 nm wide and 10 nm high that are connected to macroscopic contacts. These wires are fabricated on top of an Al gate electrode which is covered by a few-nm-thick native oxide layer. Each nanowire is connected to an individual contact pad (roughly 0.04 mm^2 in area) on one end and a large electrode shared by all 30 nanowires (a "common ground") on the other. Many sets of these wires, gates and contacts are fabricated on a silicon wafer, which is subsequently diced into 140 identical chips. Each finished chip

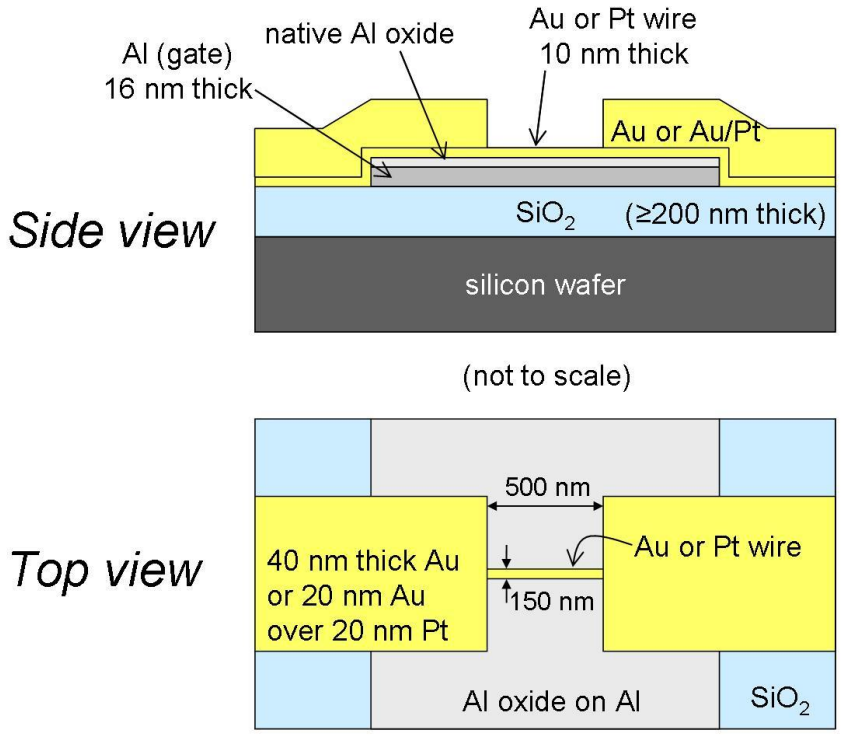


Figure 2.1: Schematic of lithography used for making single-molecule transistors. Adapted from a poster by Janice Guikema.

contains 30 nanowires, 6 gates (each contacting 5 nanowires) and 37 macroscopic contacts (one to each nanowire, one to the "common ground" and one to each gate).

The fabrication process is summarized below. See chapter 2 of reference [3] for more details.

1. A thick oxide layer (over 200 nm) is grown on top of a 4-inch diameter, 500 μm thick silicon wafer.

2. Alignment marks for photolithography are etched into the silicon oxide. These are necessary so that the multiple layers of photolithography align with one another.

3. A thin (16 nm) gold layer is fabricated using photolithography (10x stepper,

image reversal). The purpose of this layer is to connect the thick gold layer (discussed in the next step) to the smallest features defined by electron-beam (e-beam) lithography.

4. A thick (160 nm) gold layer is fabricated using photolithography (10x stepper, image reversal). The purpose of this layer is to provide macroscopic contact pads for wirebonding.

5. A thin (16 nm) aluminum layer is fabricated using photolithography (10x stepper, image reversal). This layer forms the Al gate electrodes. During the aluminum evaporation, the stage containing the wafer is cooled with liquid nitrogen to produce smoother films for the subsequent e-beam lithography.

6. If there are Al streaks on the wafer due to cracks in the photoresist during the low temperature Al evaporation, they are removed by an etching step. In practice, I found this step was rarely necessary.

7. The nanowires are fabricated using e-beam lithography. They are 10 nm high (see Section 2.2) and made of either Au or Pt (see Section 2.3). When platinum is used, I evaporate in 2.5 nm increments to avoid melting the resist. Unlike in the previous lithography steps, no Ti sticking layer is used during the evaporation (it is unnecessary, and it interferes with the electromigration process). During the metal evaporation, the stage containing the wafer is cooled with cold water (see Section 2.2).

8. Another e-beam step is done to ensure good contact between the nanowires and the "thin gold" photolithography. If the nanowires made are gold, this contact layer is made of 40 nm of gold. If the nanowires are platinum, this

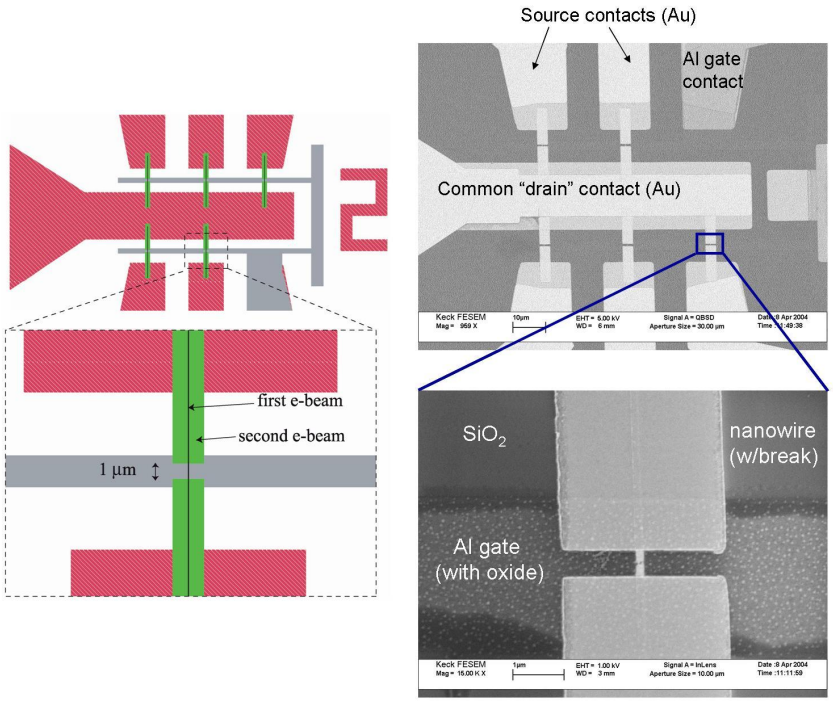


Figure 2.2: Schematic (left) and SEM images (right) of nanowires made using a 2-step e-beam process. Schematic from [3]. SEM images courtesy Janice Guikema.

contact layer is made of 20 nm of platinum (evaporated in 5 nm increments to prevent the resist from melting) followed by an additional 20 nm of gold. Again, during the metal evaporation, the stage containing the wafer is cooled with cold water.

9. The wafer is covered with a thick layer of resist and then diced into chips using the dicing saw. It is now finished and ready to be named. While every group member has his or her own naming conventions, all my wafers were named after Simpsons characters.

Once the fabrication is completed, random chips should be selected to check that the nanowires are intact and that the gates are neither shorted to nor completely isolated from the nanowires. Typical gate leakage to the common electrode

begins around 2-3 V. Wafers with gates that do not leak by 2-3 V usually do not show any Coulomb blockade in an SMT experiment. For unknown reasons, only around 1 of every 3 wafers fabricated will demonstrate Coulomb blockade in SMT experiments and no blockade in negative control experiments (see Section 2.5). Therefore, once one has learned how to fabricate, it is best to make multiple wafers simultaneously.

To make an SMT, a chip is cleaned, and the molecules used in the experiment are deposited on the surface of the chip (see Section 2.5). The chip is then wire-bonded to an appropriate package, fitted on a probe and lowered in to a dilution refrigerator. At low temperatures, the wires are broken via electromigration to form nm-scale gaps [1]. In a certain number of junctions, a molecule is drawn into the gap and a single-molecule transistor is formed. If two or more molecules are drawn in to the gap, it is not a concern since each molecule will experience a unique electrostatic environment, and so resonant tunneling will only occur through one molecule at a given gate voltage (see Chapter 3). The details of the measurement process will be given in Section 2.6.

2.2 Thin (10nm) wires

Since most people in the Ralph group work with thicker nanowires (at least 16 nm thick), I thought I would say a few words about 10 nm wires. Thinner nanowires have the advantage of being closer to the gate electrode (on average), and so there is often better coupling between the molecule and the gate electrode in SMTs made from 10 nm wires than in those made from thicker nanowires. However, 10 nm wires are trickier to fabricate. They require two e-beam steps because, unlike thicker nanowires, a 10 nm wire cannot make good contact to the photolithography

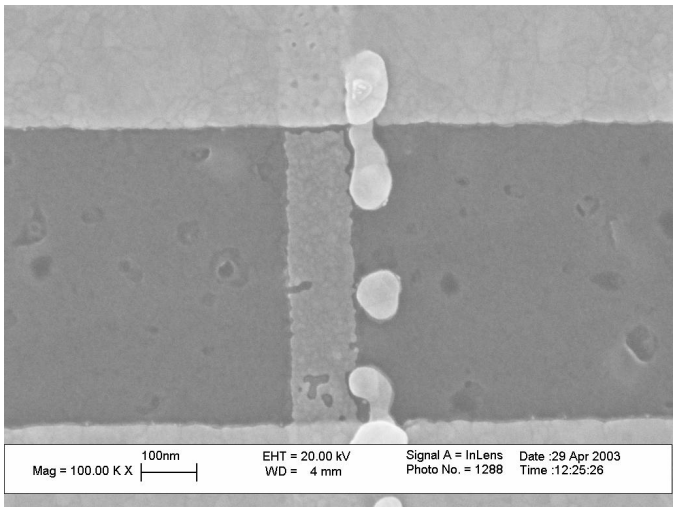


Figure 2.3: SEM images of failed attempts at making 10 nm wires (see text).

layers on its own but instead requires a second e-beam step to connect the nanowire to the photolithography.

Figure 2.3 is an SEM image which illustrates two failed attempts at gold nanowires. In the first attempt, I did not cool the stage during the second e-beam evaporation, so the gold nanowire melted as the contact was evaporated over it and the gold "balled up" (see "wire" on right side in Figure 2.3). This is why I always cool the stage with cold water during the evaporation process, even though it is probably not necessary during the first e-beam step for gold nanowires. Water cooling should always be used during platinum evaporations to prevent the resist from melting. In my second attempt, I tried to salvage the wafer by evaporating another nanowire over the contacts made during the second e-beam step. This led to a nanowire which was discontinuous at the contacts (see top of wire on left side in Figure 2.3). This discontinuity occurred because the contacts are 40 nm high and so the 10 nm nanowire did not have enough metal to get over the steep slope of the contact. The moral of Figure 2.3 is to cool the stage during the e-beam evaporations and to make the nanowires before doing the second e-beam step.

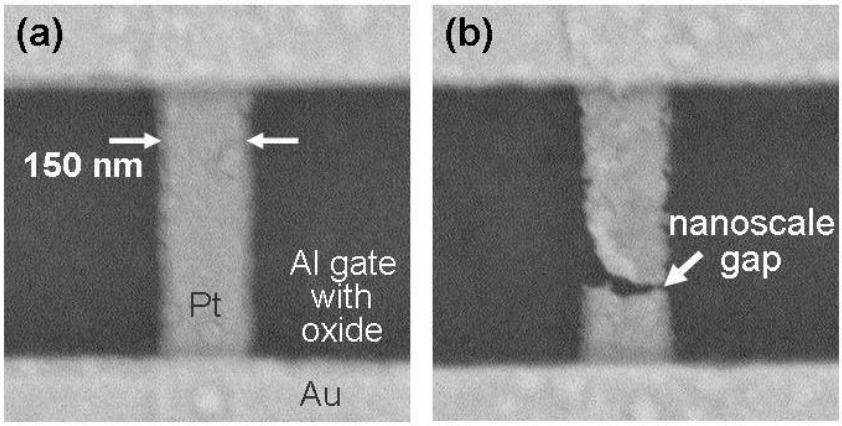


Figure 2.4: SEM images of 10 nm thick Pt wires (a) before and (b) after electromigration at $T \sim 4.7$ K with negligible series resistance. SEM images courtesy Janice Guikema.

Figure 2.4 shows an SEM image of a properly fabricated 10 nm Pt nanowire (a) before and (b) after electromigration. The Al gate electrode under the Pt nanowire is not visible in the SEM image. The wire was broken by applying a slow voltage ramp to the contact pad of the nanowire while keeping the common electrode grounded until the wire failed. The breaking was done using a 4 K probe with negligible series resistance [4]. This leads to a nanoscale gap arising somewhere on the nanowire. Abhay's only experience with 10 nm wires was that after breaking "nearly every wire showed Coulomb-blockade like characteristics" [3]. Based on this one bad experience, Abhay abandoned 10 nm wires, but I have had good success with one wafer I made with 10 nm Pt wires (Frank Grimes). However, most of my wafers made with 10 nm wires either failed to exhibit Coulomb blockade in SMT experiments or exhibited blockade in negative control experiments.

Unsurprisingly, 10 nm wires break differently than thicker nanowires do. Figure 2.5 shows breaking curves of a 10 nm Au wire and a 16 nm Au wire broken under identical conditions. Both wires pictured had fullerenes deposited on top of

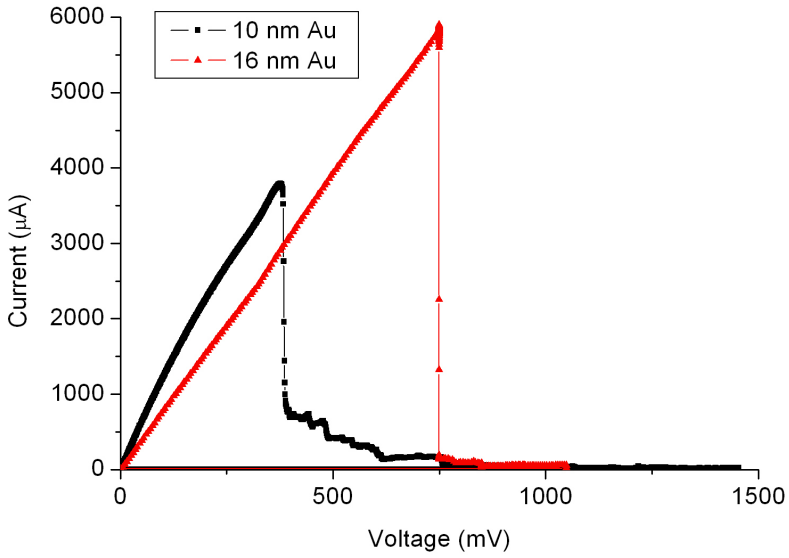


Figure 2.5: Breaking curves of 10 nm and 16 nm Au wires. Both wires had fullerenes deposited on their surface before breaking, and both were broken in a dilution refrigerator with 140 Ω series resistance. 16 nm wires courtesy Ferdinand Kuemmeth.

them before breaking at low temperatures. The main difference between the two curves is that the 10 nm wire broke at substantially lower voltages than the 16 nm wire. This is advantageous because there will be less chance that any molecules present will be damaged by the breaking process [4]. Another difference between the curves is that, around 100 mV before the 10 nm wire fails, the resistance of the wire shifts slightly. This shift in resistance during breaking is characteristic of 10 nm wires, although I do not understand the physical basis for this shift.

2.3 Platinum vs. gold wires

While most researchers in the field (including the rest of the Ralph group) make non-magnetic nanowires out of gold, the nanowires I have made that worked in SMT experiments were platinum. Most single-molecule experiments have been done using gold because most researchers use molecules with thiol ligands to affix

the molecules on the surface of their electrodes, and it is well known that thiols stick strongly to gold. However, thiols also stick to platinum (though not as strongly as they do to gold) and other ligands are available which stick strongly to platinum, such as isonitriles. Moreover, I have found that it is not really necessary to use molecules with ligands designed to stick to specific metals since almost any molecule will stick to a clean metal surface.

Figure 2.6 shows breaking curves of a 10 nm Au wire and a 10 nm Pt wire broken under identical conditions. Both wires pictured had fullerenes deposited on top of them before breaking at low temperatures. The main difference is that the Au wire broke at substantially lower voltages than the Pt wire. Note that both breaking curves show the shift in resistance just before the breaking point which is characteristic of 10 nm wires. One final point is that while gold wires can be rebroken many times, each break leading to a slightly higher-resistance junction (see reference [3]), platinum wires usually reform when one is trying to rebreak them.

2.4 Characteristics of molecules that will lead to successful experiments

Not every molecule will work in an SMT experiment, and many that will "work" are not interesting enough to be worth the significant amount of time and effort it takes to make measure a single-molecule transistor. Below is a list of requirements which I feel are necessary for a molecule to be a successful SMT candidate.

1. The molecule must have an electrochemical potential close in energy to the Fermi levels of the leads at zero bias, so that one can achieve resonant tunnel-

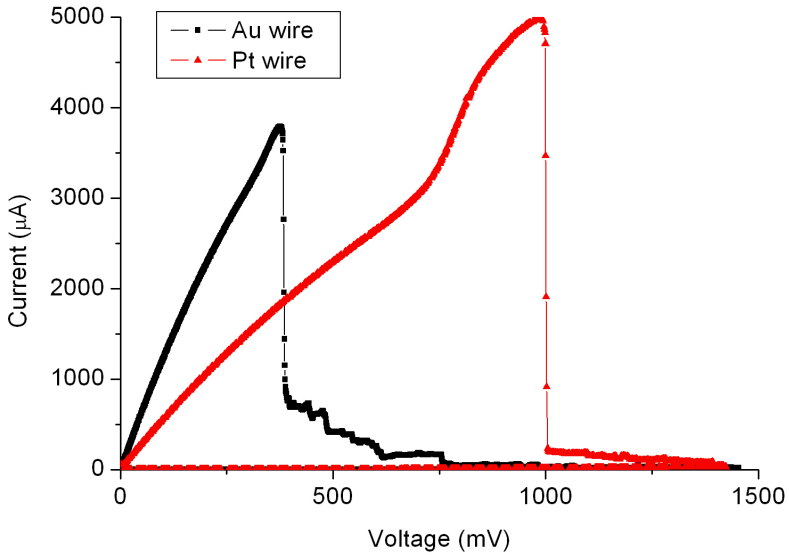


Figure 2.6: Breaking curves of 10 nm Au and Pt wires. Both wires had fullerenes deposited on their surface before breaking, and both were broken in a dilution refrigerator with 140 Ω series resistance.

ing through the molecule. Resonant tunneling is necessary to observe either Coulomb blockade or the Kondo effect. Since the ratio of the capacitance between the gate and the molecule to the total capacitance in the circuit is small (see Section 3.1), this means that one can modulate the electrochemical potential of the molecule by at most ±1 V. The best way to ensure that the electrochemical potential of the molecule in question is close to that of the leads is to perform an electrochemical experiment (cyclic voltammetry) to confirm that there are redox peaks close to "zero" volts (the closer, the better, and if they are farther than 0.5 V away from zero, it usually means trouble). Talk to your local electrochemist (at Cornell, the Abruña lab) for help on how to perform these experiments and how to interpret what "zero" means in terms of electrochemical reference electrodes.

2. The molecule must be both stable in air at room temperature and stable in

inert environments (He, vacuum) up to at least 500 K (for gold electrodes—perhaps higher for platinum). It must be air-stable at room temperature because the chip must be wire-bonded to a package compatible with the dilution fridge probes, and the wire-bonder can only be operated in ambient conditions. The molecule must be stable in inert atmospheres up to 500 K because gold wires reach these temperatures during electromigration [4, 5], even if the electromigration is done at low temperatures.

3. The molecule must have interesting physical properties (magnetic, optical, etc.) which will lead to SMT data which are *qualitatively different* than those seen in previous experiments (see Subsections 1.4.2 and 1.4.3). The device to device variation in SMT experiments is too substantial to count on seeing a quantitative difference between experiments on SMTs made from similar molecules. For ideas about molecules with interesting physical properties, see Section 1.2. However, one must be sure that the physical property in question will be observable via the current/conductance data generated in an SMT experiment.

2.5 Depositing the molecules

To deposit the molecules, they must first be dissolved in an appropriate solvent with a concentration of 0.1-1 millimolar. Certain solvents, such as acetone, should be avoided since they will lead to Coulomb blockade even without any additional molecules present. Before deposition, the chip containing the nanowires should be cleaned by leaving it to soak in acetone for at least an hour, rinsing with clean acetone, rinsing again with clean isopropanol and plasma cleaning in a 90 W

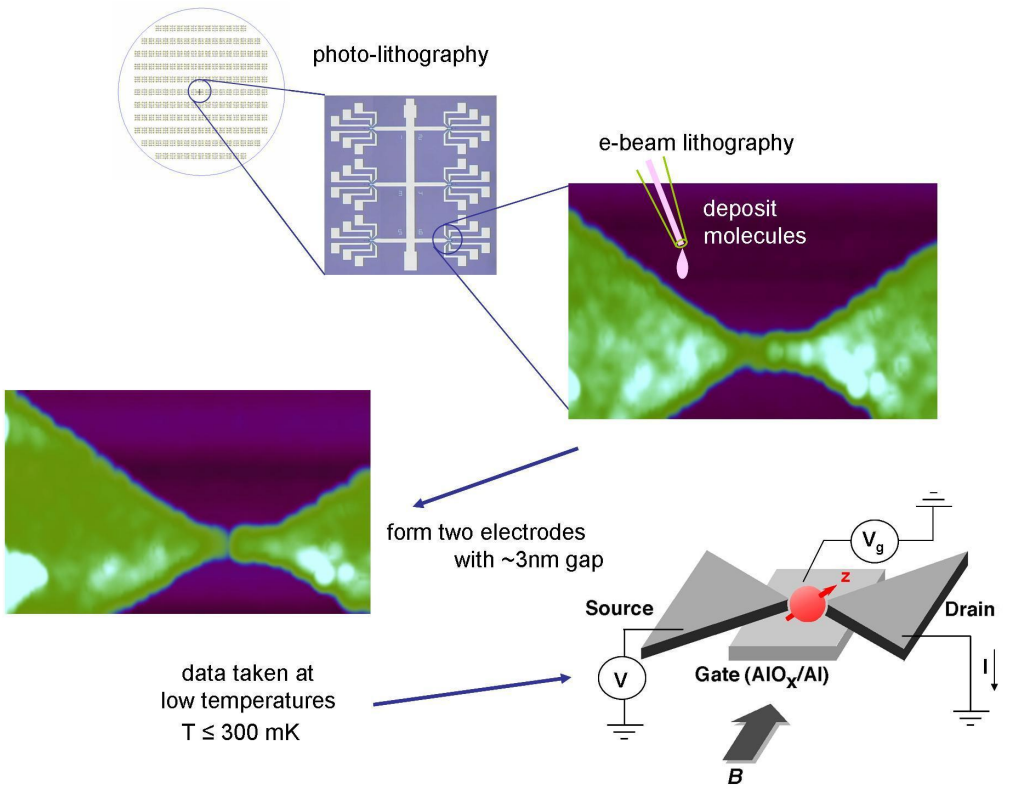


Figure 2.7: Schematic of deposition process. The molecules are drop-cast onto the surface of a chip containing the nanowires before electromigration at low temperatures. Adapted from a talk by Abhay Pasupathy and from [6].

oxygen plasma for 2 minutes (I used the PlasmaTherm 72 at CNF). Since chips should be plasma cleaned immediately before deposition, and since most molecules cannot be brought into Duffield Hall without substantial hassle, I did an additional plasma clean with a weaker 18 W oxygen plasma for 15 minutes (using the Harrick Plasma PDC-32G in G12 Clark Hall) prior to depositing the molecules.

The molecules are then drop-cast onto the chip as part of the procedure outlined in Figure 2.7. I deposit around 25 μL, wait 1-5 minutes, then blow the drop off the chip using high-purity nitrogen in order to prevent the drop from evaporating and leaving a residue. This process can be repeated if necessary. If molecules with ligands designed to stick to a specific metal are used, then you may want to soak

the chips overnight in the solution following [3], but I have never done this. For control experiments, I use the same procedure outlined above, except I skip the part where I dissolve the molecules in the solvent.

The molecules must be drop-cast on the chip before the nanowires are broken. This is not ideal since one would really like to do electromigration prior to deposition in order to preclude damaging the molecule during the breaking process. However, if the molecules are deposited after electromigration, Coulomb blockade has never observed by members of the Ralph group. Although I have no proof, I feel that this might be because it is very difficult for solvent to make its way down the steep walls of the electromigrated junction. Experiments on silicon "nanograss" by researchers at Bell Labs led by Tom N. Krupenkin confirm that liquids often have trouble wetting nanoscale surfaces with severe aspect ratios. However, if molecules are deposited on top of the nanowire prior to electromigration, they are likely to get sucked into the gap somehow during the electromigration process. Whether or not my explanation is valid, researchers have come up with alternative ways to contact molecules which do not involve electromigration that are conducive to SMT experiments [7,8]. However, in my opinion the best SMT work has been done using electromigrated junctions.

Unfortunately, at this time there is no good way to image the molecules in our junctions after breaking the nanowires via low-temperature electromigration. TEM can only be used on electron-transparent substrates, SEM is relatively insensitive to the lighter nuclei of most organic molecules (and the pump oil deposited during imaging does not help matters) and AFM cannot handle the steep side walls of the nanoscale gaps. Therefore, the molecule can only be inferred to be in the gap due to the observation of Coulomb blockade in junctions on which the molecule

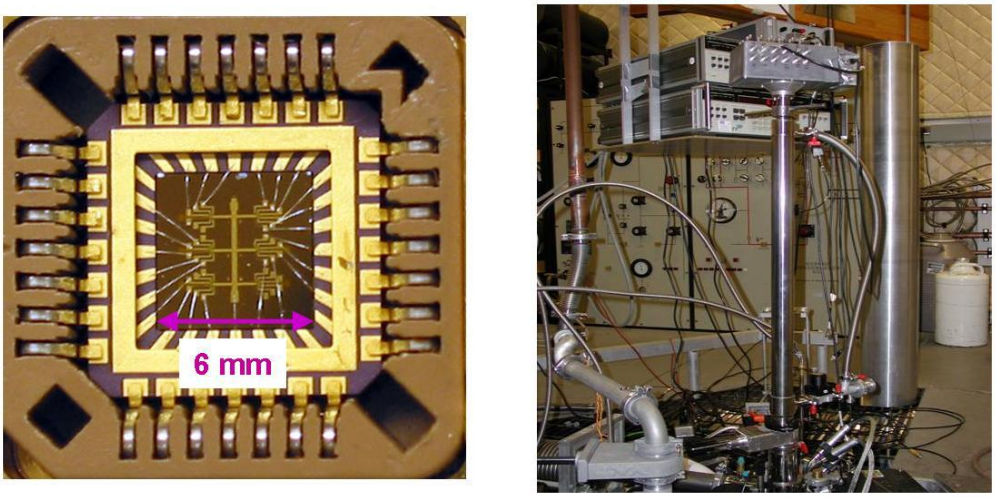


Figure 2.8: Photographs of wirebonded chip mounted on a probe (left) and dilution refrigerator used in the experiments in this thesis. Photographs courtesy Janice Guikema.

has been drop-cast. This illustrates why control experiments are strictly necessary to guard against misinterpreting one's experiments.

2.6 Low-temperature measurements

Figure 2.8 shows images of the chip mounted on the end of a low-temperature probe and the dilution refrigerator used to take the measurements in this thesis. The probes which fit into the top-loading dilution refrigerator only contain 24 wires, so one can contact at most 19 nanowires and 4 gates (along with the common ground). Since measuring SMTs is a statistical process, and since it takes around a day to cool down and warm up a sample, it is crucial that one measures as many wires as possible on each sample. It is for this reason that a common grounding electrode is used, even though one could achieve better noise reduction with separate grounds for each nanowire. More tips on noise reduction can be found in Abhay's thesis [3].

A schematic of the measurement setup used for the Coulomb blockade measure-

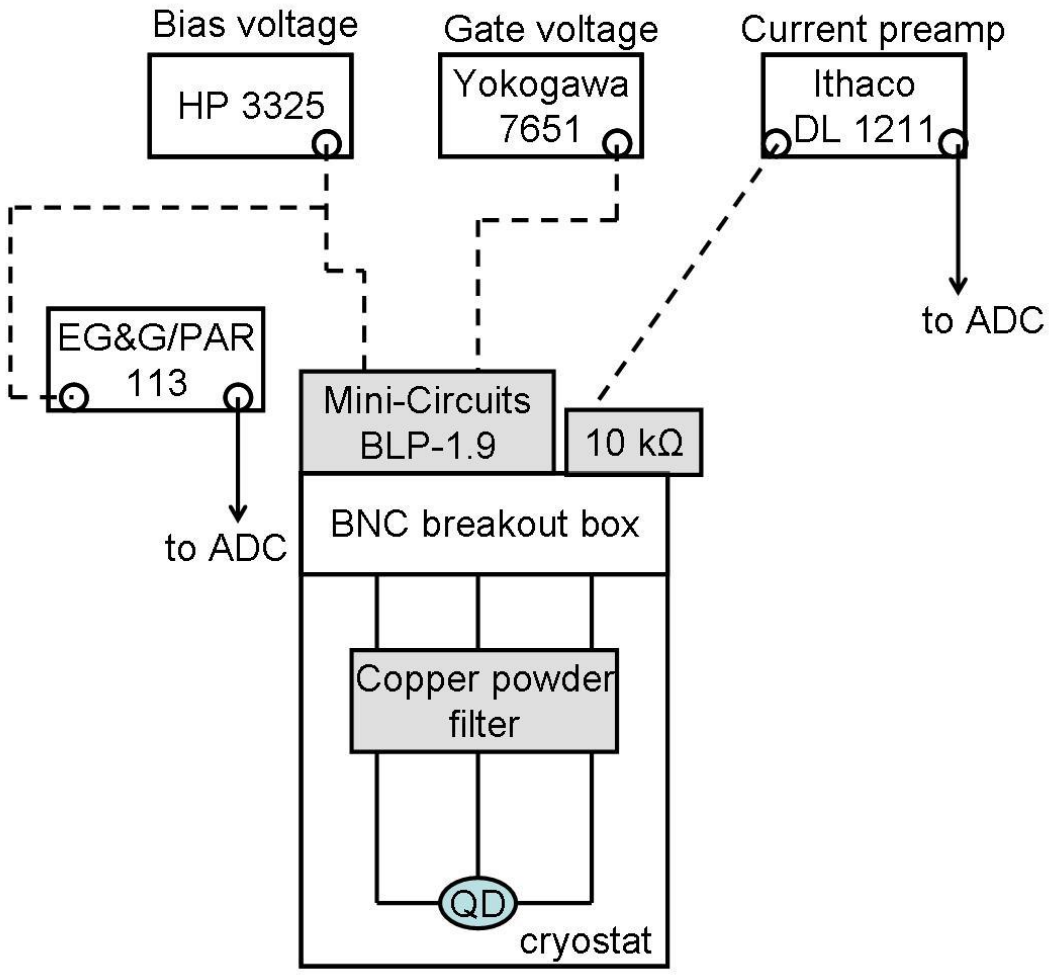


Figure 2.9: Schematic of setup used for the single-molecule transistor measurements in this thesis. The oval inscribed with "QD" (quantum dot) represents the sample being measured. The dotted lines refer to triaxial cables (used for added shielding) which were terminated in triax-to-BNC adapters. After [3].

ments is given in Figure 2.9. To break the wires initially, I used a simpler circuit where the bias voltage is provided by the DAC card and the gate is left floating (to minimize the chances of shorting out the gate during the breaking process). Platinum wires were broken on the new top-loading probe (70 Ω resistance per line) to 50 kΩ (or to 2 V, whichever comes first) without feedback. Once the lines were broken, I typically warmed up the sample and transfered it to the old probe with higher resistance lines. This cumbersome procedure was necessary because the series resistance of the old probe was too high to break the nanowires (see [4]) while the new probe was too noisy for good measurements (I suspect this is due to the unshielded high-frequency SMA lines which terminate next to the sample). Future Ralph group students should look into ways to minimize the noise in the new probe.

Once the chip was transferred to the old probe and inserted back into the fridge, I used the setup in Figure 2.9 to measure Coulomb blockade. I found that the resistances of my Coulomb blockade peaks (typically 1-10 MΩ) were too large to allow for practical lock-in measurements, so I always measured DC currents using the "SETACQ" program (written for CVI) which also numerically differentiated the current with respect to the bias voltage to get conductance values. Virtually all the SMT data in this thesis were taken using the following algorithm:

1. Record current values while sweeping the bias voltage at constant gate voltage or magnetic field.

2. Step the gate voltage or magnetic field.

3. Repeat steps 1 and 2 until the entire parameter range has been swept.

4. Numerically differentiate the current with respect to the bias voltage to get

conductance values.

The setup I used is basically the same setup that Abhay used in his DC Coulomb blockade measurements [3], with a few small changes. I replaced the HP AC function generator that Abhay used to supply the gate voltage with a Yokogawa DC voltage source because the Yokogawa offered better resolution, and, since the gate voltage is not swept during data collection as is the bias voltage, there was no real need for a second AC source. I used π-filters from Mini-Circuits since they were less noisy than the homemade ones Abhay used. I also added a 10 kΩ resistor in series with the current preamplifier to filter out current noise. This is necessary since the Ithaco cannot tolerate any capacitance on its input (thanks to Ferdinand for this suggestion). Of the many noise reduction tricks I have tried, the most effective one is to make sure that the fluorescent lights in the shielded room are turned off during sensitive measurements because they will lead to voltage noise at 64 kHz.

REFERENCES

[1] H. Park, A. K. L. Kim, J. Park, A. P. Alivisatos and P. L. McEuen, Appl. Phys. Lett. **75**, 301 (1999).

[2] H. Park *et al.*, Nature **407**, 57 (2000).

[3] A. N. Pasupathy, *Electron Transport in Molecular Transistors*, Ph.D. thesis, Cornell University, 2004.

[4] T. Taychatanapat, K. I. Bolotin, F. Kuemmeth, and D. C. Ralph, Nano Lett. **7**, 652 (2007).

[5] M. L. Trouwborst, S. J. van der Molen and B. J. van Wees. J. Appl. Phys. **99**, 114316 (2006).

[6] M.-H. Jo and J. E. Grose *et al.*, Nano Lett. **6**, 2014 (2006).

[7] T. Dadosh *et al.*, Nature 436, 677 (2005).

[8] X. Guo *et al.*, Science **311**, 356 (2006).

Chapter 3

Theory of Coulomb blockade in a single-molecule transistor based on a single-molecule magnet

3.1 Theory of Coulomb blockade in single-molecule transistors

Coulomb blockade refers to an increased resistance in a single-electron transistor (SET) at small bias voltages and under certain conditions. An SET consists of a localized "island" of electrons, connected to two metallic electrodes (source and drain) via tunnel barriers and a third electrode (gate) via a capacitor (see Figure 3.1). There are many excellent reviews of SETs, from the basic [1] to the more advanced [2]. Although the "island" of electrons in SETs can be made from GaAs/AlGaAs heterostructures, carbon nanotubes, nanoparticles or single molecules, my discussion in the rest of this chapter will focus on SETs based on single molecules (SMTs). While the discussion and Figures 3.3 and 3.4 in this section are my own, I will augment my text with other figures obtained with permission from the theses of Jiwoong Park [3] and Abhay Pasupathy [4]. These theses are also wonderful references for transport in SMTs in and of themselves. Throughout this chapter, I will assume a negative value of the electron charge (i.e. $e = -|e|$).

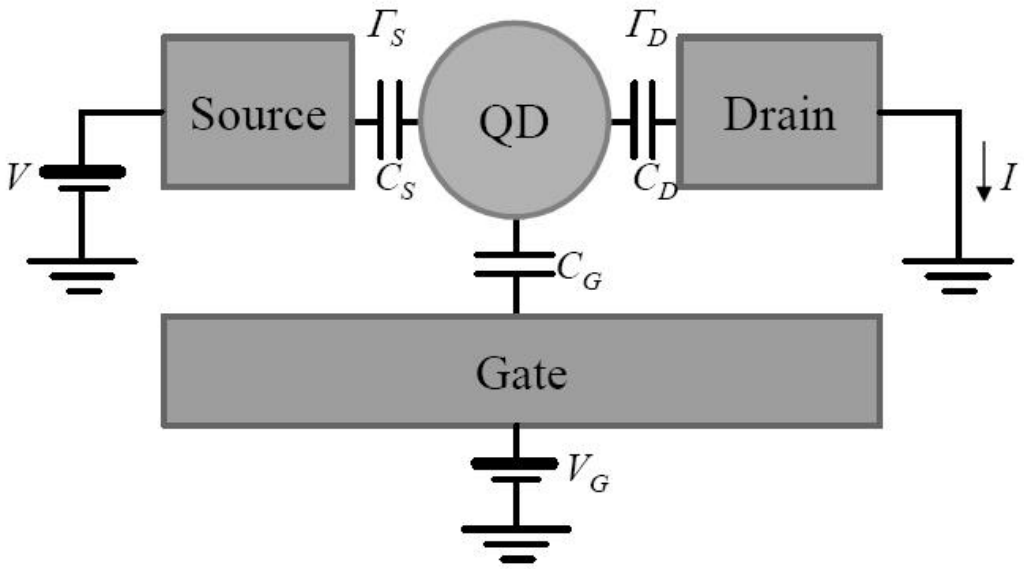


Figure 3.1: Single-electron transistor circuit diagram. From [3].

3.1.1 Definitions and assumptions

Figure 3.1 illustrates the various parameters in an SET. In an SMT, the circle labeled QD (quantum dot) represents a single molecule. The amount of energy it would take to add an electron to a molecule with N electrons is known as the electrochemical potential, μ_{N+1}, which, in this circuit, is defined by the equation below:

$$\mu_{N+1} \equiv U(N+1) - U(N) = E_{cp}(N+1) + E_{sc}(N+1) + E_{cc}(V, V_g), \qquad (3.1)$$

where $U(N)$ is the total energy of the molecule with N electrons, $E_{cp}(N+1)$ is the energy required to add an electron to an N-electron molecule neglecting Coulomb interactions, $E_{sc}(N+1)$ is related to the self-capacitance of the molecule and $E_{cc}(V, V_g)$ is related to the rest of the capacitance in the circuit. Note that the first two terms are functions of N but not of V or V_g, while the opposite is true for the third term.

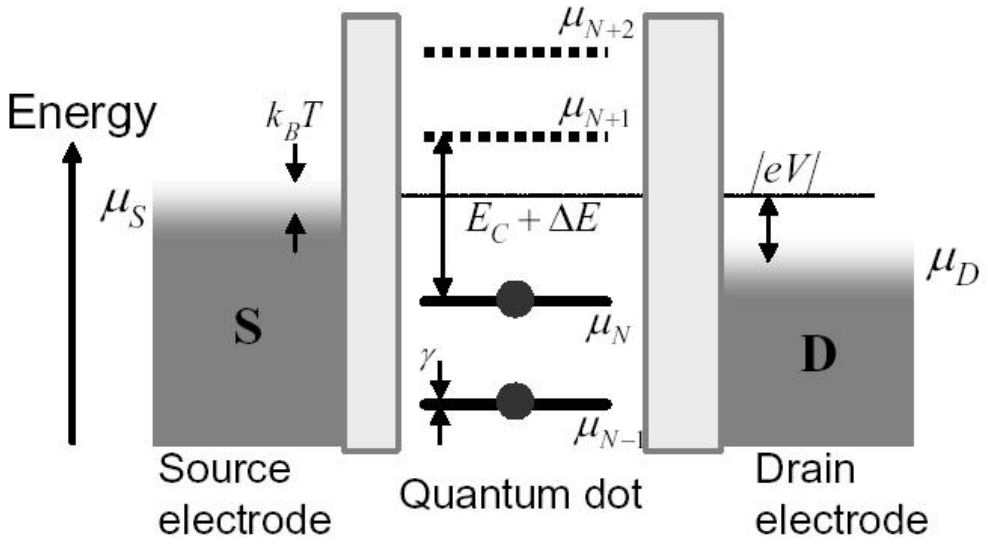


Figure 3.2: Energy scales in a single-molecule transistor. Adapted from [3].

From Figure 3.1, it is clear that:

$$E_{cc}(V, V_g) = \frac{e}{C_\Sigma}(VC_s + V_g C_g), \tag{3.2}$$

where $C_\Sigma \equiv C_s + C_d + C_g$. The reason that there is no term in (3.2) related to the "drain voltage" is that the drain electrode is grounded in all experiments discussed in this thesis.

The difference in energy between the electrochemical potentials μ_N and μ_{N+1} is

$$\mu_{N+1} - \mu_N = E_C + \Delta E, \tag{3.3}$$

where E_C and ΔE are given by

$$E_C \equiv E_{sc}(N+1) - E_{sc}(N) \tag{3.4}$$

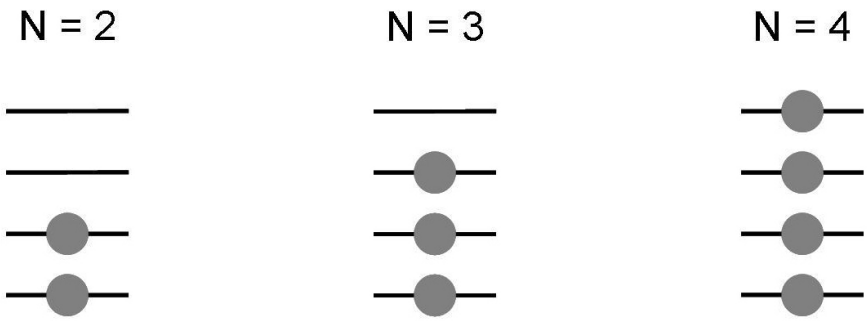
and

$$\Delta E \equiv E_{cp}(N+1) - E_{cp}(N). \tag{3.5}$$

Here, E_C is known as the "charging energy," and ΔE is known as the "level spacing," which in a neutral molecule is equal to the HOMO-LUMO gap or bandgap. It is important to remember that the sum of these energies is not the amount of energy it takes to add an electron to the molecule, but equal to the difference between two electrochemical potentials (see Figure 3.2). Nothing measurable in a Coulomb blockade experiment is dependent on the total energy, U, of a many-body state, but only on μ (the difference between the energies of two many-body states that differ in electron count), S (the total spin) or E_C or ΔE (differences of differences in energy).

Figure 3.3 describes a toy model which should provide some physical intuition to help in understanding quantities such as E_C and ΔE. Although this model gives a value for the charging energy, $E_C = \dfrac{e^2}{C_\Sigma}$, which is generally correct, it assumes that ΔE is independent of N while the energies of real molecular orbitals are clearly not equally spaced like the states of a particle in a box. In addition, the model provides no clues as to how to find ΔE for molecules in between metal electrodes in an SMT, how to estimate C_Σ in real devices, or how to determine where μ_N lies in relation to μ_s and μ_d at zero applied voltage (see [3] for some answers to these questions). Therefore, while this toy model is useful to help gain intuition, it has many limitations arising from its simple assumptions.

I will now list some of the assumptions I will be making in the following sections. These are necessary in order to describe my experiments on SMTs made with single molecules roughly 1 nm in diameter measured at temperatures below 4.2 K. The first three assumptions are that $E_C + \Delta E \gg k_B T, \left|eV^{Max}\right|, \left|e\alpha V_g^{Max}\right|$. Here $\alpha \equiv \frac{C_g}{C_\Sigma}$. These conditions imply that there are only two charge states energetically accessible on the molecule (e.g. N and $N+1$), which (despite a few claims to the



$$U(2) = \frac{4e^2}{2C_\Sigma} + 3(\Delta E) \qquad U(3) = \frac{9e^2}{2C_\Sigma} + 6(\Delta E) \qquad U(4) = \frac{16e^2}{2C_\Sigma} + 10(\Delta E)$$

$$\mu_3 \equiv U(3) - U(2) = \frac{5e^2}{2C_\Sigma} + 3(\Delta E)$$

$$\mu_4 \equiv U(4) - U(3) = \frac{7e^2}{2C_\Sigma} + 4(\Delta E)$$

$$\mu_4 - \mu_3 = \frac{e^2}{C_\Sigma} + \Delta E$$

Figure 3.3: Toy model illustrating charging energy and level spacing. The model assumes a "molecule" with: 1) N electrons and no protons, 2) capacitance C_Σ to the rest of the world, 3) constant level spacing ΔE with no spin degeneracy and 4) $V = V_g = 0$ ($E_{cc} = 0$). These commonly made assumptions imply: $U(N) = \frac{(Ne)^2}{2C_\Sigma} + \sum_{i=1}^{N} i\Delta E$, $\mu_N = (N - 1/2)\frac{e^2}{C_\Sigma} + N\Delta E$ and $\mu_{N+1} - \mu_N = \frac{e^2}{C_\Sigma} + \Delta E$. This last statement implies that $E_C = \frac{e^2}{C_\Sigma}$.

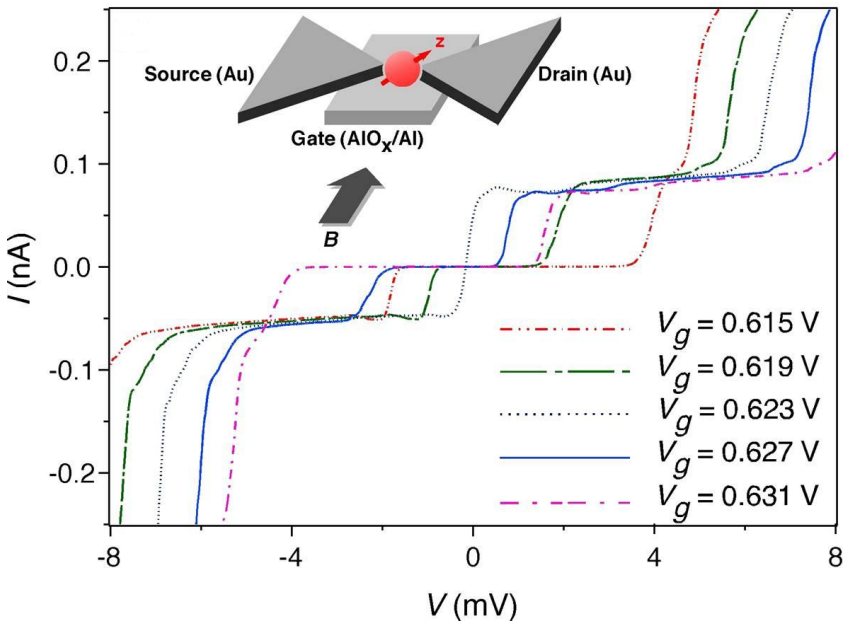


Figure 3.4: Example of "quantum" Coulomb blockade in a single-molecule transistor. From [5].

contrary [6]) is true for all small molecules in real-world SMTs.

The fourth assumption is that the SMT is in the "quantum" Coulomb blockade regime defined by $\Delta E \gg k_B T$, in which the density of states on the molecule is discrete (ignoring degeneracies due to spin), and the current increases in steps beyond the blockade region (see Figure 3.4). This is in contrast to the "classical" Coulomb blockade regime in which the level spacing is much smaller than the temperature, and the current increases continuously beyond the blockade region [4]. Assumptions relating to tunneling rates will be discussed in Subsection 3.3.1.

3.1.2 Ground state transitions

With the definitions and assumptions made in the last subsection, it is now time to describe the phenomenology of Coulomb blockade in SMTs. Figure 3.5 shows two qualitatively different scenarios in an SMT. In Figure 3.5a, no electrochemical

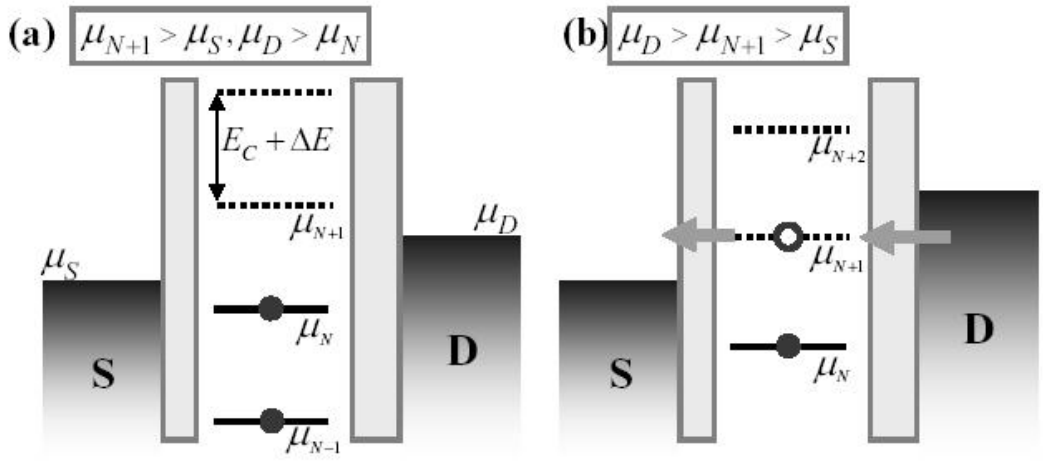


Figure 3.5: Electron transport in a single-electron transistor. In (a), the number of electrons is fixed at N and the current is "blocked." In (b), the number of electrons oscillates between N and $N+1$ and current flow is allowed. Adapted from [3].

potentials of the molecule fall in between the Fermi levels (μ_s and μ_d) of the source and drain electrodes. In this case, resonant tunneling (current flow) through the molecule is energetically "blocked." In contrast, Figure 3.5b shows the case where μ_{N+1} is less than μ_d but greater than μ_s. Here, an electron from the drain electrode has the energy necessary to elastically tunnel onto the molecule (so the molecule goes from having N electrons to having N+1 electrons) and then tunnel again from the molecule to an empty state in the source electrode (bringing the number of electrons on the molecule back to N) where it can relax to the local Fermi energy. Under this scenario, current flow through the molecule is allowed.

Experimenters can control the relative energies of μ_s, μ_d and μ_{N+1} by manipulating the voltages V and V_g. (Since the drain electrode is always grounded, I will assume $\mu_d = 0$ for the rest of this section.) In order to see how this works, I will

begin by rewriting the equation for μ_{N+1}:

$$\mu_{N+1} = E_o + \frac{e}{C_\Sigma}(VC_s + V_g C_g), \tag{3.6}$$

where $E_o \equiv E_{cp}(N+1) + E_{sc}(N+1)$. From (3.6), it is clear that at zero applied bias ($V = \mu_s = \mu_d = 0$), the gate voltage necessary to make μ_{N+1} line up with the Fermi levels of the source and drain is given by

$$V_g = \frac{E_o}{|e|}\frac{C_\Sigma}{C_g} \equiv V_o\,. \tag{3.7}$$

What happens at finite bias? As mentioned above, resonant tunneling occurs when the electrochemical potential of the molecule lies between the Fermi levels of the source and drain. In order to understand at what voltages the Coulomb blockade is lifted, we must look at the two boundary conditions for resonant tunneling, $\mu_{N+1} = \mu_s$ and $\mu_{N+1} = \mu_d = 0$. The first boundary condition, $\mu_{N+1} = \mu_s$, is described by

$$\mu_{N+1} = \frac{|e|\,V_o C_g}{C_\Sigma} + \frac{e}{C_\Sigma}(VC_s + V_g C_g) = eV = \mu_s\,, \tag{3.8}$$

or, solving for V, by

$$V = \frac{C_g}{C_\Sigma - C_s}(V_g - V_o) = \frac{C_g}{C_g + C_d}(V_g - V_o). \tag{3.9}$$

The other boundary condition, $\mu_{N+1} = \mu_d = 0$, is given by

$$V = -\frac{C_g}{C_s}(V_g - V_o). \tag{3.10}$$

The data from SMTs are usually plotted in two-dimensional conductance plots as seen in Figure 3.6, with V_g on the x-axis and V on the y-axis. The colorscale represents differential conductance $\frac{dI}{dV}$, or the derivative of the current through the device with respect to the bias voltage, V. Since, as mentioned previously, SMTs

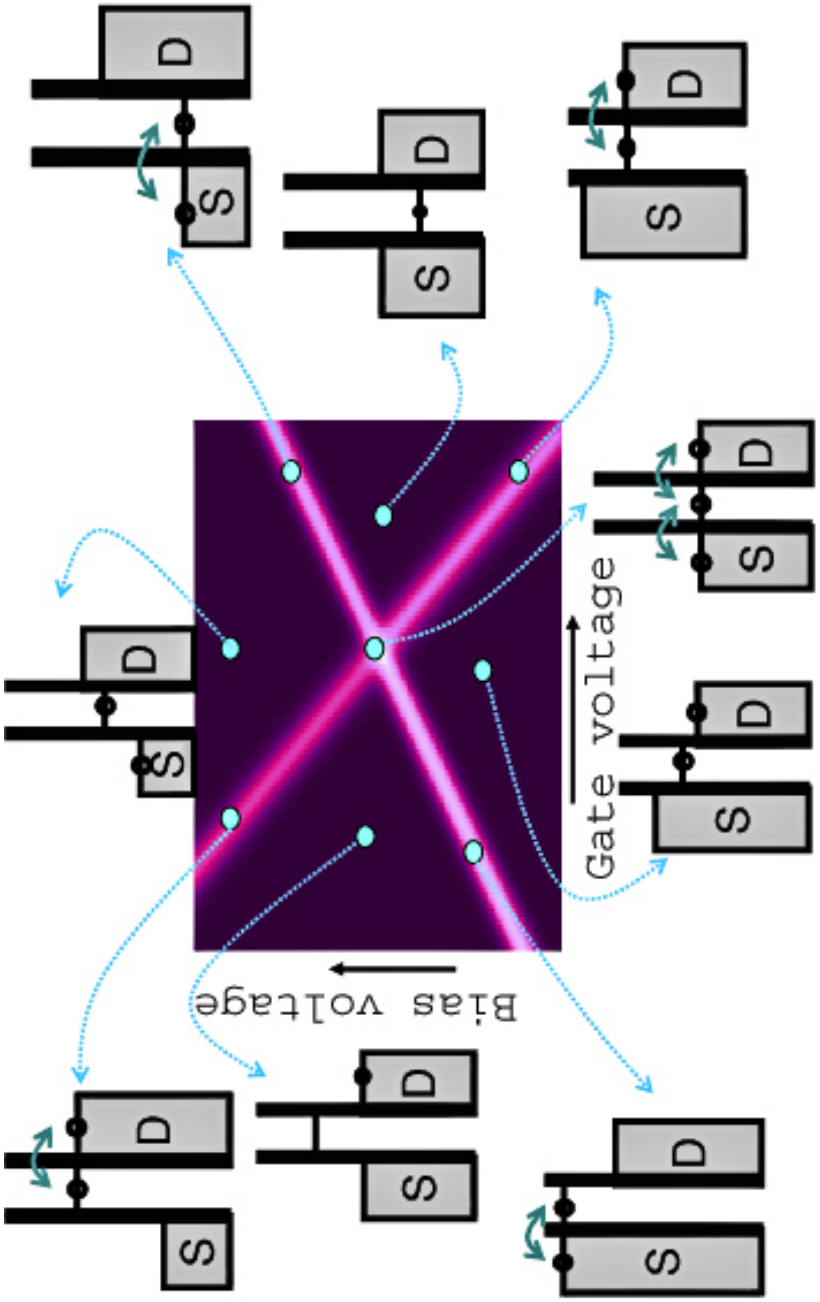


Figure 3.6: Simulation of transport through the ground states of a single-molecule transistor. Cartoons illustrate the relative energies of μ_s, μ_d and μ_{N+1} in various regions of the plot. From [4].

are in the "quantum" limit for Coulomb blockade, there is a peak in conductance at the voltages for which the blockade is lifted. These voltages are defined by equations (3.9) and (3.10). The point on a conductance plot at zero bias where $V_g = V_o$ is known as the "degeneracy point," because this is the point in parameter space where μ_{N+1} is degenerate with the Fermi levels of both the leads.

Figure 3.6 also contains cartoons illustrating the relative energies of μ_s, μ_d and μ_{N+1} in various regions of the plot. At zero bias and smaller gate voltages, the SMT is in the Coulomb blockade regime and the number of electrons on the molecule is fixed at N. At zero bias and larger gate voltages, the SMT is again in the Coulomb blockade regime and the number of electrons on the molecule is fixed at N+1. At finite bias around $V_g = V_o$, μ_{N+1} is between μ_s and μ_d, and current is flowing through the molecule.

3.1.3 Excited state transitions

In the last section, I discussed the simple case where the molecule in an SMT remains in its ground state as the current flow causes the number of electrons on the molecule to toggle from N to N+1. However, often the tunneling electrons couple inelastically to some excitation on the molecule. This excitation could be a center of mass oscillation, a vibrational mode or a magnetic excitation (electronic excitations in molecules are not energetically accessible in my experiments). In any case, inelastic coupling alters the current flow through the molecule in characteristic ways which I will describe below.

First, I will need some new nomenclature in order to describe such a coupling. I will now refer to μ_{N+1} as μ^0_{N+1} in order to reflect the fact that it represents the difference in energy between two ground states, $U^g(N+1)$ and $U^g(N)$. The

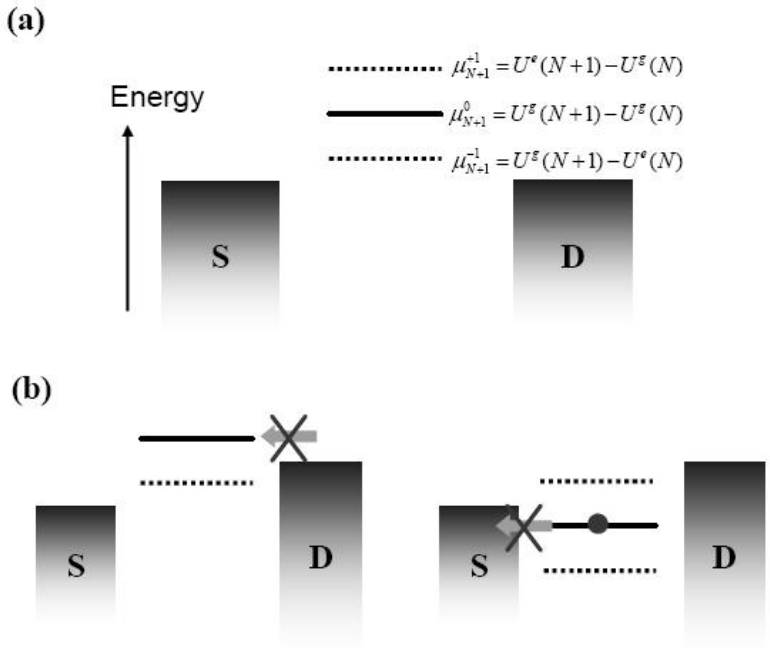


Figure 3.7: Cartoon of excited states in a single-molecule transistor. (a) Electrochemical potentials associated with excited states of either charge state. (b) When only an excited level is within the bias window, current does not flow because the ground state is not available. From [3].

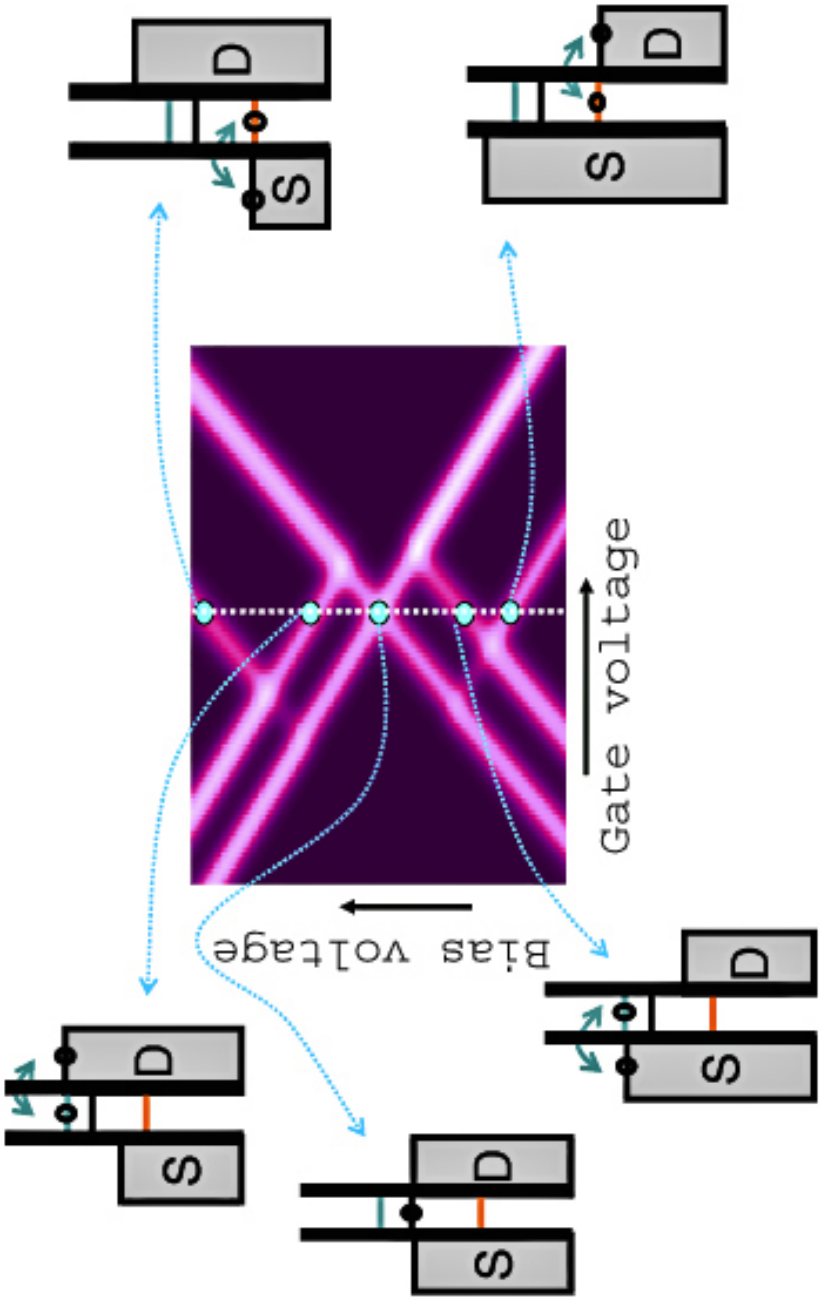


Figure 3.8: Simulation of transport in a single-molecule transistor with excited states. Cartoons illustrate the relative positions of μ_{N+1}^{+1} (top line in blue), μ_{N+1}^{0} (middle line in black) and μ_{N+1}^{-1} (bottom line in orange) with respect to μ_s and μ_d in various regions of the plot. From [4].

electrochemical potential corresponding to the transition between the first excited state of the N+1-electron manifold and the ground state of the N-electron manifold will be called μ_{N+1}^{+1}, while μ_{N+1}^{-1} will represent the potential corresponding to the transition between the ground state of the $N+1$-electron manifold and the first excited state of the N-electron manifold (see Figure 3.7).

A two-dimensional conductance plot for this scenario can be seen in Figure 3.8. This figure also contains cartoons representing the potentials μ_{N+1}^{+1} (top line in blue), μ_{N+1}^{0} (middle line in black) and μ_{N+1}^{-1} (bottom line in orange). As explained in the caption of Figure 3.7, there are additional peaks in conductance when both μ_{N+1}^{0} and one of the other potentials fall within the bias window, but not when only μ_{N+1}^{+1} or μ_{N+1}^{-1} fall within the window.

In Figure 3.9, a simulation of an SMT is presented with a single excited state in the N+1-electron manifold where $\mu_{N+1}^{+1} - \mu_{N+1}^{0} = \Delta E$. ΔE here is unrelated to the ΔE of Subsection 3.1.1. At all points along line L1, the excited level is lined up with the source electrode. At all points along L2, the ground level is lined up with the drain electrode. At point D, which is at the intersection of these lines, both conditions are true, and thus one can find the value of ΔE simply by reading off the value of the source voltage at point D [4].

3.2 Theory of single-molecule magnets

Single-molecule magnets (SMMs) are a class of metal clusters, usually based on manganese or iron, that show intramolecular ferromagnetic behavior at low temperatures [7]. Although most experiments involve van der Waals SMM crystals, there are two recent experiments (including one by the author [5]) which look at SMTs based on Mn_{12} compounds, the most common type of SMM. In this section,

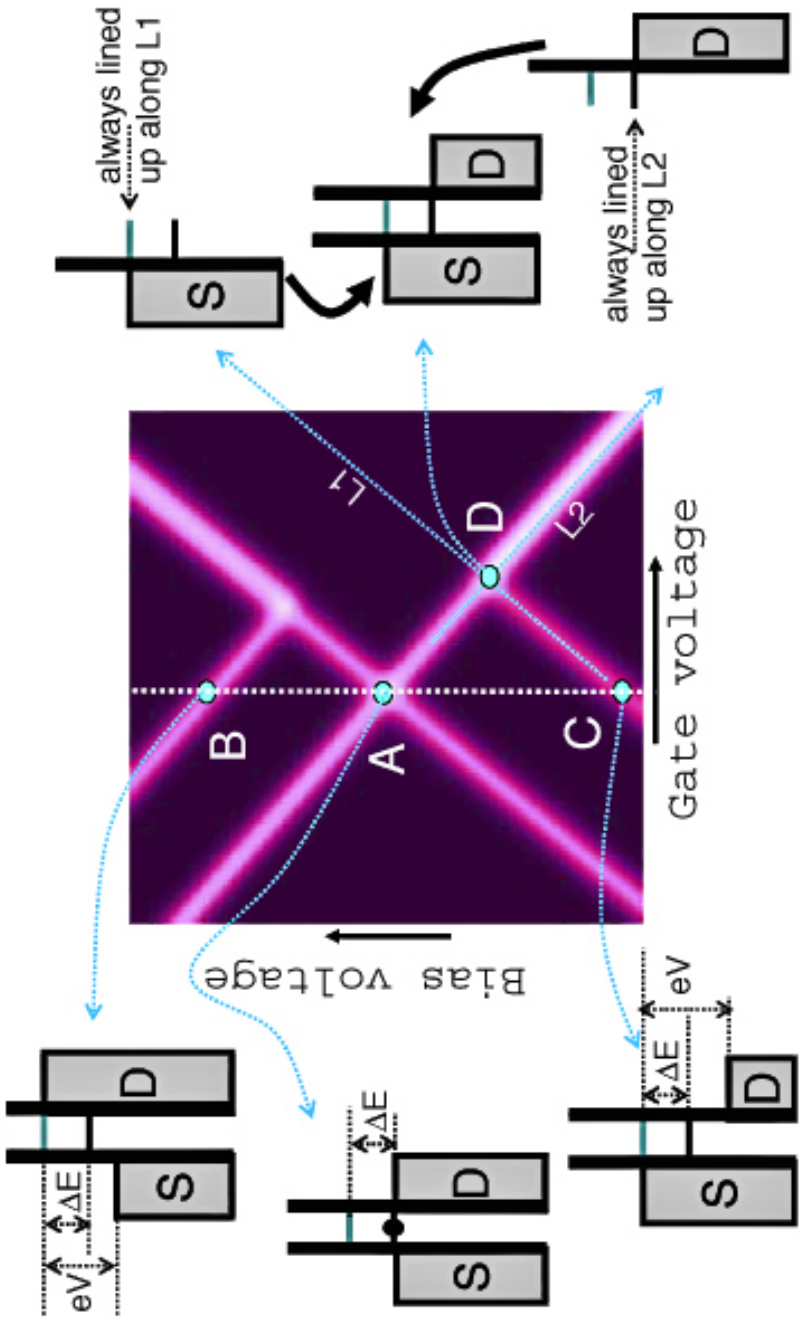


Figure 3.9: Deducing the energy of an excited state. From [4].

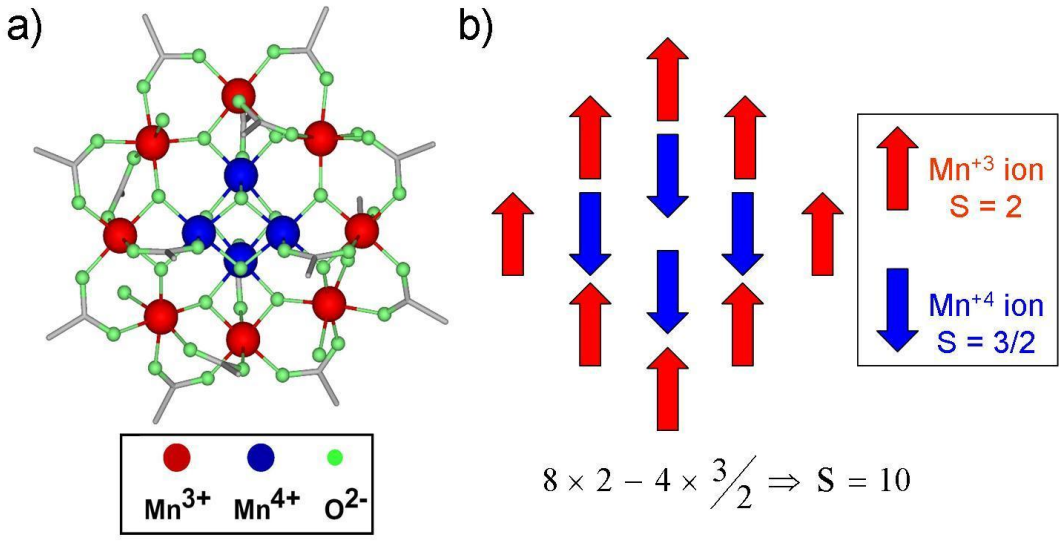


Figure 3.10: Structure of $Mn_{12}Ac$. a) Chemical structure. b) Magnetic structure.

I will review the basic properties of SMMs, often using $Mn_{12}Ac$ (a common Mn_{12} compound, see Figure 3.10) as an example. Theory and simulations of SMTs based on SMMs will be discussed in Section 3.3, while experiments on SMTs based on SMMs will be discussed in Chapter 4.

3.2.1 Magnetic characteristics

Like all SMMs, $Mn_{12}Ac$ is a superparamagnet [7]. In the crystalline form, the molecules in the lattice are very weakly coupled to one another. Intermolecular exchange interactions are negligible [8] because the molecules are far apart in the crystal (the shortest intermolecular distance between metal ions is longer than 7Å) [9]. Intermolecular magnetic dipole interactions, characterized by susceptibility measurements and extrapolation from a Curie-Weiss law, lead to interactions on the order of tens of millikelvin, but whether these interactions are overall antiferromagnetic [10] or ferromagnetic [11] is the source of some controversy. In any

case, it is the combination of a relatively weak *inter*molecular magnetic interaction and a strong *intra*molecular exchange interaction that gives SMMs their uniquely molecular brand of ferromagnetism.

As illustrated in Figure 3.10a, $Mn_{12}Ac$ is composed of 12 manganese ions held together by bridging acetate ligands [7]. Due to the tetragonal symmetry of the molecule, only three of these ions are independent, two in the formal oxidation state of Mn(III) and one in the state of Mn(IV). The fact that the magnetization of $Mn_{12}Ac$ crystals saturates at $20\mu_B$ implies a $S = 10$ ground state with ferrimagnetic coupling. The coupling of the spins of the Mn ions in $Mn_{12}Ac$ is usually understood in terms of a Heisenberg model with four distinct exchange terms (J_i, $i = 1, 2, 3, 4$) to account for superexchange (mediation of the interaction of the Mn ions by the diamagnetic acetate bridges). In a simpler model, the central four Mn(IV) ions (each with spin 3/2) are coupled ferromagnetically, as are the eight outer Mn(III) ions (each with spin 2). Since in this model the coupling between the Mn(III) and Mn(IV) ions is antiferromagnetic, it is easy to see that the interactions would lead to a ferrimagnetic $S = 10$ ground state ($8 \times 2 - 4 \times \frac{3}{2} = 10$, see Figure 3.10b).

Although the magnetization both parallel and perpendicular to the tetragonal axis reach the same saturation value of $20\mu_B$, the former curve increases much more rapidly than the latter, indicating the presence of a large easy-axis magnetic anisotropy. The primary physical origin of this anisotropy lies in the single-ion anisotropy of the Jahn-Teller-distorted Mn(III) ions [7].

Upon cooling an SMM crystal at zero field, the magnetization of each molecule will lock in a direction either parallel or anti-parallel to the molecular easy axis [11]. Since intermolecular interactions are weak, there is no spontaneous magnetization,

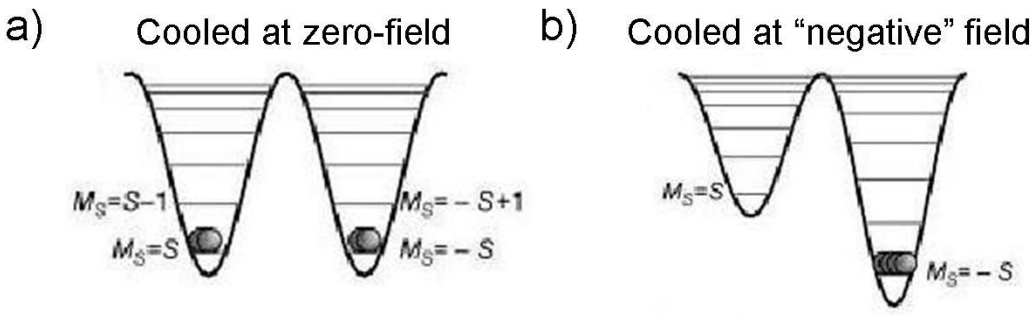


Figure 3.11: Magnetization of single-molecule magnet crystals during cooling. Adapted from [7].

and a $Mn_{12}Ac$ crystal will have no net magnetization upon zero-field cooling (see Figure 3.11a). However, if the crystal is cooled at high fields, the magnetization will saturate at $20\mu_B$ (see Figure 3.11b) and hysteresis can be observed. Thus at low temperatures, a $Mn_{12}Ac$ crystal is best described as an ensemble of weakly-interacting, anisotropic ferrimagnets, as opposed to the simplistic definition of a "ferromagnet."

3.2.2 Hamiltonian and zero-field splitting

The simplest effective Hamiltonian[1] (with non-trivial anisotropy) that one can write for the lowest-energy spin multiplet of an SMM is

$$\mathscr{H} = DS_z^2 - g\mu_B \boldsymbol{S} \cdot \boldsymbol{B}, \tag{3.11}$$

where D is a negative constant with dimensions of energy corresponding to the strength of the anisotropy [7]. (For $Mn_{12}Ac$, $D = -57\,\mu$eV and $g = 2$.) Although there is EPR evidence for an $S = 9$ excited multiplet roughly 4 meV above the ground-state $S = 10$ multiplet in an Mn_{12} derivative [12], for simplicity I will focus my attention on the ground-state multiplet in this chapter.

[1] In (3.11) and (3.14), S_z, S_x and $\boldsymbol{S}$ are the standard spin operators divided by $\hbar$. In the text, S and S_z refer to quantum numbers.

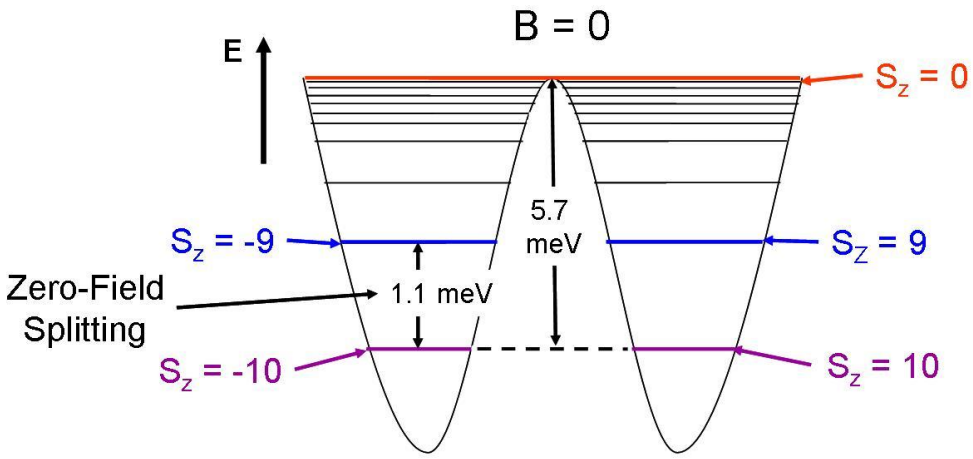


Figure 3.12: Mn_{12} energy-level diagram for the $S = 10$ multiplet at zero field.

The Hamiltonian in (3.11) leads to a "zero-field splitting" of the $S = 10$ multiplet (see Figure 3.12). The $S_z = \pm m$ states remain degenerate at zero applied field, but the $S_z = \pm 10$ ground states are separated from the $S_z = \pm 9$ states by

$$E_{S_z=9} - E_{S_z=10} = D(81 - 100) = 1.1\,\text{meV}\,(12.5\text{K}). \tag{3.12}$$

As is clear from (3.11), the zero-field splitting between consecutive energy levels gets smaller as S_z goes from $\pm 10 \to 0$. The height of the barrier to thermally activated magnetic relaxation (the "Curie temperature" of the molecule) is given by

$$E_{S_z=0} - E_{S_z=10} = 57\,\text{meV}\,(66\text{K}). \tag{3.13}$$

3.2.3 Hysteresis and quantum tunneling of the magnetization

One of the most characteristic features of a ferromagnet is a hysteresis loop of the magnetization as a function of applied field. Like all superparamagnets, SMMs exhibit hysteresis loops below their blocking temperatures, but SMM hysteresis loops have unique features related to thermally assisted quantum tunneling of the

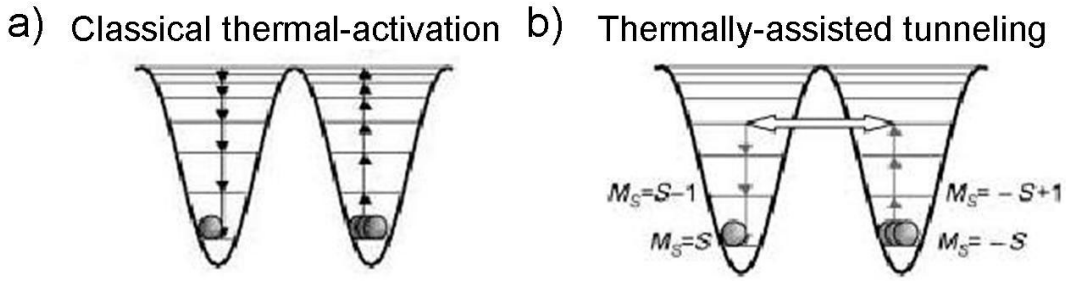


Figure 3.13: Thermal relaxation of the magnetization in SMMs. a) Molecules are thermally excited from the $S_z = -S$ ground state over the barrier to the $S_z = 0$ state, from where the magnetization relaxes randomly. b) Molecules are thermally excited to an intermediate excited state where the tunnel barrier is small enough to allow tunneling on reasonable time scales. Adapted from [7].

magnetization (QTM) from a "spin up" to a "spin down" state. SMMs are the perfect objects in which to observe QTM, since their tunneling barriers are much smaller than that of macroscopic magnets, and yet their blocking temperatures are high enough to prevent thermal relaxation at cryogenic temperatures.

When a crystal is exposed to a large magnetic field parallel to the easy axis, the moment of the crystal reaches its saturation value. When the field is suddenly turned off, there is a characteristic time for the system to return to equilibrium. For a Mn_{12}Ac crystal at temperatures from 2 K to 10 K, the decay is exponential, $M_z(t) = M_z(t = 0)e^{-t/\tau}$ [7]. The relaxation time τ is well approximated by an Arrhenius law, $\tau = \tau_o e^{\Delta E/k_B T}$, where ΔE (the height of the anisotropy barrier) is 62 K. From experimental evidence, it is known that the attempt time for Mn_{12}Ac is $\tau_o = 2.1 \times 10^{-7}$s [7], leading to relaxation times on the order of months at 2 K that are more than sufficient for experimental observation of hysteresis.

If there were no QTM, τ would be the characteristic time it would take for molecules in the crystal to be thermally excited at zero field from the saturation

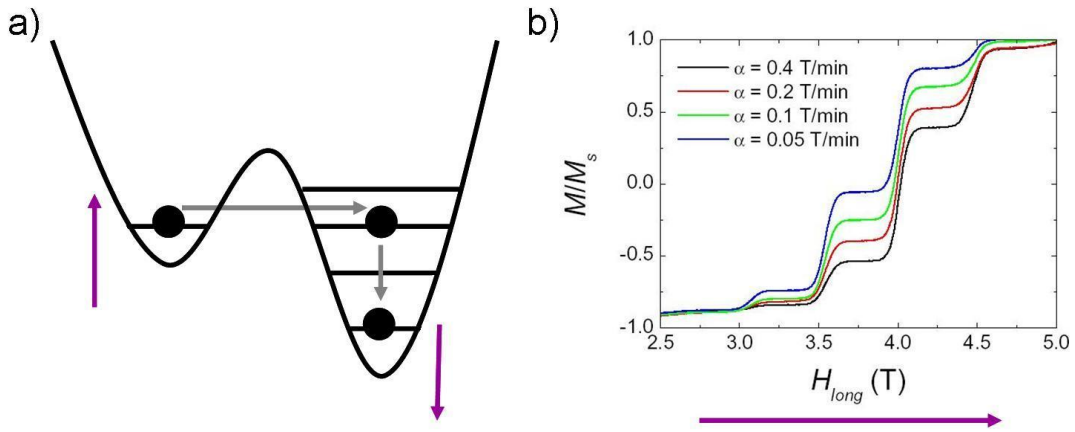


Figure 3.14: Quantum tunneling of the magnetization in $Mn_{12}Ac$ crystals. a) Cartoon of QTM at finite field. b) Dependence of one side of the magnetic hysteresis loop on field-sweep rate. Data taken at 600 mK, adapted from [13].

value[2] of $S_z = -10$ up to the $S_z = 0$ state (see Figure 3.13a). This thermal excitation would randomize the magnetization of the crystal as the individual molecules relax from their excited $S_z = 0$ state. The reason that the empirical fit of τ from 2 K to 10 K is slightly lower than the barrier height implied by (3.13) is due to thermally-assisted tunneling [7]. Thermally-assisted tunneling (see Figure 3.13b) occurs when an SMM molecule is thermally excited to an intermediate state (say $S_z = -6$) and then tunnels through the barrier into the corresponding "spin down" state ($S_z = 6$). Since thermally-assisted tunneling provides a shortcut to magnetic relaxation, it serves to lower the effective Arrhenius barrier.

I should note that in the simple Hamiltonian presented in (3.11), there would be no quantum tunneling at all for a field parallel to the easy axis because there would be no matrix element connecting the various S_z states. However, due to higher-order anisotropic terms and transverse field terms in the true Hamiltonian, such tunneling is observed experimentally, as is a tunnel splitting Δ [13].

[2]For the rest of this section, I will assume the system was prepared in a "negative" magnetic field so that the initial state of the molecules is $S_z = -10$.

In Mn_{12}Ac crystals below 2 K, there is no longer enough energy to allow the magnetization to relax thermally, so there is a crossover from a thermally assisted tunneling regime to a quantum tunneling regime [7]. At zero field, the tunneling barrier is large, making the transition $S_z = \pm 10 \rightarrow \mp 10$ a very rare event (as mentioned above, τ is on the order of months). However, at finite fields parallel to the easy axis, tunneling can occur between other states that are degenerate in energy as long as the tunneling barriers between the states are small enough to allow the tunneling to occur on experimental time scales (see Figure 3.14a).

From (3.11), it is clear that the longitudinal fields at which pairs of levels become degenerate is given by the equation $B_z^n = \frac{nD}{g\mu_B} = 0.44n$ T, where n is equal to -1 times the sum of the S_z values of the levels in question (e.g. $S_z = +10, -10 \Rightarrow n = 0$; $S_z = +9, -10 \Rightarrow n = 1$; and so on). In the quantum tunneling regime, QTM leads to characteristic "steps" in the hysteresis loop at values of $B_z^n = 0.44n$ T corresponding to pairs of levels with small tunnel barriers. The details of these steps depend on the sweep rate of the applied field because the slower the field is swept, the longer the molecules will remain on a given resonance which means that more QTM will occur at resonances corresponding to lower values of magnetic field (see Figure 3.14b).

3.3 Simulations of Coulomb blockade in single-molecule magnets

In this section, I will discuss some Mathematica simulations of SMTs based on Mn_{12} compounds [5]. These simulations are based on the SET simulations of two former Ralph group members, Mandar Deshmukh and Edgar Bonet [14,15]. Even

though these simulations were done using the simplest assumptions (see below), they are still fairly complicated, so I will be forced to introduce a fair amount of notation to describe them. For the interested reader, the Mathematica notebooks used to generate the simulations presented in this section will be available on the Ralph group website.

3.3.1 Assumptions related to tunneling rates

I will make the following assumptions for the sake of simplicity of my simulation, even though they may not be entirely physically accurate. Future simulations should seek to improve on these limitations. First, I will assume that the tunnel barriers have resistances, $R \gg h/e^2$, so that higher order tunneling processes can be neglected [15]. I had tacitly made this assumption in Section 3.1, and will make this assumption in this section despite the fact that cotunneling processes have been observed in some of our Mn_{12} SMTs (see Chapter 4).

With the tunnel barriers separating the molecule from the electrodes given by Γ_s and Γ_d, the lifetime of the electron on the molecule is given by $\tau \sim (\Gamma_s + \Gamma_d)^{-1}$ and the intrinsic broadening by $\gamma = h(\Gamma_s + \Gamma_d)$. My second assumption is that $\gamma \ll k_B T$, although under experimental conditions γ can be on the order of $k_B T$ [3]. Thirdly, I will assume that magnetic relaxation in the molecule is slow compared to the tunneling rates. This allows there to be significant probability that the molecule remains in an excited state during the course of many tunneling events and will be crucial in allowing for magnetic relaxation of the molecule via tunneling.

A fourth assumption I make is that the tunneling in SMM-based SMTs is incoherent, and thus I can use a simple rate-equation approach [14,15]. While Braig and Brouwer state that this assumption is valid in steady-state models of SETs with

non-magnetic leads (or magnetic leads in which the magnetization is collinear) [16], it is less clear whether I am justified in incoherently changing the basis of the probability vector in the iterative simulation described in Subsection 3.3.4.

My last assumption is that only the lowest-energy multiplets of each charge state are involved in the tunneling process. In other words, if the Mn_{12} molecule is toggling between the 1^+ and neutral charge states, I will assume that only the $S = 19/2$ and $S = 10$ multiplets are accessible. Although as mentioned in Subsection 3.2.2 the $S = 9$ multiplet may lie close to the $S = 10$ multiplet in the neutral molecule, it would be too computationally expensive to include higher multiplets in the simulation. Although one group claims to see evidence of the $S = 9$ multiplet in tunneling spectra from Mn_{12}-based SMTs [17], we did not see conclusive signs of an $S = 9$ multiplet in our experiments discussed in Chapter 4 and in reference [5].

3.3.2 Transition rates via Clebsch-Gordon coefficients

Because the anisotropy in (3.11) has only a z-component, that the x- and y-directions are equivalent, and so I can take the magnetic field to be in the x-z plane without loss of generality. Therefore, the Hamiltonian used in the simulation to describe a N-electron molecule with spin S is

$$\mathscr{H}_N = D_N S_{z,N}^2 - g\mu_B B S_{z,N} \cos\theta - g\mu_B B S_{x,N} \sin\theta, \tag{3.14}$$

where D_N is the anisotropy term and θ is the angle between the applied field and the magnetic easy-axis.

Coulomb blockade involves transport between two charge states. For the Mn_{12} simulations presented here, I will assume that the transitions are between states

composed of a Mn_{12}^{+}, S=19/2 multiplet and states composed of a neutral Mn_{12}, S=10 multiplet, although other choices of charge (spin) states produce qualitatively similar results provided the difference in total charge (spin) remains e (1/2). The SMT simulations are based on a 41-dimensional master equation,

$$\frac{d}{dt}\boldsymbol{P} = \boldsymbol{\Gamma} \cdot \boldsymbol{P}, \tag{3.15}$$

where $\boldsymbol{P}$ is a vector whose components represent the probability of being in each state of the system and Γ is a matrix representing the transition rates between various states [14, 15].

Before I can write down this 41-dimensional master equation, I must first establish a basis, and the natural basis for this equation is made from the eigenvectors of the Hamiltonian in (3.14). For Mn_{12}^{+} (S=19/2) there are 20 ($2S$+1) eigenvectors: $\boldsymbol{v}^{+,i}$, i = 0–19. For neutral Mn_{12} (S=10) there are another 21 eigenvectors: $\boldsymbol{v}^{n,j}$, j = 0–20. All possible states of the Mn_{12} molecule can be written as a linear combination of these 41 eigenvectors. I will arrange the eigenvectors of Mn_{12}^{+} in order of increasing energy so that $\boldsymbol{v}^{+,0}$ is the ground state and arrange the eigenvectors of neutral Mn_{12} in a similar fashion. If I then adopt a notation where $P^{+,i}$ represents the probability that the molecule is in the eigenstate $\boldsymbol{v}^{+,i}$ of the Mn_{12}^{+} Hamiltonian, and $P^{n,j}$ represents the probability that the molecule is in the eigenstate $\boldsymbol{v}^{n,j}$ of the neutral Mn_{12} Hamiltonian, I can write $\boldsymbol{P}$ as a 41-dimensional

vector:

$$\boldsymbol{P} = \begin{pmatrix} P^{+,0} \\ \vdots \\ P^{+,19} \\ P^{n,0} \\ \vdots \\ P^{n,20} \end{pmatrix}. \tag{3.16}$$

The next problem is how to write $\boldsymbol{\Gamma}$. In order to answer this, I will temporarily assume that Mn_{12}^{+} has spin S=1/2, and neutral Mn_{12} has spin S=1, so that I can work with a 5-dimensional $\boldsymbol{\Gamma}$ instead of a 41-dimensional $\boldsymbol{\Gamma}$ (the results will generalize easily). Following [15], I can write

$$\boldsymbol{\Gamma} = \left(\begin{array}{cc|ccc} -\sum_{j=0}^{2} R_{n,j}^{+,0} & 0 & R_{+,0}^{n,0} & R_{+,0}^{n,1} & R_{+,0}^{n,2} \\ 0 & -\sum_{j=0}^{2} R_{n,j}^{+,1} & R_{+,1}^{n,0} & R_{+,1}^{n,1} & R_{+,1}^{n,2} \\ \hline R_{n,0}^{+,0} & R_{n,0}^{+,1} & -\sum_{i=0}^{1} R_{+,i}^{n,0} & 0 & 0 \\ R_{n,1}^{+,0} & R_{n,1}^{+,1} & 0 & -\sum_{i=0}^{1} R_{+,i}^{n,1} & 0 \\ R_{n,2}^{+,0} & R_{n,2}^{+,1} & 0 & 0 & -\sum_{i=0}^{1} R_{+,i}^{n,2} \end{array}\right), \tag{3.17}$$

where $R_{n,j}^{+,i}$ represents the transition rate from the i^{th} excited state of Mn_{12}^{+} to the j^{th} excited state of neutral Mn_{12}, and $R_{+,i}^{n,j}$ represents the transition rate from the j^{th} excited state of neutral Mn_{12} to the i^{th} excited state of Mn_{12}^{+}. This matrix has the structure

$$\boldsymbol{\Gamma} = \left(\begin{array}{c|c} \boldsymbol{\Gamma}_{++} & \boldsymbol{\Gamma}_{+}^{n} \\ \hline \boldsymbol{\Gamma}_{n}^{+} & \boldsymbol{\Gamma}_{nn} \end{array}\right), \tag{3.18}$$

where $\boldsymbol{\Gamma}_{++}$ and $\boldsymbol{\Gamma}_{nn}$ are diagonal blocks corresponding respectively to the rates of depopulating the Mn_{12}^{+} and neutral Mn_{12} states respectively. The cross-diagonal

blocks correspond to tunneling off of ($\mathbf{\Gamma}^n_+$) and onto ($\mathbf{\Gamma}^+_n$) the molecule. The general structure of (3.18) holds whether $\mathbf{\Gamma}$ is 5-dimensional or 41-dimensional.

From (3.17), it is clear that I will have to solve for the tunneling rates in order to have an explicit form for $\mathbf{\Gamma}$. These tunneling rates are the product of two terms, a term related to the relative energy of the electrochemical potential of the molecular orbital in relation to the Fermi levels of the leads, and a term related to Clebsch-Gordon coefficients. The first term is given by either $(\Gamma_s f_s + \Gamma_d f_d)$ or $(\Gamma_s(1-f_s) + \Gamma_d(1-f_d))$ depending on whether the rate corresponds to an electron tunneling onto or off of the molecule. Here, Γ_s and Γ_d are the bare tunneling rates defined in Section 3.1, while f_s and f_d are Fermi functions defined below [3]:

$$\begin{aligned} f_d &= \left(1+\exp\left(\frac{\mu_{N+1}-\mu_d}{k_BT}\right)\right)^{-1} = \left(1+\exp\left(\frac{\mu_{N+1}}{k_BT}\right)\right)^{-1} \\ f_s &= \left(1+\exp\left(\frac{\mu_{N+1}-\mu_s}{k_BT}\right)\right)^{-1} = \left(1+\exp\left(\frac{\mu_{N+1}+|e|\,V}{k_BT}\right)\right)^{-1} \\ \mu_{N+1} &= E_o - |e|\,\frac{C_gV_g + C_sV}{C_\Sigma}. \end{aligned} \tag{3.19}$$

For the purposes of the simulation, I defined

$$E_o \equiv \left(U^i(n) - U^j(+)\right) - \left(U^0_{B=0}(n) - U^0_{B=0}(+)\right). \tag{3.20}$$

Since transport in SMTs involves the tunneling of a $S=\frac{1}{2}$ electron onto and off of the molecule, the second term contributing to the tunneling rates is related to the Clebsch-Gordon coefficients, $C^{\frac{19}{2},\frac{1}{2},10}_{m_+,\pm\frac{1}{2},m_n}$, where m_+ is the z-component of the Mn^+_{12} spin and m_n is the z-component of the neutral Mn_{12} spin. If I work in a basis in which the eigenvectors of the Mn^+_{12} and Mn_{12} Hamiltonians are written respectively as

$$\boldsymbol{v}^{+,i} = \begin{pmatrix} v_0^{+,i} \\ \vdots \\ v_{19}^{+,i} \end{pmatrix} \text{ and } \boldsymbol{v}^{n,j} = \begin{pmatrix} v_0^{n,j} \\ \vdots \\ v_{20}^{n,j} \end{pmatrix}, \tag{3.21}$$

where v_0 corresponds to $S_z = S$ and v_{2S} corresponds to $S_z = -S$, then the tunneling matrix element between eigenstates $\boldsymbol{v}^{+,i}$ and $\boldsymbol{v}^{n,j}$ is proportional to

$$R_{\mathrm{CG}}^{i,j} \equiv \frac{1}{2}\left(\sum_{k=0}^{19} C^{\frac{19}{2},\frac{1}{2},10}_{(\frac{19}{2}-k),\frac{1}{2},(10-k)}\, v_k^{+,i}\, v_k^{n,j}\right)^2 + \frac{1}{2}\left(\sum_{k=0}^{19} C^{\frac{19}{2},\frac{1}{2},10}_{(\frac{19}{2}-k),-\frac{1}{2},(9-k)}\, v_k^{+,i}\, v_{k+1}^{n,j}\right)^2. \tag{3.22}$$

The first term in (3.22) is the rate associated with tunneling a "spin up" electron while the second term is the rate associated with tunneling a "spin down" electron. The factor of $\frac{1}{2}$ in front comes from the assumption that the electrodes are nonmagnetic, and so there is equal probability that the tunneling electron is "spin up" or "spin down."

Putting everything together, the matrix $\boldsymbol{\Gamma}$ can be constructed as in (3.17), with

$$R_{n,j}^{+,i} = R_{\mathrm{CG}}^{i,j}(\Gamma_s f_s + \Gamma_d f_d) \tag{3.23}$$

and

$$R_{+,i}^{n,j} = R_{\mathrm{CG}}^{i,j}(\Gamma_s(1-f_s) + \Gamma_d(1-f_d)), \tag{3.24}$$

where $R_{\mathrm{CG}}^{i,j}$ is defined by (3.22), Γ_s and Γ_d are bare tunneling rates and f_s and f_d are defined by (3.19) and (3.20).

3.3.3 Steady-state simulations of magnetic randomization and anisotropy

If one wants to model steady-state current flow through an SMT without regard for hysteresis, the algorithm is relatively straightforward. For a given set of input parameters: $\{V,\ V_g,\ B,\ D_+,\ D_n,\ g,\ \theta,\ k_BT,\ \Gamma_s,\ \Gamma_d,\ C_s{:}C_d{:}C_g\}$, one can calculate $\boldsymbol{\Gamma}$ as in the previous subsection. The steady-state probability vector, $\boldsymbol{P}_{ss}$, in accordance with (3.15) is equal to the eigenvector of $\boldsymbol{\Gamma}$ corresponding to eigenvalue 0.

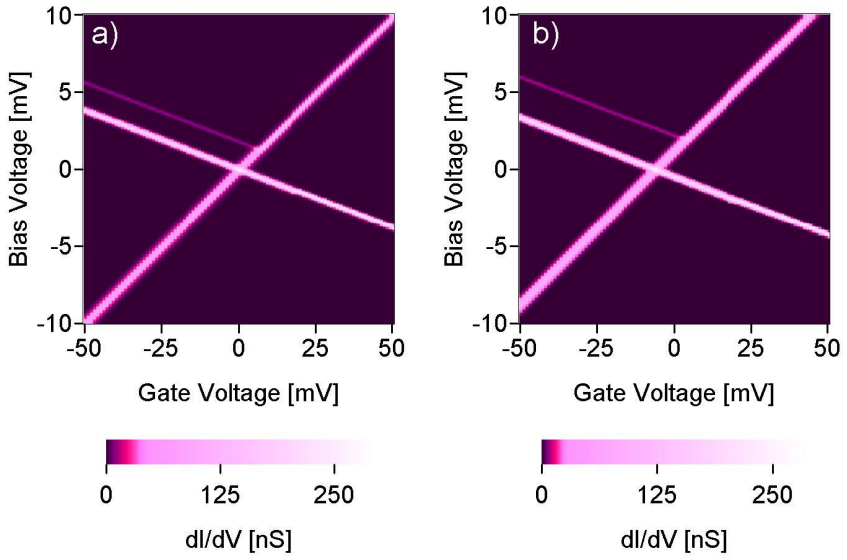


Figure 3.15: Steady-state simulations of magnetic excitations in the tunneling spectra of a Mn_{12}-based SMT. The parameters used here are: $D_+ = D_n = -0.071$ meV, $g = 2.0$, $\theta = 45^o$, $T = 0.5$ K, $\Gamma_s = 8$ GHz, $\Gamma_d = 0.8$ GHz and C_s:C_d:C_g=1:13:4. a) Zero-field splitting. b) Increased splitting at $B = 8$ T.

Due to conservation of charge, the total current must be equal to both the current flow from the source electrode to the molecule, and to the current flow from the molecule to the drain electrode. Therefore, in order to calculate the current, I must first define new tunneling rates which only take into account current flow across one barrier. I will arbitrarily choose to calculate current flow from the source electrode and define the tunneling rates: $R^{+,i}_{n,j,s} \equiv R^{i,j}_{CG}\Gamma_s f_s$ and $R^{n,j}_{+,i,s} \equiv R^{i,j}_{CG}\Gamma_s(1 - f_s)$. With these definitions, the current flow through the Mn_{12} SMT is given by

$$I = e\left[\sum_{i=0}^{19}\sum_{j=0}^{20}\left(R^{+,i}_{n,j,s}P^{+,i}_{ss}\right) - \sum_{i=0}^{19}\sum_{j=0}^{20}\left(R^{n,j}_{+,i,s}P^{n,j}_{ss}\right)\right]. \tag{3.25}$$

Two steady-state simulations of Coulomb blockade are pictured in Figure 3.15. At $B = 0$ T and $B = 8$ T, there is only one excited state corresponding to the Mn_{12} multiplet, whereas from (3.14) one might expect ten excited states corresponding to

the Mn_{12} multiplet and nine excited states corresponding to the Mn_{12}^{+} multiplet at $B = 0$ T, and at least as many excited states at $B = 8$ T. The reason there is only one excited state is, as seen in Figure 3.12, the level spacing in Mn_{12} decreases as the excited states become higher in energy. Therefore, the largest energy difference between two different electrochemical potentials which differ in S_z by 1/2 is given by $\mu(S_z = 19/2 \leftrightarrow 9) - \mu(S_z = 19/2 \leftrightarrow 10) \equiv \mu_n^{+1} - \mu_n^0$, following the notation of Figure 3.7. This implies that if there is sufficient bias to allow for current flow through the μ_n^{+1} level, then there is sufficient bias to allow for current flow through all excited levels, and thus only one excited state appears in the tunneling spectra.

The explanation presented in the last paragraph is subtle, so let's take a moment to understand what is going on via the energy diagram in Figure 3.16. The discussion below will assume $B = 0$ T for simplicity, although the gist of the argument holds at all fields. At zero field, the $S_z = 10$ state in the Mn_{12} multiplet is separated from the $S_z = 9$ state by 1.1 meV (see Figure 3.12). Therefore, at biases below 1.1 mV, only ground state to ground state tunneling is allowed energetically. In other words, there is only enough energy for a "spin up" electron to tunnel onto and off of the molecule ($S_z : 19/2 \leftrightarrow 10$). However, at biases greater than 1.1 mV, there is enough energy for a "spin down" electron to tunnel onto the molecule, which means that the $S_z = 9$ state becomes energetically accessible. Once the molecule is in the $S_z = 9$ state, there is nothing stopping a "spin up" electron from tunneling off, leaving the molecule in the $S_z = 17/2$ state, and so on. Following this pattern, it is easy to see that biases greater than 1.1 mV have the effect of randomizing the magnetization of the Mn_{12} molecule, making all states equally accessible and effectively bringing the magnetic temperature to infinity. This magnetic randomization via tunneling electrons will have interesting conse-

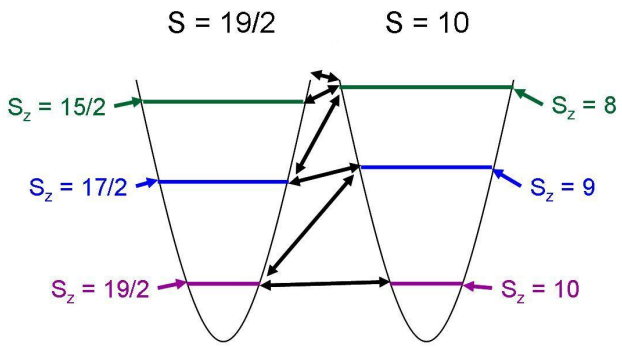


Figure 3.16: Cartoon of magnetic randomization in a Mn_{12} single-molecule transistor at $B = 0$.

quences for the observation of hysteresis in iterative simulations of Mn_{12}-based SMTs, as explained in Subsection 3.3.4.

In addition to zero-field splitting, there are two other magnetic signatures in Mn_{12} tunneling spectra that are not due to hysteresis. The first is a lack of traditional Zeeman splitting of the ground state in Figure 3.15b. This will be discussed in more detail in Section 4.3. The second is related to magnetic anisotropy. Figure 3.17 shows a quasi-steady-state simulation of the tunneling spectrum of a Mn_{12}-based SMT. In this simulation, conductance is plotted as a function of V and B at constant $V_g = -20$ mV, as opposed to the more standard plots of conductance vs. V and V_g at constant field. The slight curvature of the conductance peaks as a function of magnetic field is due to the difference in the anisotropy parameters of the Mn_{12}^{+} Hamiltonian (D_+) and the Mn_{12} Hamiltonian (D_n). If these parameters were equal, the conductance peaks would be linear as a function of field (see Figure 3.18).

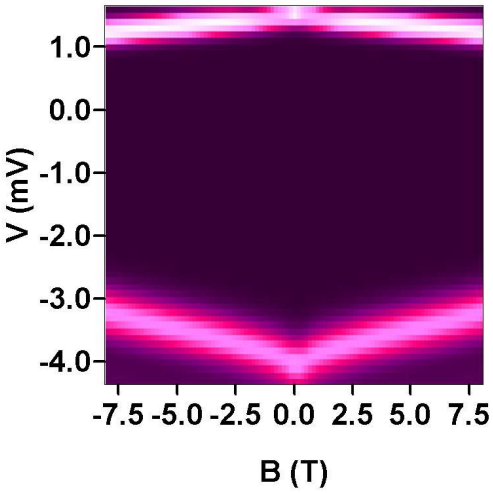


Figure 3.17: Quasi-steady-state simulation of anisotropy in the tunneling spectrum of a Mn_{12}-based SMT. Here the gate voltage is held constant at $V_g = -20$ mV as the magnetic field varies from -8 T to $+8$ T. Same parameters as in Figure 3.15, except $D_n = -0.086$ meV. From [5].

3.3.4 Iterative simulations of hysteresis and magnetic relaxation via tunneling

As explained in Subsection 3.2.3, SMMs exhibit hysteresis at low temperatures. For a Mn_{12} in an SMT, this hysteresis should appear in the conductance spectra as a sudden shift in the peak positions as the magnetization tunnels from the $S_z < 0$ energy well to the $S_z > 0$ as in Figure 3.14.

However, repeated spin transitions caused by tunneling electrons might allow the molecule to surmount the anisotropy barrier between the energy wells on time scales fast compared to the sweep rate of B, so that there would be no abrupt changes measured in the tunneling spectrum as a function of B. For the case of magnetic nanoparticles, Waintal and Brouwer [18] predicted precisely this scenario—under certain conditions tunneling electrons can induce magnetic relaxation despite the presence of anisotropy. More recently, Timm and Elste [19] reached similar conclusions for an SMM.

A steady-state simulation will never reproduce hysteresis in a Mn_{12}-based SMT. This is because hysteresis is by definition a non-equilibrium effect whereby a ferromagnet remains trapped in a state other than its true ground state. In order to allow for the possibility of hysteresis, I instead used an iterative algorithm described below.

1. Calculate a steady state current for the initial point in the parameter space of V and B using the steady state procedure outlined in Subsection 3.3.3.

2. For subsequent points, begin by calculating a new $\mathbf{\Gamma}$ using new parameter values. If the value of B has changed from the previous point, one will need to recalculate the Hamiltonian and shift the basis of the probability vector incoherently from the eigenstates of the old Hamiltonian to the eigenstates of the new Hamiltonian. The shift is incoherent because the algorithm works with probability vectors, not amplitude vectors, so phase information is unavoidably lost.

3. Solve for $\boldsymbol{P} + d\boldsymbol{P}$ using the equation $\boldsymbol{P} + d\boldsymbol{P} = \boldsymbol{P} + (\mathbf{\Gamma} \cdot \boldsymbol{P})dt$, and then make the substitution $\boldsymbol{P} + d\boldsymbol{P} \rightarrow \boldsymbol{P}$.

4. Iterate the previous step a specified number of times (default is 1000). At this time, check to see if each entry in $\boldsymbol{P}$ changes by less than a specified percentage (default is 1%) upon one further iteration. If so, stop iterating; if not, return to step 3. In this fashion, $\boldsymbol{P}$ will reach a quasi-steady-state.

5. Once a quasi-steady-state has been reached, project $\boldsymbol{P}$ against the states corresponding to $S_z < 0$ and see if the majority of the probability density corresponds to a "spin up" or a "spin down" state of the molecule.

6. Once this has been determined, check to see if after one iterates $\boldsymbol{P}$ for a given time corresponding to the time between points in parameter space (inverse of the sweep rates of V or B), that the probability density remains primarily in the same "well." If the density would remain primarily in the original well, go to the next point in parameter space and apply the algorithm from step 2.

7. If the probability of flipping wells is greater than 50%, then $\boldsymbol{P}$ is temporarily replaced by a new $\boldsymbol{P}$ corresponding to 50% probability in the eigenstate of the Mn_{12}^{+} Hamiltonian with the greatest probability density in the ground state of the new well and 50% in the eigenstate of the neutral Mn_{12} Hamiltonian with the greatest probability density in the ground state of the new well.

8. $\boldsymbol{P}$ is then iterated using the same formula ($\boldsymbol{P} + d\boldsymbol{P} = \boldsymbol{P} + (\boldsymbol{\Gamma} \cdot \boldsymbol{P})dt$) each entry in $\boldsymbol{P}$ changes by less than a specified percentage (default is 1%). At this point, check again to see if the majority of the probability density has stayed in the new well. If it has, then keep this new $\boldsymbol{P}$ permanently. But if the majority of the probability migrates back to the original well, discard this new $\boldsymbol{P}$ and use the one found in step 4.

9. Go to the next point in parameter space and apply the algorithm from step 2.

Figure 3.18 shows a simulation based on the algorithm described above where V is swept from a given V_{min} to V_{max} at B_{min}, then B is incremented positively and V is swept at each B value. When the bias window is large enough so that the excited state appears in the tunneling spectrum, as pictured in Figure 3.18a, no hysteresis is observed. On the other hand, if the bias window is small, then hysteresis appears in the conductance peaks, as pictured in Figure 3.18b. Figure 3.18c,d illustrate how

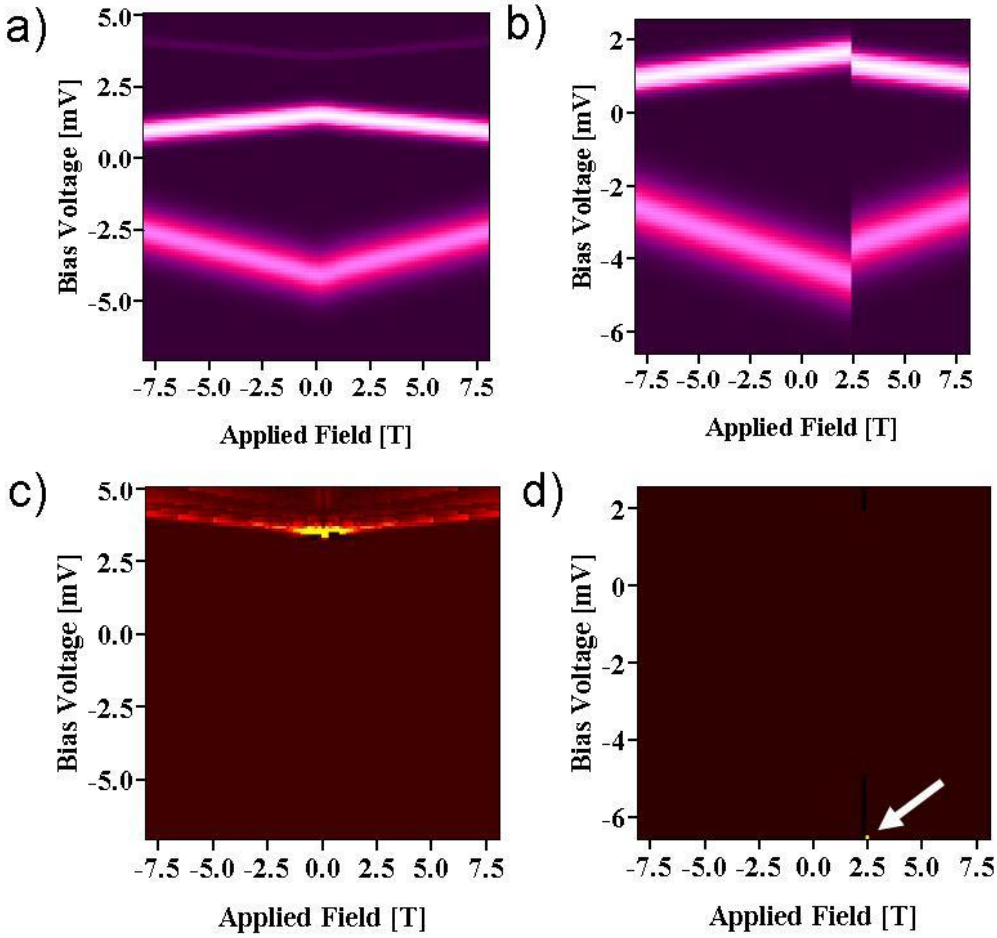


Figure 3.18: Iterative simulations of the tunneling spectra of a Mn_{12}-based SMT at $V_g = -20$ mV. Similar parameters as in Figure 3.15. Field is swept from negative to positive. a) When the excited state is accessible, no hysteresis is present. b) If the bias window is kept small enough, hysteresis is observed. c) and d) "Shift rates" (see text) of a) and b) respectively. Arrow in d) corresponds to the point at which the magnetization tunnels into the ground state.

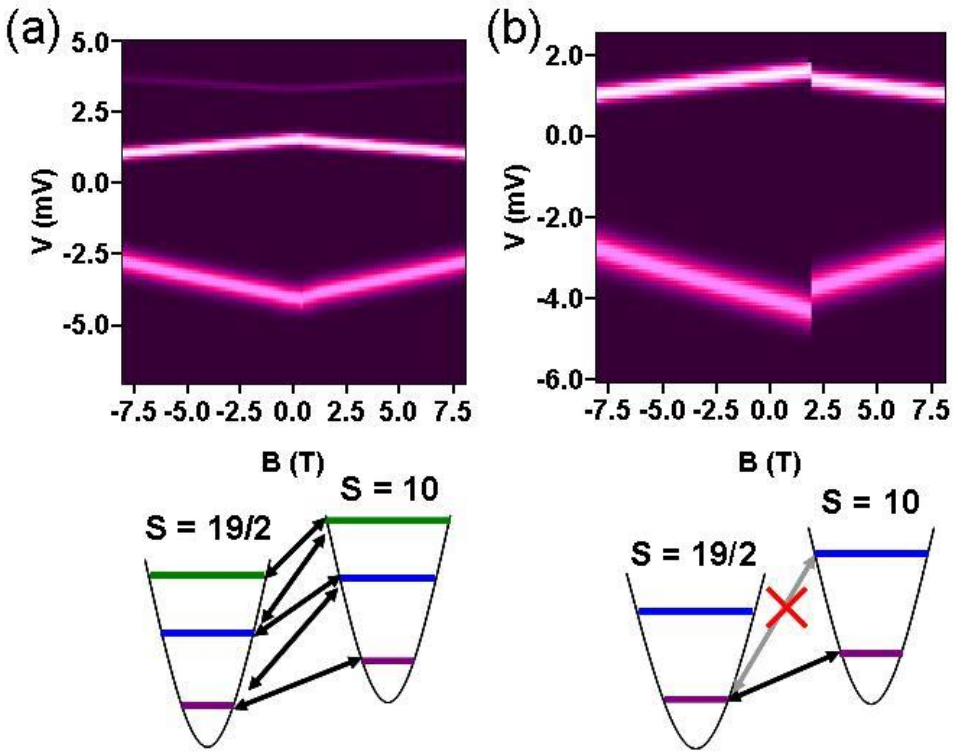


Figure 3.19: Explanation of the disappearance of hysteresis at high biases. Simulations of the tunneling spectra were done using $V_g = -20$ mV and the same parameters as in Figure 3.15. a) At high biases, the tunneling current randomizes the magnetization, erasing the "memory" inherent in hysteresis. b) When the bias is restricted, magnetic randomization does not occur and hysteresis is observed. Adapted from [5].

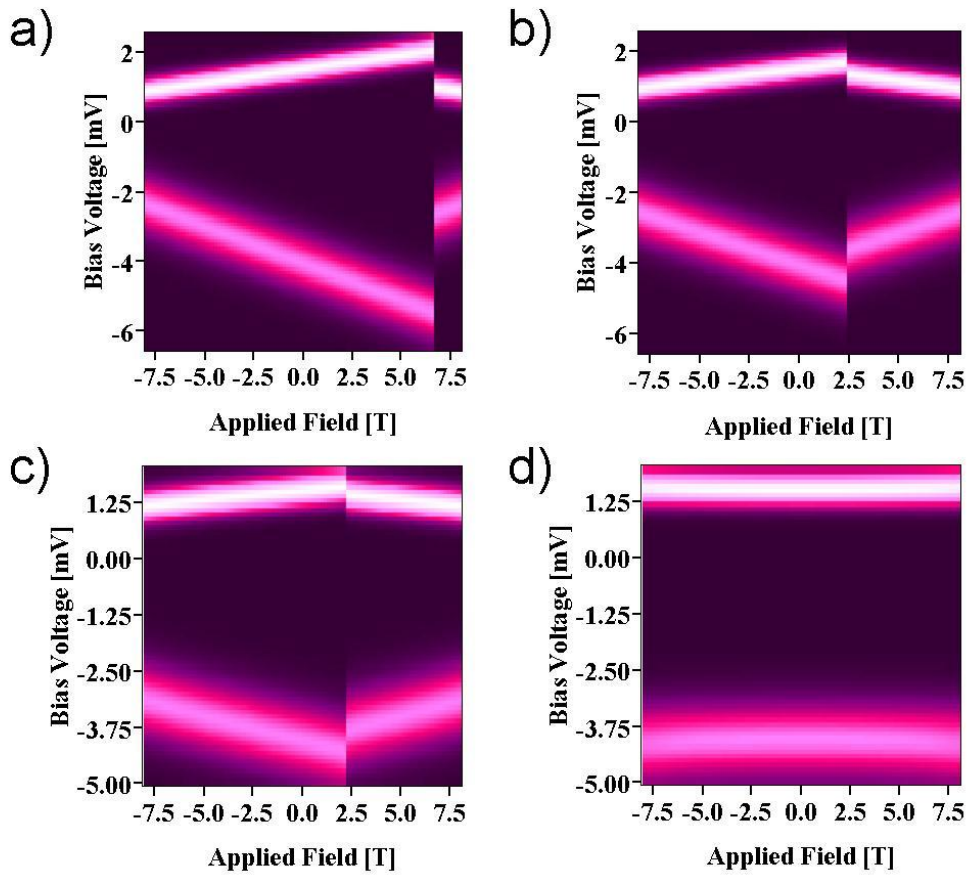


Figure 3.20: Iterative simulations of the tunneling spectra of a Mn_{12}-based SMT ($V_g = -20$ mV) at various angles of the applied field with respect to the easy axis. Similar parameters as in Figure 3.15 except: a) $\theta = 0^o$. b) $\theta = 30^o$. c) $\theta = 60^o$. d) $\theta = 90^o$.

quickly the probability density is shifting from its original well to the opposite well (lighter shades correspond to faster shift rates). From plots a) and c), it is clear that the probability density shifts rapidly at biases greater than those required to observe the excited state transition. In plot d), the only point where the shift rate is fast corresponds to the point in plot b) where the hysteretic transition occurs.

Figure 3.19 illustrates what is happening. In simulations such as those shown in Figure 3.19a, when the bias is sufficient to observe the excited state, the magnetization is randomized as discussed in Subsection 3.3.3. This precludes the observation of hysteresis since the molecule has an opportunity to find the true ground state of the system at high bias voltage at every value of applied field. In contrast, Figure 3.19b shows the case where the bias is insufficient for the magnetization to be randomized, so the magnetization is stuck in the $S_z < 0$ well until the field increases to the point where the magnetization is far enough from equilibrium to force it to tunnel through the barrier into the ground-state well. Figure 3.20 shows the dependence of hysteresis on the angle, θ, between the applied field and the easy axis. As one might expect, the point where the magnetization tunnels occurs at lower field values for higher values of θ until $\theta = 90^{\text{o}}$ where hysteresis is no longer observed in the conductance spectrum.

REFERENCES

[1] M. A. Kastner, Phys. Today **46**, 24 (1993).

[2] L. P. Kouwenhoven *et al.* in L. L. Sohn, L. P. Kouwenhoven and G. Schön (Eds.), *Mesoscopic Electron Transport*, Springer, New York, 1997.

[3] J. Park, *Electron Transport in Single Molecule Transistors*, Ph.D. thesis, University of California, Berkeley, 2003.

[4] A. N. Pasupathy, *Electron Transport in Molecular Transistors*, Ph.D. thesis, Cornell University, 2004.

[5] M.-H. Jo and J. E. Grose *et al.*, Nano Lett. **6**, 2014 (2006).

[6] S. Kubatkin *et al.*, Nature **425**, 698 (2003).

[7] D. Gatteschi and R. Sessoli, Angew. Chem. Int. Ed. **42**, 268 (2003).

[8] I. Tupitsyn and B. Barbara in J. S. Miller and M. Drillon (Eds.), *Magnetism: From Molecules to Materials III, Nanosized Magnetic Materials*, Wiley-VCH, Weinheim, 2002.

[9] R. Sessoli *et al.*, Nature **365**, 141 (1993).

[10] M. A. Novak and R. Sessoli in L. Gunther and B. Barbara (Eds.), *Quantum Tunneling of Magnetization - QTM '94*, Springer, New York, 1995.

[11] C. Paulsen and J.-G. Park in L. Gunther and B. Barbara (Eds.), *Quantum Tunneling of Magnetization - QTM '94*, Springer, New York, 1995.

[12] K. Petukhov, S. Hill, N. E. Chakov, K. A. Abboud and G. Christou, Phys. Rev. B **70**, 054426 (2004).

[13] E. del Barco *et al.*, J. Low Temp. Phys. **140**, 119 (2005).

[14] E. Bonet, M. M. Deshmukh and D. C. Ralph, Phys. Rev. B **65**, 045317 (2002).

[15] M. M. Deshmukh, *Probing Magnetism at the Nanometer Scale using Tunneling Spectroscopy*, Ph.D. thesis, Cornell University, 2002.

[16] S. Braig and P. W. Brouwer, Phys. Rev. B **71**, 195324 (2005).

[17] H. B. Heersche *et al.*, Phys. Rev. Lett. **96**, 206801 (2006).

[18] X. Waintal and P. W. Brouwer, Phys. Rev. Lett. **91**, 247201 (2003).

[19] C. Timm and F. Elste, Phys. Rev. B **73**, 235304 (2006).

Chapter 4

Coulomb blockade in single-molecule transistors based on single-molecule magnet (Mn_{12}) compounds

4.1 Introduction

In this chapter, I will discuss data from SMTs based on Mn_{12} complexes [1]. The main point of these experiments is to explain how strong intramolecular exchange forces and magnetic anisotropy in these molecules may affect the flow of tunneling electrons. I note below that our measurements suggest that the structure of the molecules may not be preserved when the molecules are incorporated into our electrode geometry. Due to this uncertainty about the molecular structure, our most important conclusions are qualitative; we show how to distinguish signals of a molecule with significant magnetic anisotropy from non-magnetic tunneling in low-temperature current-voltage measurements, and we suggest steps which may permit future improvements in similar measurements. We find two signatures of magnetic molecular states and magnetic anisotropy: an absence of energy degeneracy between spin states at zero magnetic field (B) and a nonlinear evolution of energy level positions with B. The magnitude of zero-field splitting between spin states varies from device to device, and we interpret this as evidence for magnetic anisotropy variations upon changes in molecular geometry and environment. We do not observe hysteresis in the electron-tunneling spectrum as a function of swept

magnetic field. In experiments in which we apply biases above those required to access the first excited state, the lack of observed hysteresis is consistent with the predictions made by the simulations presented in Subsection 3.3.4. In experiments at low biases, the absence of hysteresis in the tunneling spectra is more surprising, and I will present two hypotheses which may explain it.

The experiments presented in this chapter were done in close collaboration with Moon-Ho Jo, who at the time was a poctdoc in Hongkun Park's lab at Harvard. Moon-Ho fabricated the devices mentioned in reference [1], but most of the measurements were done here at Cornell by both Moon-Ho and me. In Section 4.6, I will present some unpublished data I took by myself using Mn_{12}-based SMTs made with chips I fabricated as in Section 2.1. I should note that Heersche *et al.* were the first to publish a paper on Mn_{12} SMTs [2], although they reported little about the magnetic-field dependence of the spectra, which was our primary focus.

4.2 Control experiments, deposition and electromigration

As I mentioned above, the data presented in this chapter (except for those presented in Section 4.6) were taken from devices fabricated by Moon-Ho at Harvard. His fabrication was similar to that described in Section 2.1. He first produced gate electrodes by depositing 40 nm of Al and oxidizing in air at room temperature. Then, he used electron-beam lithography and liftoff to pattern Au wires 10 nm thick and 100 nm wide.

At Cornell, we exposed the devices to oxygen plasma using the Harrick Plasma PDC-32G for 30-120 s to remove any organic contaminants (we did not use the PlasmaTherm 72 as described in Section 2.5). Molecules were deposited on the samples by applying dilute ($\sim$100 μM) solutions of two similar Mn_{12} complexes

(Mn_{12}Ac in acetonitrile or Mn_{12}Cl in methylene chloride) for less than 1 minute. We then created molecular-sized gaps in the gold wires using electromigration by sweeping the applied voltage (V) at a rate of approximately 30 mV/s until the wire broke (typically at 0.7-0.8 V). Some samples underwent electromigration at a temperature $T = 1.5$ K in cryogenic vacuum, and others at room temperature, with magnetic properties observed in both cases. Detailed electrical transport measurements were performed at $T = 300$ mK. Magnetic fields were applied parallel to the plane of the substrate (see the inset of Figure 3.4). The angle of the magnetic field with respect to the magnetic anisotropy axis of the molecule is expected to vary from device to device because the adsorption geometry of Mn_{12} cannot be controlled during the deposition process.

In addition to the devices made with molecules, we conducted control experiments by preparing approximately 80 junctions from Moon-Ho's chips using solvent alone. We observed simple linear tunneling I-V characteristics or no measurable current in all but two of the control samples. In those two, we found Coulomb blockade characteristics; however these devices exhibited small charging energies (< 75 meV) as compared to much larger charging energies (> 250 meV) in molecular devices, and could therefore be ascribed to nanoscale metal particles created by the electromigration process. None of the control samples displayed any of the characteristics that we associate below with the existence of magnetic states.

We fabricated more than 70 chips of devices incorporating either Mn_{12}Ac or Mn_{12}Cl molecules, each chip containing more than 40 tunneling junctions, although not every junction on a chip was measured. Approximately 10% of these 70 chips exhibited devices with Coulomb blockade characteristics with a yield of 1-4 devices per chip (the other devices exhibited either characteristics of simple tunnel

junctions or no measurable current whatsoever). In total, 16 junctions exhibiting Coulomb blockade were sufficiently stable over time for thorough investigation.

4.3 Zero-field splitting and possible *in situ* degradation of Mn_{12}

Figure 4.1 shows plots of the differential conductance (dI/dV) of two devices as a function of V and V_g. In these plots we observe crossed diagonal lines intersecting at $V = 0$ that indicate tunneling transitions between the ground energy levels of adjacent charge states. In Figure 4.1a, for a Mn_{12}Ac transistor, two additional peaks in dI/dV (marked with green and yellow arrows) can also be observed, corresponding to excited-state transitions with energies of $\sim$1.1 meV and 1.34 meV. As a function of magnetic field (Figure 4.1b), neither the ground-state transition nor either of the excited-state peaks exhibits simple Zeeman splitting of degenerate spin states, in contrast to measurements in non-magnetic quantum dot systems. The existence of Zeeman splitting can be observed, in that the peak marked by the yellow arrow shifts with B to higher energy relative to the ground state, but these two transitions are not degenerate at $B = 0$. This zero-field splitting is exactly what is predicted by simulations of Mn_{12}-based SMTs (see Subsection 3.3.3, especially Figure 3.15). The peak marked by the green arrow does not shift with B relative to the ground state, indicating that this transition corresponds to an excited level with the same spin as the ground state, most likely due to a vibrational excitation of the molecule. This means that the simulation also correctly predicted that there would be only one magnetic excited state in the tunneling spectrum (again, see Subsection 3.3.3 and Figure 3.15).

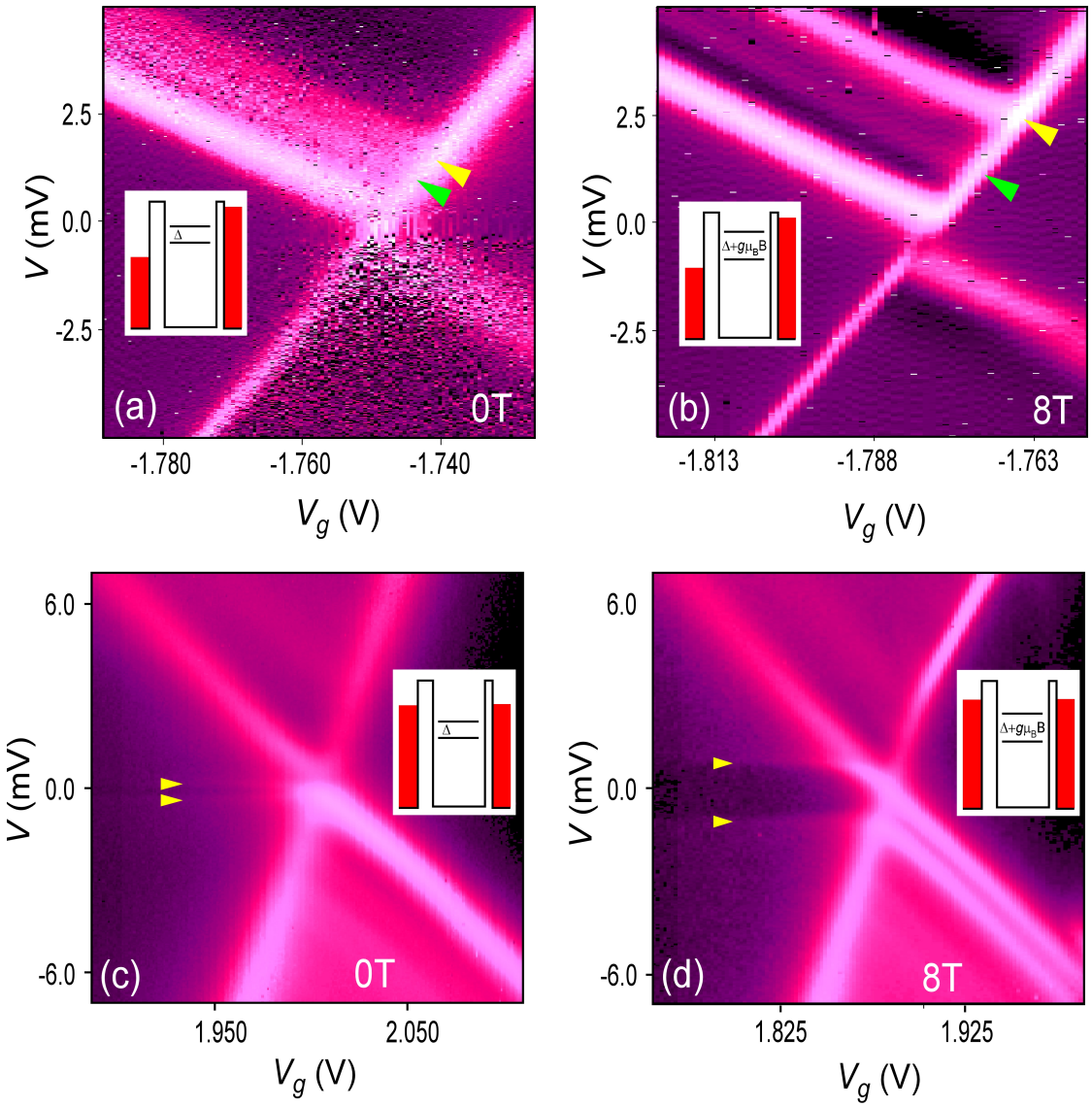


Figure 4.1: Conductance plots of zero-field splitting in Mn_{12}-based SMTs. (a,b) dI/dV vs. V and V_g for a Mn_{12}Ac transistor at $B = 0$ T and 8 T. Arrows (yellow and green) indicate excited energy states. The insets depict energy diagrams for the transport features. (c,d) dI/dV vs. V and V_g for a Mn_{12}Cl transistor at $B = 0$ T and 8 T. The arrows mark cotunneling features. The color scale in all panels varies from deep purple (10 nS) to light pink (200 nS). The color scale in (c,d) is logarithmic. From [1].

Figure 4.1c,d show dI/dV vs. V and V_g plots for a $Mn_{12}Cl$ transistor at $B = 0$ and $B = 8$ T. Here we do not directly resolve separate ground and excited levels at $B = 0$, but instead observe inelastic cotunneling features within the left blockade region [3]. This cotunneling feature indicates the existence of an excited state with a small energy splitting ($\sim$0.25 meV) from the ground state. As B increases (Figure 4.1d), the Zeeman effect increases this splitting and the excited state becomes separately resolvable in the sequential-tunneling spectrum, so we can conclude that the splitting at $B = 0$ is between non-degenerate spin states. In total, we have observed the absence of any degenerate spin states at zero magnetic field in four different devices. We found zero-field splittings between spin states ranging from 0.25 meV to 1.34 meV (both extremes are represented in Figure 4.1).

The absence of spin-degeneracy at $B = 0$ for all states that undergo Zeeman splitting as a function of B is a signature of magnetism in a quantum system. In non-magnetic quantum-dot systems for which the lowest-energy tunneling processes correspond to transitions from an even ($S = 0$) to an odd ($S = 1/2$) number of electrons, it is a requirement of Kramers degeneracy that that the two lowest-energy tunneling transitions ($S_z = +1/2$ and $-1/2$) must exhibit simple Zeeman splitting with no zero-field splitting. To our knowledge, this is observed universally in quantum-dots made from materials with exchange interactions sufficiently weak that magnetic ground states are not possible [4]. For odd-to-even transitions ($S = 1/2$ to $S = 0$) in non-magnetic quantum dots, only one spin transition is allowed for the lowest-energy tunneling transition because of Pauli blocking, so that there is no Zeeman splitting of the first tunneling state, but in this case the lowest-energy tunneling transition must shift to higher energy with increasing B. In all four of the devices that we describe, the energy of the ground-state tran-

sition decreases vs. B, so that this case does not apply. The lack of degenerate spin states at zero magnetic field in four of our devices therefore demonstrates that tunneling in these devices is occurring via magnetic states with non-zero magnetic anisotropy [4]. Therefore, the comparison to the magnetic simulation in Figure 3.15 is a valid one.

In Mn_{12}, the magnetic anisotropy is associated with Jahn-Teller distortions in the octahedral coordination spheres of the eight Mn^{3+} ions, and thus it is sensitive to changes in the charge state and environment of the molecule [5–7]. For example, one Mn_{12} complex has been isolated in two different crystal forms, for which differences in the Jahn-Teller distortion axes around the Mn^{3+} ions give rise to different zero-field splitting parameters of $D = -0.042$ and -0.081 meV [7]. The variations in zero-field splitting observed between devices may therefore be due to variations in the environment of each molecule as it interacts with the surface in the device.

Another possible cause of the variations in zero-field splitting is the fact that the overall molecular structure may not be consistent from device to device. It should be noted that our measurements do not provide a means to verify that the Mn_{12} molecules remain intact through the processes of deposition and electromigration. It is possible that the molecules may lose water ligands, degrade into smaller magnetic subunits or aggregate into larger clusters. However, the qualitative conclusions that we present about tunneling via a magnetic molecule are unaffected regardless of whether our data reflect tunneling through an intact Mn_{12} molecule or through a smaller or larger cluster with non-zero spin and magnetic anisotropy.

The other twelve devices (of sixteen) that we studied in detail also exhib-

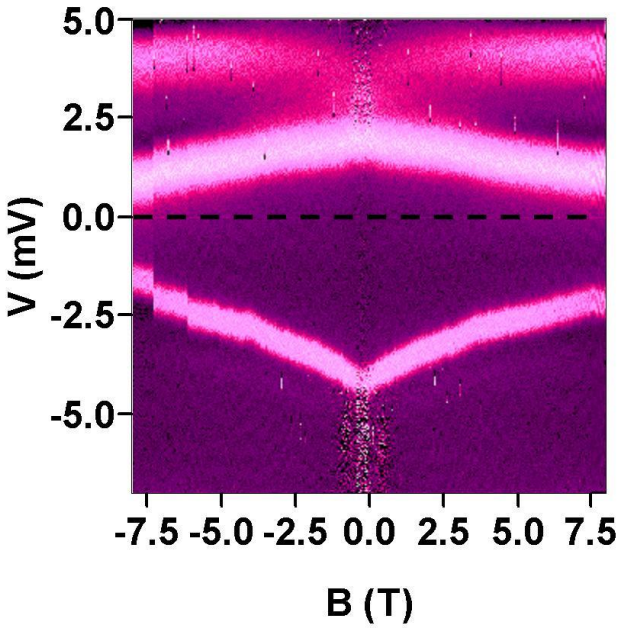


Figure 4.2: Conductance plot of magnetic anisotropy in a Mn_{12}-based SMT. The plot shows dI/dV vs. V and B at fixed V_g for the same Mn_{12}Ac device as in Figure 4.1a,b. The color scale varies from deep purple (10 nS) to light pink (200 nS). Adapted from [1].

ited Zeeman splitting, but with apparent degeneracy at $B = 0$ T. We suggest that molecules in these devices may have degraded to the point of being non-magnetic while remaining redox active. Since Mn_{12} complexes are not air-stable, the molecules may have degraded during the deposition/wire-bonding process when they were exposed to air. Alternatively, since it is known that Mn_{12}Ac can degrade in inert atmospheres at temperatures above 450 K [8], and since break junctions similar to ours are estimated to reach temperatures close to this value during electromigration (see Section 2.4), the electromigration process may have caused the molecules to degrade.

4.4 Anisotropy

Figure 4.2 illustrates the B dependence of the 1.34 meV excitation of the $Mn_{12}Ac$ device from Figure 4.1a,b. Here V_g was held fixed on the more negative side of the degeneracy point and B was swept slowly from -8 T to 8 T while more rapid scans of dI/dV vs. V were measured. The variations of the transition energies are continuous, symmetric around $B = 0$, and show deviations from perfect linearity. The curvature of the conductance peaks in Figure 4.2 is exactly what is predicted by the numerical simulation in Subsection 3.3.3 when the magnetic anisotropy of the N-electron state is smaller than the magnetic anisotropy of the $(N+1)$-electron state (see Figure 3.17).

4.5 No observation of hysteresis

Magnetic measurements of macroscopic Mn_{12} crystals find low-temperature hysteresis for all field directions except those within a few degrees of the hard magnetic axis (see Subsection 3.2.3). As illustrated in Figure 4.2, however, we do not observe hysteresis in any of our devices within a magnetic field sweep range of 8 T, at $T = 300$ mK.

While it is not possible to draw a definitive conclusion about why there is no hysteresis, the most obvious explanation is that the molecule degraded during the processes of deposition and electromigration as described in Section 4.3. If this is indeed the case, then the easiest solution would be to choose a different SMM to study which is both air-stable and stable in inert atmospheres up to at least 450 K. See Section 7.1 for a suggestion of a good candidate molecule for future experiments.

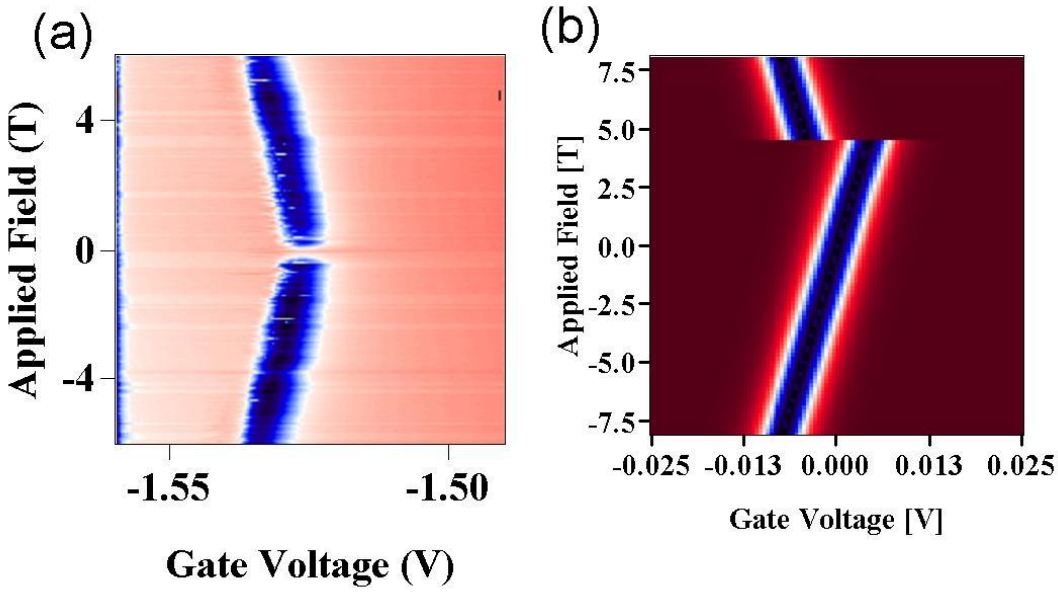


Figure 4.3: Low-bias tunneling current measurements and simulation. (a) I vs. V_g and B at fixed $V = 0^-$ mV. There is no hysteresis, and for unknown reasons the current is suppressed around $B = 0$ T. (b) Simulation similar to those in Subsection 3.3.4 predict that hysteresis should be observed under these conditions.

Another possible explanation that would be relevant to any magnetic molecule is that repeated spin transitions caused by tunneling electrons might allow the molecule to surmount the anisotropy barrier through the sequential occupation of increasingly high-energy spin states. This could allow the magnetic moment to undergo excursions between the $S_z < 0$ and $S_z > 0$ energy wells on time scales fast compared to the sweep rate of B, so that there would be no abrupt changes measured in the tunneling spectrum as a function of B.

From the simulation presented in Subsection 3.3.4, we learned that if, during the magnetic-field sweeps, the voltage is scanned to values sufficiently high to measure the first excited state of the higher-spin state, then there is no hysteresis (see Figure 3.19a). This voltage is sufficiently high to enable tunneling for all allowed tunneling transitions with $S = \pm 1/2$, so that all states in the spin multiplets are

accessible despite the magnetic anisotropy. Within the approximation that only lowest-order sequential tunneling processes are taken into account, the model predicts that hysteretic switching might be observed if V is kept sufficiently low that excited spin states are never populated (see Figure 3.19b). We investigated this experimentally at selected values of V_g by applying a small constant bias V and measuring the tunneling current while sweeping B, but still we observed no hysteresis (see Figure 4.3a), while simulations similar to those in Subsection 3.3.4 predict that hysteresis should be observed (see Figure 4.3b). Possibly this discrepancy is due to spin excitations caused by low levels of experimental noise or by second- and higher-order cotunneling processes that cause spin excitations but which are neglected in the simulation [3].

4.6 Other phenomena

In addition to the data taken using Moon-Ho's devices made with Au electrodes, I took some data which were not published using chips with Pt electrodes I fabricated as in Section 2.1. While I did not observe any hysteretic tunneling spectra, I did see some different magnetic phenomena from what we saw in the Au devices. However, as with the Au samples, most of the spectra I took showed no magnetic characteristics, implying once again that it is likely that many of the Mn_{12} molecules degrade before transport measurements can be taken.

Figure 4.4 shows two devices in which I observed conductance peaks which were split at $B = 0$ T. In contrast to the Au samples, the splitting often decreased with increasing B, a phenomenon I will refer to here as "reverse" zero-field splitting. In Figure 4.4a and b, the negative differential resistance (NDR) trough at positive bias exhibits reverse zero-field splitting, even as the conductance peaks at negative bias

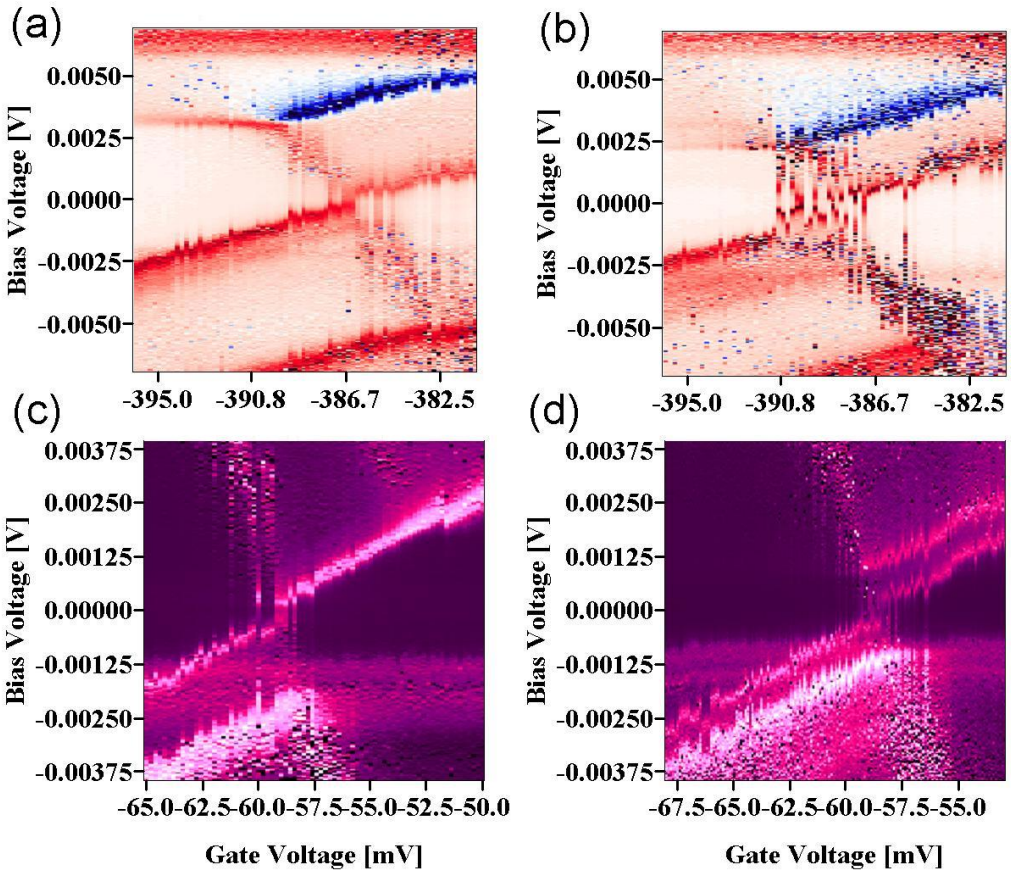


Figure 4.4: Conductance plots showing "reverse" (see text) zero-field splitting in two Mn_{12}-based SMTs. All plots show strong cotunneling peaks. (a,b) dI/dV vs. V and V_g for a Mn_{12}Ac transistor at (a) $B = 0$ T and (b) 8 T. Here the NDR trough at positive bias moves to lower energies as B increases. The color scale varies from deep blue (-4 μS) to deep red (14 μS). (c,d) dI/dV vs. V and V_g for a different Mn_{12}Ac transistor at (c) $B = 0$ T and (d) 8 T. Here the peak at negative bias moves to lower energies as B increases. The color scale varies from deep purple (0 μS) to light pink (10 μS).

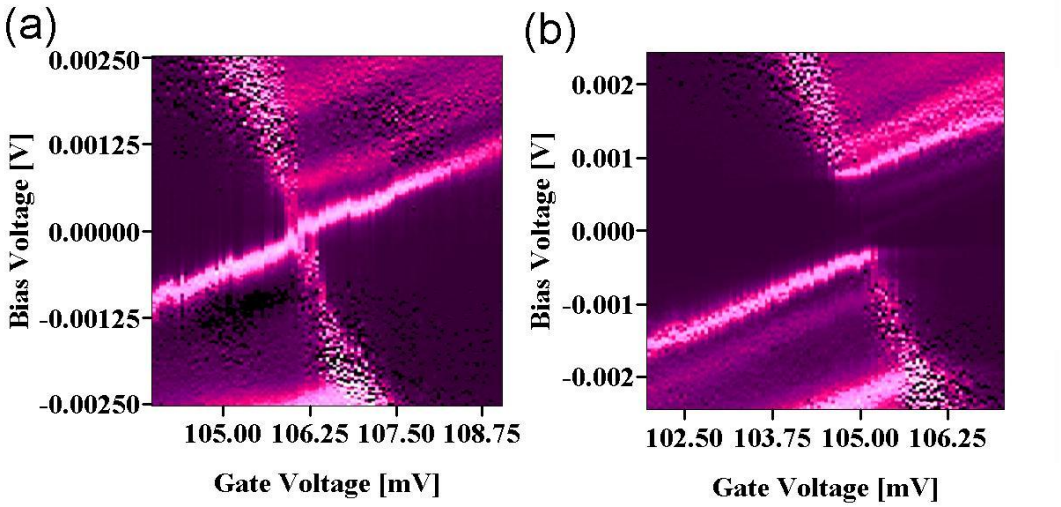


Figure 4.5: High field suppression of low energy conductance peaks in a Mn_{12}-based SMT. The color scale varies from deep purple (0 μS) to light pink (5 μS). (a) $B = 0$ T; no suppression is observed. (b) $B = 8$ T; low energy peaks are suppressed.

exhibit standard zero-field splitting. In Figure 4.4c and d, the peak at negative bias exhibits reverse zero-field splitting while the ground state at positive bias exhibits standard Zeeman splitting.

Reverse zero-field splitting is expected to occur in molecules with magnetic anisotropy when the higher-charge state involved in the transport has a smaller spin than the lower-charge state. For example, if the states involved in the Coulomb blockade are the neutral Mn_{12} state ($S = 10$) and the Mn_{12}^{-} state ($S = 19/2$), then one should expect to see reverse zero-field splitting in the tunneling spectra. However, the presence of the NDR trough in Figure 4.4a and b (usually a sign of spin blockade [2]), as well as the prominent cotunneling peaks in all the Figure 4.4 spectra, imply that the transport in these devices is complex and not easily understood. Certainly, we have insufficient statistics to determine whether the use of Pt electrodes (as opposed to Au electrodes) has any effect on the tunneling spectra of Mn_{12}-based SMTs.

Figure 4.5 shows a sample in which the low energy conductance peaks are suppressed at high field. This is the opposite of what is seen in Figure 4.3a, and I have no good explanation for this phenomenon. Since it only occurred in one device, it may not be representative of Mn_{12}-based SMTs in general.

REFERENCES

[1] M.-H. Jo and J. E. Grose *et al.*, Nano Lett. **6**, 2014 (2006).

[2] H. B. Heersche *et al.*, Phys. Rev. Lett. **96**, 206801 (2006).

[3] S. De Franceschi *et al.*, Phys. Rev. Lett. **86**, 878 (2001).

[4] D. C. Ralph, C. T. Black, and M. Tinkham, Phys. Rev. Lett. **74**, 3241 (1995).

[5] S. M. J. Aubin *et al.*, Inorg. Chem. **38**, 5329 (1999).

[6] M. Soler *et al.*, Chem. Commun. **21**, 2672 (2003).

[7] H. H. Zhao *et al.*, Inorg. Chem. **43**, 1359 (2004).

[8] J. Larionova *et al.*, J. Mat. Chem. **13**, 795 (2003).

Chapter 5

Coulomb blockade in single-molecule transistors based on the high-spin endofullerene, N@C_{60}

5.1 Introduction

Endofullerenes (or endohedral fullerenes) are fullerenes with individual atoms or small groups of atoms encapsulated inside [1]. The notation X@C_{60}, where X is the encapsulated atom(s), is used to name endofullerenes. Roughly half of the elements in the periodic table have been encapsulated in fullerenes at some point, although the rare earth elements are the most commonly encapsulated. Most of these complexes are air-stable up to hundreds of degrees Celsius, with the stability of many higher fullerenes actually increasing upon encapsulation. All endofullerene complexes fall into one of two categories: endohedral metallofullerenes and non-metal doped fullerenes.

Endohedral metallofullerenes are produced either by DC electric arc discharge of metal/graphite composite rods used as positive electrodes, or by the laser furnace method which incorporates laser vaporization of the composite rods under high temperature [1]. While most endofullerenes are produced with low yields (typically with endofullerene:fullerene ratios of less than 1:20), the trimetallic nitride compound $Sc_3N@C_{80}$ is the third most abundant fullerene, surpassed only by C_{60} and C_{70} [2]. Due to the high electron affinities of the fullerenes and the

low ionization potentials of metals, the electronic structure of endohedral metallofullerenes involves a transfer of electrons from the metal atom(s) to the fullerene cage [1]. When this happens in monometallofullerenes, the metal cation takes a position off-center in the fullerene cage.

The most common high-spin endohedral metallofullerene is Gd@C_{82} [3]. In this molecule, three electrons from the Gd atom are transferred to the C_{82} cage, leaving the $4f$-shell of the Gd half filled. By Hund's rules, the Gd^{3+} ion is left in the $S = 7/2$ state, while the C_{82}^{3-} ion is in the low-spin, $S = 1/2$ configuration. Antiferromagnetic coupling between the Gd and the cage leads to an overall molecular spin for Gd@C_{82} of $S = 3$. Gd@C_{82} has been used in many molecular electronics experiments. Gd@C_{82} molecules have been themselves encapsulated in single-walled carbon nanotubes (in a "peapod" geometry) and imaged using both TEM [4] and EELS [5]. Individual Gd@C_{82} molecules were imaged on an Ag(001) surface using STM [6]. In addition to being used in molecular electronics, water-soluble Gd@C_{82} derivatives have been synthesized for medical uses, such as radiotracers and MRI contrast agents [7].

Non-metal doped fullerenes cannot be produced in an arc. Instead, they are usually made by either heating fullerenes in the presence of the non-metal atoms at high pressures or shooting the atoms inside fullerenes using ion- or atomic-beam implantation [2]. Also unlike metallofullerenes, in non-metal fullerenes there is no electron transfer from the encapsulated atom to the fullerene cage (both species remain neutral). While this is unsurprising for noble gas-doped fullerenes, it is certainly surprising that the normally reactive group V elements remain their atomic electron configurations when implanted inside a fullerene.

N@C_{60} is an example of a group V endofullerene [8]. It is produced by ion im-

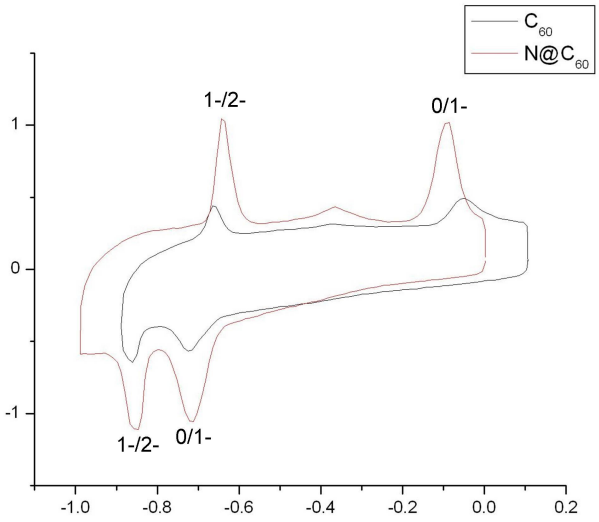


Figure 5.1: Cyclic voltammograms of N@C_{60} and C_{60}. Vertical axis is current in units of 10^{-5} A. Horizontal axis is voltage in volts vs. Ag/AgCl. The molecules were drop cast from toluene onto the working electrode (a 3 mm Pt disc, sealed in glass, polished to a mirror finish). The voltammograms were taken under a nitrogen blanket in 0.1 M tetrabutylammonium hexfluorophospate in acetonitrile, at a sweep rate of 500 mV/s after bubbling the solution with N_2 for 10 minutes. Courtesy Burak Ülgüt.

plantation, but it is extremely hard to purify since $N@C_{60}$:C_{60} ratios are roughly 1:100,000 and since $N@C_{60}$ and C_{60} have such similar masses. $N@C_{60}$ is a high-spin molecule due to the fact that the encapsulated nitrogen atom retains its atomic electronic configuration of $S = 3/2$. Since the electron affinity of nitrogen is roughly 3 eV more negative than that of C_{60}, the additional electrons in $N@C_{60}$ anions are believed to inhabit the LUMO of the C_{60} cage, leaving the nitrogen atom in a neutral state [2]. The coupling of these extra electrons to the nitrogen atom is weak, and cyclic voltammograms we performed on $N@C_{60}$ and C_{60} confirm that the first two reductions of $N@C_{60}$ occur within 25 mV of those of C_{60} (see Figure 5.1). When we decided to make SMTs based on high-spin endofullerenes, we selected $N@C_{60}$ for our experiment because 1) it has a relatively simple magnetic structure, 2) it is stable at the high temperatures achieved during the electromigration process (see Section 2.4) and 3) we could easily compare $N@C_{60}$ transistors to C_{60} transistors for control purposes.

Below, I describe a single-molecule transistor based on the high-spin endofullerene, $N@C_{60}$, in which we observe two uniquely magnetic signatures in the Coulomb blockade tunneling spectra [9]. First, there is a change in the slope of the ground-state conductance peaks when plotted against bias voltage and magnetic field, which we attribute to a change in the ground-state spin of the $N@C_{60}^{2-}$ ion from $S = 3/2$ to $S = 5/2$ as a function of applied magnetic field. Second, excited-state conductance peaks terminate in other excited-state peaks, as opposed to terminating in ground-state peaks as is common in non-magnetic spectra. While changes in spin as a function of field are commonly observed in devices based on GaAs heterostructures [10] and carbon nanotubes [11], the electronic energy-level spacing in small molecules is normally so large as to preclude spin changes at ex-

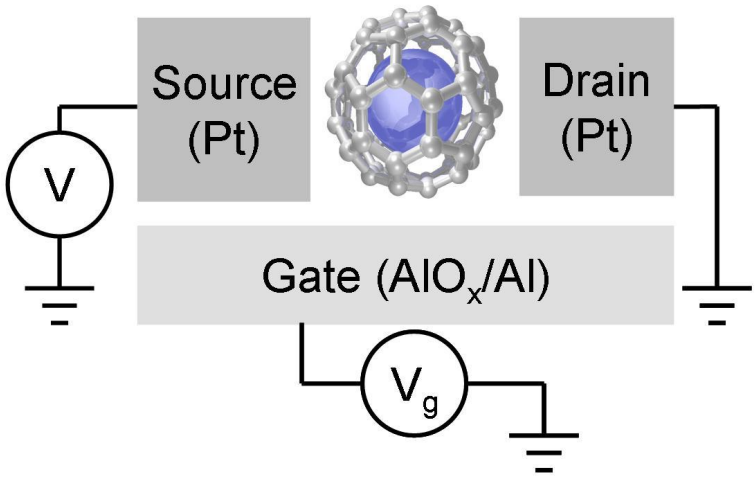


Figure 5.2: Schematic diagram of an N@C_{60} single-molecule transistor. Image of N@C_{60} courtesy Wolfgang Harneit.

perimentally accessible fields. Both magnetic signatures observed in our N@C_{60} devices are made possible by the combination of the high-symmetry of the molecule and the exchange interaction between the electrons on the nitrogen and those on the C_{60} cage. We expect that the ability to exert control over the spin state of a single-molecule device will be of interest, not only to researchers studying molecular electronics, but to scientists in the fields of spintronics [12] and quantum computing [13] as well.

5.2 Negative controls, deposition and electromigration

We prepared the single-molecule transistors, as illustrated in Figure 5.2. We made chips with 10 nm-thick Pt wires as described in Section 2.1. The chips are cleaned with an oxygen plasma as described in Section 2.5 and immediately covered with 25 μL of either a 0.1 mM solution of N@C_{60} for 2.5 minutes or a 0.5 mM solution of C_{60} in toluene for 1 minute. Then the excess solution is blown off the chip, and the deposition process is repeated. This technique produced a convenient

yield of single-molecule devices in the control C_{60} samples. After the molecules are deposited, we cool to cryogenic temperatures and break the wires with 140 Ω of additional series resistance as described in Section 2.6. The success rate for observing Coulomb blockade is 9/19 for N@C_{60} devices and 17/59 for C_{60} devices, while 0/39 devices prepared using pure toluene instead of a fullerene solution show evidence of Coulomb blockade.

5.3 Changes in ground-state spin at high fields

The most striking difference between the N@C_{60} devices and those made from C_{60} can be seen in Figure 5.3, which shows plots of conductance as a function of V and B. In the two N@C_{60} devices pictured in Figure 5.3a,b, the ground-state peaks move apart and then come together as a function of increasing field. At the point where the slopes of the peaks change sign, excited-state peaks take over as new ground-state peaks. We observed the ground-state peaks move apart then together on the positive-gate side of the degeneracy point in four out of five of the N@C_{60} devices on which we performed this measurement, although the field values at which they crossed-over varied from around 1 T to around 7 T. In addition, some excited-state peaks intersect the ground-state peaks without changing their slope. Figure 5.3c shows a similar plot for a C_{60} device also taken on the positive-gate side of the degeneracy point. Here the peaks move linearly as a function of field, and, of the five C_{60} devices measured in this way, none of them show a change in the sign of the conductance peaks' slopes.

The change in sign of the ground-state-peak slopes in the N@C_{60} devices is a clear indication that the difference in spin of the two charge states has changed sign. Labeling the spin of the more-negative gate-voltage state as S_L and the spin

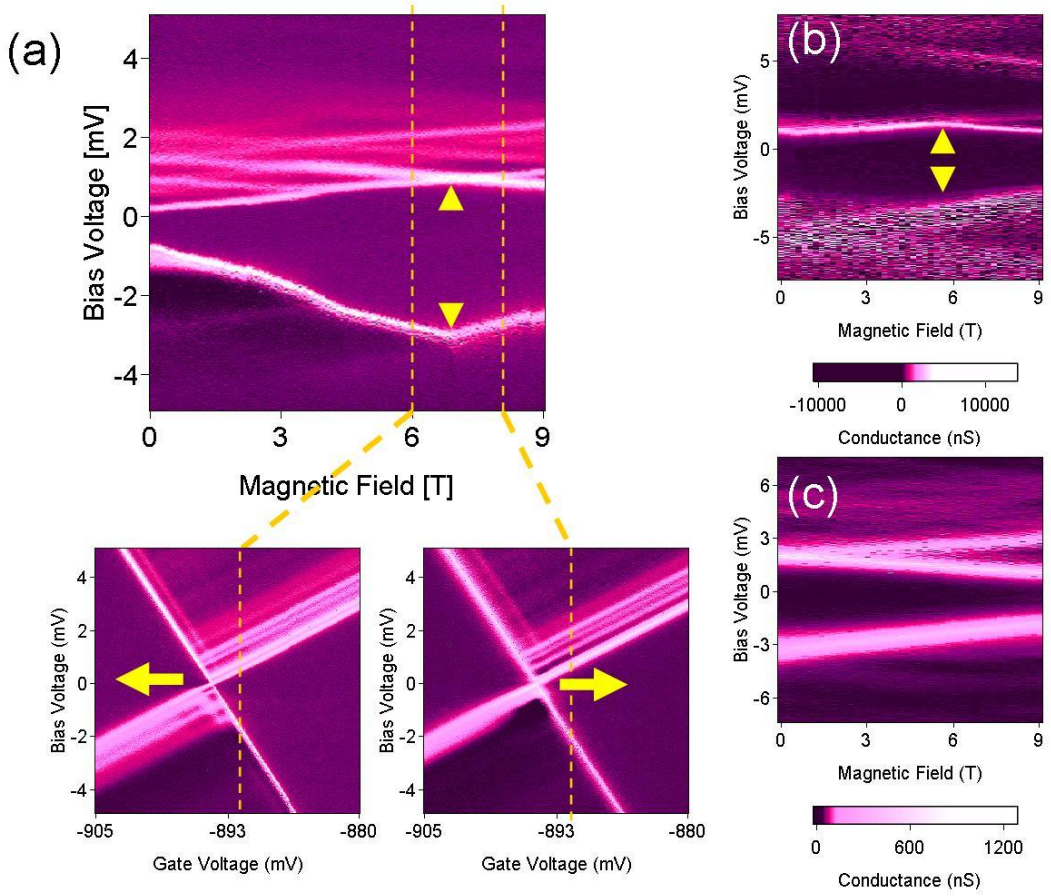


Figure 5.3: Color-scale plots of differential conductance (dI/dV) for N@C_{60} and C_{60} single-molecule transistors at various magnetic fields. (a) Top: Conductance as a function of V and B at constant V_g on the more positive side of the degeneracy point for an N@C_{60} SMT. Color scale varies from -2740 nS (deep purple) to 4730 nS (light pink). Arrows indicate a change in slope of the ground-state peaks. Bottom: Conductance of the same device as a function of V and V_g at $B = 5.5$ T (left) and $B = 8$ T (right). Same color scale as top. The arrows indicate the direction the degeneracy point moves as B increases. (b) Same as (a), top for another N@C_{60} SMT. (c) Conductance as a function of V and B at constant V_g on the more positive side of the degeneracy point for a C_{60} SMT. No change in slope is observed.

of the more-positive gate-voltage state as S_H, the slopes of the peaks imply that at low fields, $S_H - S_L = +1/2$, while at high fields, $S_H - S_L = -1/2$ (assuming $g = 2$). At fields below the change in slope, the degeneracy point moves to more negative gate voltages. This favors the charge state with fewer electrons. Since the degeneracy point by definition is the point at which the two charge states have equal energy, this means that the magnetic field favors the higher-charge state, implying $S_H > S_L$. At fields above the change in slope, the degeneracy point moves to more positive gate voltages, implying $S_L > S_H$.

If we assume that the coupling between the nitrogen spin and the spins on the C_{60} cage is ferromagnetic, then the 2–/3– couple is the couple with the lowest total charge that is capable of transitioning from $S_H - S_L = +1/2$ at low fields to $S_H - S_L = -1/2$ at high fields. Since previous calculations [14] suggest ferromagnetic coupling, as do DFT calculations[1] we performed on the $N@C_{60}^{2-}$ anion, we will assume this to be the case. Our argument in support of assigning the 2–/3– couple to our data is outlined in Figure 5.4a, which shows the nitrogen atom (blue arrow) coupled ferromagnetically to the electrons (black arrows) occupying the three spin-degenerate "LUMO" orbitals of the C_{60} cage. Because the quartet state on the nitrogen lies roughly 600 meV below the doublet state in neutral $N@C_{60}$ [2], the doublet is energetically inaccessible and the blue arrow will always signify a $S = 3/2$ state. The "LUMO" orbitals, which are degenerate when empty, will undergo Jahn-Teller distortions when occupied with one or two electrons.

The $N@C_{60}/N@C_{60}^{-}$ (0/1–) couple can be ruled out since the difference in spin between the monoanion ($S = 2$) and the neutral molecule ($S = 3/2$) is +1/2 at

[1]Evaluation of the relative energies of the different charge and spin states were computed using Gaussian 03 and the B3LYP density functional, using the 6-311+G(d) basis set, after first finding the equilibrium geometry.

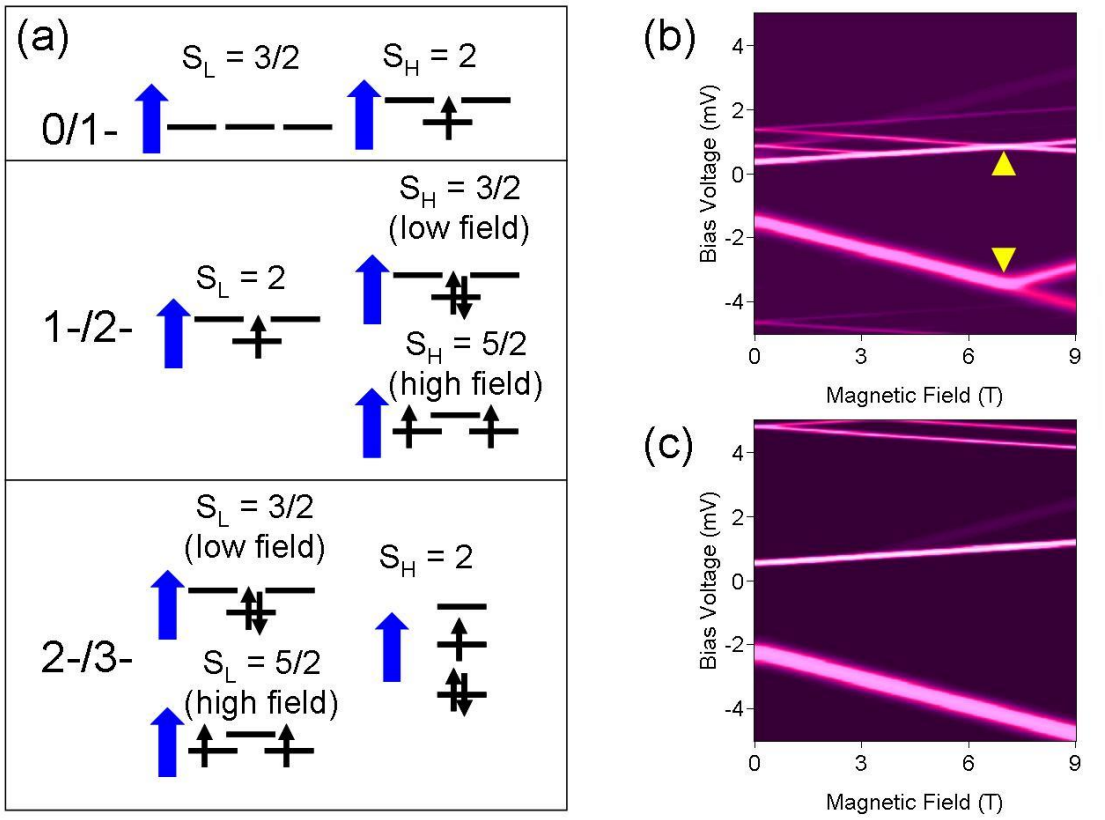


Figure 5.4: Arguments in support of the hypothesis of a 2–/3– transition with ferromagnetic coupling. (a) Cartoons illustrating the various spin states of the N@C_{60} at different charge transitions in a single-molecule transistor. The blue arrow represents the $S = 3/2$ nitrogen atom which couples ferromagnetically to the electrons on the Jahn-Teller distorted C_{60} cage. Of these scenarios, only the 2–/3– transition in is consistent with the data shown in Figure 5.3a,b. (b) Numerical simulation of a 2–/3– transition in an N@C_{60} single-molecule transistor. Color scale same as in Figure 5.3a. Conductance is plotted as a function of V and B at constant V_g on the more positive side of the degeneracy point parameters (see text) chosen to mimic the data presented in Figure 5.3a. Arrows indicate a change in slope of the ground-state peaks. (c) C_{60} device with the same parameters as in (b). Color scale same as in Figure 5.3a. Note that the slopes of the ground-state peaks in the C_{60} simulation do not change sign as a function of magnetic field as they do in the N@C_{60} simulation.

all values of magnetic field. Transitions involving the $N@C_{60}^{2-}$ dianion are more complicated. C_{60}^{2-} is known to have a singlet ground state due to Jahn-Teller distortion of the triply degenerate LUMO [15], which implies that $N@C_{60}^{2-}$ will have an $S = 3/2$ ground state at low fields. In addition, C_{60}^{2-} possesses a relatively low-lying triplet state which some experiments place as close as 0.1 meV above the singlet [15, 16]. This implies that one should expect an $S = 3/2$ ground state for $N@C_{60}^{2-}$ at low fields, and an $S = 5/2$ ground state at high fields, and our DFT calculations on the $N@C_{60}^{2-}$ ion confirm that the energies of the two states are within 20 meV of one another (the limit of the accuracy of the calculation). Therefore the 1–/2– couple implies $S_H - S_L = -1/2$ at low fields and $S_H - S_L = +1/2$ at high fields, opposite to what we observe in the data. However, C_{60}^{3-} has a doublet ground state [15], which implies that $N@C_{60}^{3-}$ has an $S = 2$ ground state. Since the 2–/3– couple leads to $S_H - S_L = +1/2$ at low fields and $S_H - S_L = -1/2$ at high fields, it is the couple with the lowest total charge that is consistent with our data. Using this interpretation for the device used in Figure 5.3a, the fact that the change in slope occurs at $B = 7$ T implies that the splitting between the $S = 3/2$ and $S = 5/2$ states of $N@C_{60}^{2-}$ is 0.8 meV at zero field, consistent with the experiments discussed above which suggest a small singlet-triplet splitting in C_{60}^{2-}. Once again, this argument assumes ferromagnetic coupling between the nitrogen's valence electrons and the electrons on the C_{60} cage. If the calculations are wrong and there is in fact antiferromagnetic coupling, then both a 1–/2– transition and a 2–/3– transition may be consistent with the data.

In order to confirm our interpretation of a 2–/3– couple, Prof. Carsten Timm of the University of Kansas wrote a simulation of conductance in both $N@C_{60}$ and C_{60} single-molecule transistors (see Figure 5.4b,c) as a function of V and

B assuming a 2–/3– transition. The model he implemented assumes that the triply degenerate "LUMO" of the C_{60} cage is split via a Jahn-Teller distortion into one low-energy spin-degenerate orbital with two high-energy spin-degenerate orbitals ("two-above-one"). Since only occupied orbitals can undergo Jahn-Teller distortions, one would expect a "two-above-one"–splitting for the $S = 3/2$ state of the $N@C_{60}^{2-}$ ion, a "one-above-two"–splitting for the $S = 5/2$ state of $N@C_{60}^{2-}$ and a complete loss of degeneracy for $N@C_{60}^{3-}$ ion (see Figure 5.4a). However, we chose to have "two-above-one"–splitting for all states in our model for simplicity. Our choice of "two-above-one" can also be interpreted as a Born-Oppenheimer approximation, since it is likely that the Jahn-Teller distortions of the molecule will be slow compared to the electron tunneling rate.

Once the orbitals are occupied, the electrons on the C_{60} cage interact via 1) Coulomb repulsion with one another, 2) exchange with the electrons on the nitrogen and 3) exchange with other electrons on the cage. Carsten's model (similar to the steady-state model in Section 3.3) is based on the Hamiltonian:

$$\begin{aligned}\mathscr{H} = (E_o - eV_g^{eff})n + V_s^i(n_{e1} + n_{e2}) + V_{sx}n_{e2}(n-2) + \\ \frac{U}{2}(n(n-1)) - J\boldsymbol{s}\cdot\boldsymbol{S} - J_{Hund}\boldsymbol{s}\cdot\boldsymbol{s} - B(s_z + S_z).\end{aligned} \tag{5.1}$$

The terms in (5.1) can be understood as follows. V_g^{eff} is an effective voltage equal to $\alpha V_g - \beta V$ (E_o, V_g and V are defined in Section 3.1). n_{e1} and n_{e2} are the occupation numbers of the high-energy orbitals, and $n = n_a + n_{e1} + n_{e2}$, where n_a is the occupation number of the low-energy orbital. V_s^i is the strength of the Jahn-Teller splitting between the low-energy orbital and the two high-energy orbitals of the i^{th} charge state ($i = 2-, 3-$). V_{sx} is a small parameter corresponding to the slight energy difference between the two high-energy orbitals. $\frac{U}{2}$ represents the strength of the Coulomb repulsion between electrons on the C_{60} cage. $\boldsymbol{s}$ is the

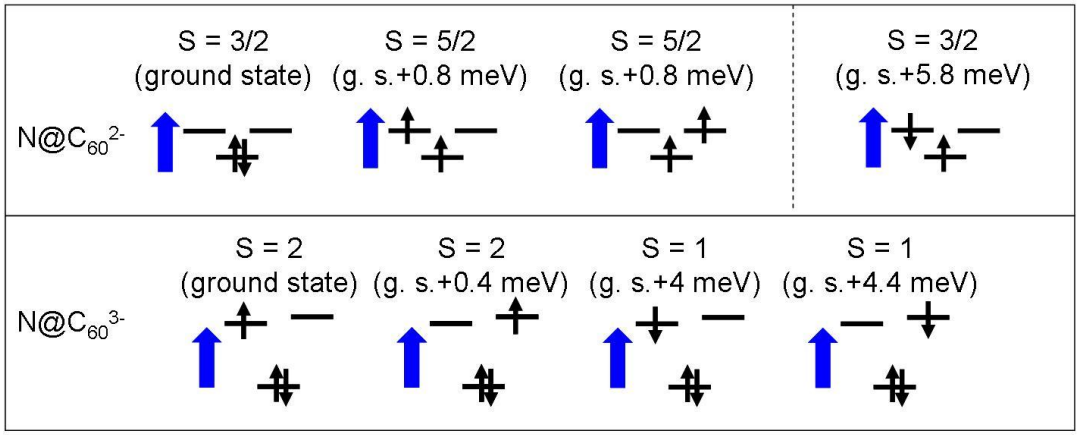


Figure 5.5: Low-energy states in Carsten's model at $B = 0$. The 2– charge state has three low-energy states: an $S = 3/2$ ground state and two degenerate $S = 5/2$ excited states 0.8 meV above the ground state. The next-lowest state ($S = 3/2$) is 5.8 meV above the ground state. The 3– charge state has four low-energy states: two $S = 2$ states separated by 0.4 meV and another two $S = 1$ states 4 meV above the $S = 2$ states. The next-lowest state ($S = 3$) is roughly 40 meV above the ground state.

total spin operator of the electrons in the three orbitals, while $\boldsymbol{S}$ is the nitrogen spin operator. J is the exchange energy between the electrons on the nitrogen and those on the C_{60} cage, while J_{Hund} is the exchange energy among the electrons on the cage.

For the N@C_{60} simulation in Figure 5.4b, Carsten chose the following parameters (in meV except where dimensionless) to roughly correspond to the data presented Figure 5.3a: $E_o = -2177$, $\alpha = 0.15$, $\beta = 0.8$, $V_s^{2-} = 5.8$, $V_s^{3-} = 45$, $V_{sx} = 0.4$, $U = 1000$, $J = 2$ and $J_{Hund} = 1$. Other parameters he used include $T = 230$ mK, and tunneling amplitudes $t_R = 0.59$ meV and $t_L = 0.47$ meV. For the C_{60} simulation in Figure 5.4c, Carsten used the same parameters except he let $J = 0$. The low-energy states for the 2– and 3– charge states are pictured in Figure 5.5.

Clearly, the model reproduces the general features seen in Figure 5.3. The reason that the slopes of the conductance peaks do not change sign in the C_{60} simulation as they do in the N@C_{60} simulation is that the ferromagnetic coupling between the nitrogen and the C_{60} cage in the endofullerene stabilizes the triplet cage state relative to the singlet cage state. This makes the singlet/triplet transition for the electrons on the N@C_{60} cage possible at experimentally accessible fields, while the singlet/triplet transition for the C_{60} molecules will be inaccessible up to $B = 9$ T. In broader terms, the fact that we can observe a change in spin state in N@C_{60} transistors is due to the unique combination of the relative isotropy of the dianion (which keeps the "LUMO" levels relatively close in energy) and the exchange coupling between the electrons on the nitrogen and those on the C_{60} cage (which further reduces the splitting between the $S = 3/2$ and $S = 5/2$ states in N@C_{60}^{2-}).

The details of the plot in Figure 5.4b are very sensitive to the strength of the various parameters in the model, particularly V_s^{2-}, V_s^{3-} and V_{sx}. (The model is not strongly sensitive to J, but J must be sufficiently large or else there is no difference between N@C_{60} and C_{60}.) This helps explain the fact that the change in slope we observe in four of the five N@C_{60} devices we measured occurs anywhere from $B = 1$ T to 9 T (and not at all in the fifth up to $B = 9$ T). The fact that the local electrostatic environment varies greatly from device to device due to the local roughness of the electrodes implies that the N@C_{60} will distort differently in different devices causing variation in the strengths of both the exchange interactions and the Jahn-Teller distortions.

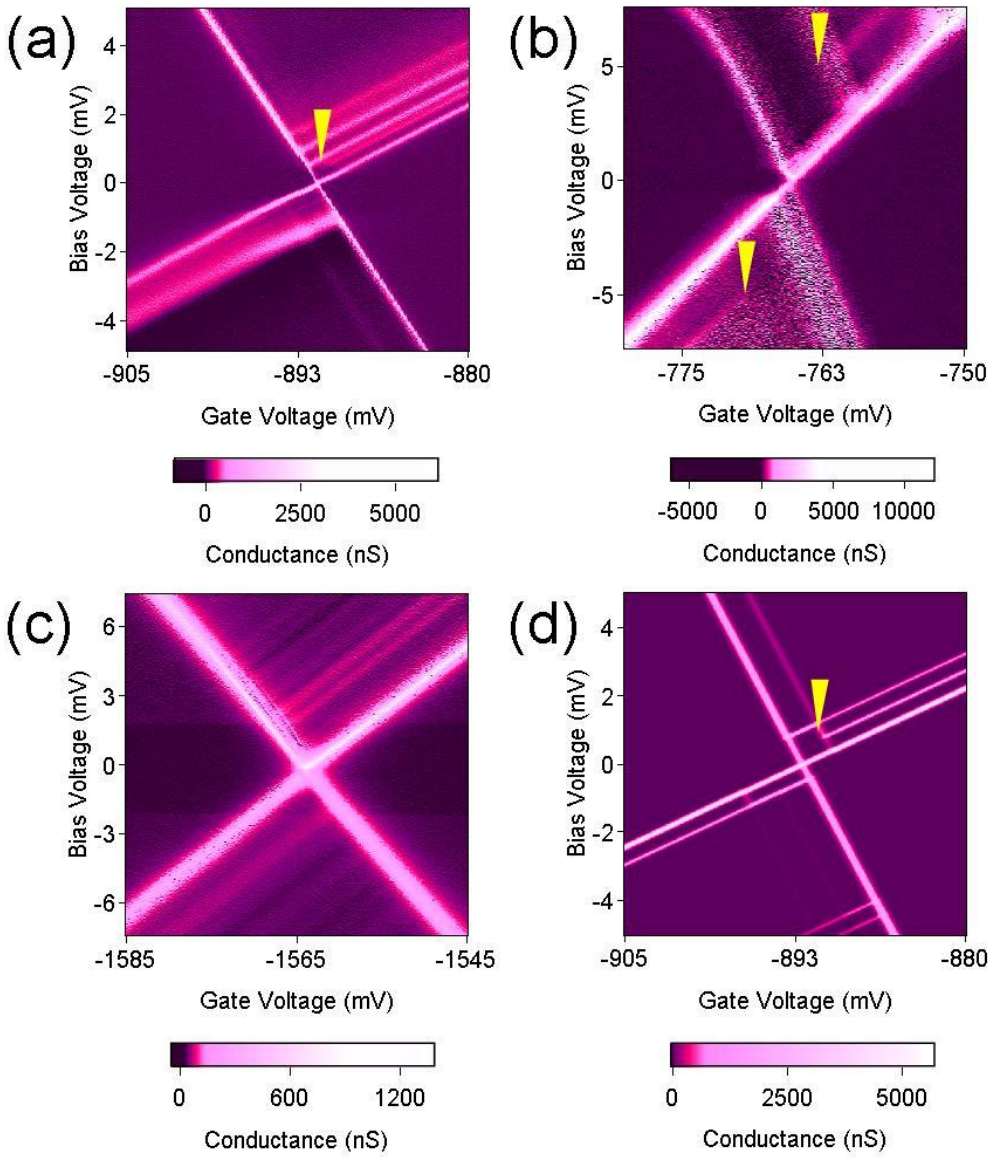


Figure 5.6: Color-scale plots of differential conductance (dI/dV) as a function of the bias voltage (V) and the gate voltage (V_g) at zero applied field ($B = 0$ T). (a),(b) Conductances from the N@C_{60} devices used in Figure 5.3a,b respectively. The arrows indicate ETE peaks (see text). (c) Conductances from the C_{60} device used in Figure 5.3c. No ETE peaks are present. (d) Numerical simulation of the 2–/3– transition using the same parameters as in Figure 5.4b. The ETE peak in the simulation (marked with an arrow) is similar to the ETE peak in the experimental data.

5.4 Signatures of isotropic magnetism at zero-field

Figure 5.6a,b show plots of the differential conductance, dI/dV, as a function of V and V_g from two different N@C_{60} devices at zero field. Only six of the N@C_{60} devices which demonstrated Coulomb blockade were stable for long enough to allow for this kind of measurement. While there are clearly many peaks at low bias corresponding to excited-state tunneling (and at least one trough corresponding to negative differential resistance), the locations and intensities of these peaks (troughs) vary from device to device. Four of the six devices, including the ones used in Figure 5.6a,b, displayed Excited-state conductance peaks which Terminated at other Excited-state conductance peaks (ETE peaks) as opposed to terminating at the ground state peaks as is typical in Coulomb blockade spectra. Of the thirteen C_{60} devices which were stable enough for study, including the one used in Figure 5.6c, none showed this behavior. While all of the N@C_{60} spectra contain excitations with energies below 2 mV, not all of the C_{60} devices exhibit such low-energy excitations.

While it is difficult to determine whether many of the low-energy conductance peaks are due to center-of-mass oscillations, torsional modes or magnetic excitations (intramolecular vibrational modes - including rattling modes of the nitrogen atom - are all expected to be greater than 8 meV [2]), the ETE peaks are characteristic of transport through high spin molecules [17]. ETE peaks arise when certain transitions are energetically possible but cannot occur until other states are occupied with non-zero probability. Results of Carsten's simulation of conductance through an N@C_{60}-based single-molecule transistor shown in Figure 5.6d (same as that in Figure 5.4b except plotted vs. V_g at $B = 0$) confirm the possibility of an ETE peak similar to that found in Figure 5.6a, although there are too

many free parameters to claim a quantitative fit. The presence of additional peaks in the experimental spectrum could be the result of any of three possibilities: 1) the additional peaks are due to non-magnetic excitations (such as center-of-mass oscillations), 2) the parameters chosen in the simulation are not perfectly optimized (the parameter space was too large to do a thorough optimization) or 3) the molecule has been distorted in the junction sufficiently to remove some of the degeneracies assumed in the model.

Elste and Timm [17] predict that characteristic suppressed transitions should lead to reproducible "fingerprints" of ETE peaks in the tunneling spectra that should allow experimentalists to differentiate between the 1–/2– couple and the 2–/3– couple. However, the spectra of the four N@C_{60} devices differed from both the theoretical predictions and from each other to the extent that we were incapable of assigning a specific couple to the data based on ETE peaks. While it is possible in systems with simple Hamiltonians to assign specific spin states to transitions based on the ratios of currents in the Zeeman-split ground state [18], the N@C_{60} Hamiltonian is too complex for this technique to be applicable.

5.5 Other conductance peaks that intersect the ground state

Since in Section 5.3 we were able to suggest that the most likely couple responsible for the N@C_{60} Coulomb blockade is the 2–/3– couple, we used that couple to simulate the conductance peaks in Figure 5.6d. In this model, the ETE peak at positive bias (yellow arrow) is due to transitions involving two distinct $S = 2$ multiplets corresponding to the N@C_{60}^{3-} charge state, as seen in Figure 5.7.

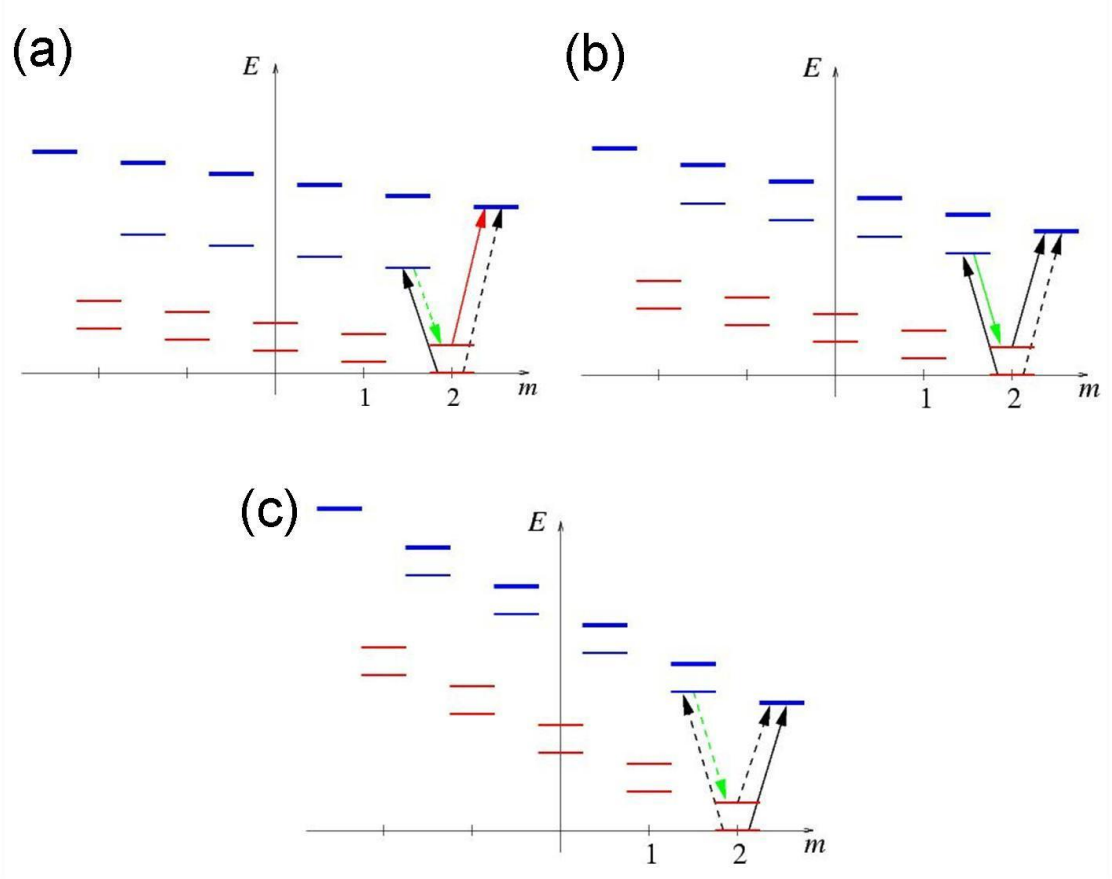


Figure 5.7: Energy diagrams explaining ETE peaks in Carsten's simulation. Red lines correspond to $N@C_{60}^{3-}$ states, blue lines to $N@C_{60}^{2-}$ states. Thick lines indicate orbital degeneracies. To avoid confusion, not all transitions are indicated with arrows, only the minimum necessary to explain the phenomena (see text). (a) 0 T $< B <$ 4 T. (b) 4 T $< B <$ 7 T. (c) $B >$ 7 T. Diagrams courtesy Carsten Timm.

In this figure, red lines correspond to $N@C_{60}^{3-}$ states, blue lines to $N@C_{60}^{2-}$ states. Assume that 0 T $< B <$ 4 T (Figure 5.7a), and that we are in a region of V/V_g parameter space where the transition between the $S_z = 2$ state in the $S = 2$ ground-state multiplet of the 3– charge state and the $S_z = 3/2$ state in the $S = 3/2$ ground-state multiplet of the 2– charge state is allowed (solid black arrow). If, in a given region of parameter space, the transition between the $S_z = 3/2$ state in the $S = 3/2$ ground-state multiplet of the 2– charge state and the $S_z = 2$ state in the $S = 2$ excited-state multiplet of the 3– charge state (dashed green arrow) is not energetically allowed, then the transition between the $S_z = 2$ state in the $S = 2$ excited-state multiplet of the 3– charge state and the $S_z = 5/2$ state in the $S = 5/2$ excited-state multiplet of the 2– charge state (solid red arrow) will not be possible even if it is energetically allowed, because the $S_z = 2$ state in the $S = 2$ excited-state multiplet will have zero occupation. This leads to an ETE peak at low fields. (The dashed black arrow is the transition that leads to a change in slope of the ground state at roughly $B = 7$ T in Figure 5.4b.)

The fact that two electronic configurations with the same total spin are energetically accessible in our experiments is due to the relatively high isotropy of endofullerene anions, even after taking Jahn-Teller distortions into account. Although it is conceivable that ETE peaks would also arise in devices made from strongly anisotropic magnetic molecules, such as single-molecule magnets, due to transitions involving low-lying multiplets with a different total spin than the ground state, no ETE peaks are seen in conductance spectra taken from these devices [19, 20].

In the simulation presented in Figure 5.4b, the ETE peak intersects the ground-state at roughly $B = 4$ T. Once this happens (i.e. for fields satisfying $B > 4$ T as in Figure 5.7b,c), the region of parameter space in which the transition between

the $S_z = 2$ state in the $S = 2$ excited-state multiplet and the $S_z = 5/2$ state in the $S = 5/2$ excited-state multiplet (rightmost solid black arrow in Figure 5.7b) is allowed overlaps with the region of parameter space in which the transition between the $S_z = 2$ state in the $S = 2$ ground-state multiplet and the $S_z = 3/2$ state in the $S = 3/2$ ground-state multiplet (leftmost solid black arrow in Figure 5.7b) is allowed. This occurs because at these fields, it takes less energy to make the transition corresponding to the rightmost black arrow than it does to make the transition corresponding to the leftmost black arrow. So once the $S_z = 2$ state in the $S = 2$ excited-state multiplet is occupied (green arrow), there is no region of parameter space where both the transition corresponding to the leftmost black arrow is energetically allowed and the transition corresponding to the rightmost black arrow is energetically forbidden.

The difference between the region in which 4 T $< B <$ 7 T (Figure 5.7b) and that in which $B >$ 7 T (Figure 5.7c) is that, in the latter region, the transition between the $S_z = 2$ state in the $S = 2$ ground-state multiplet of the 3– charge state and the $S_z = 5/2$ state in the $S = 5/2$ multiplet of the 2– charge state is the ground-state transition. Because $S_H - S_L =$ –1/2 for this transition, while $S_H - S_L = +1/2$ for the ground-state transition below $B = 7$ T, there is a change in slope of the ground state as described in Section 5.3.

Unlike what occurs in the simulation presented in Figure 5.4b, the peak that intersects the ground state at $B = 4$ T in the data in Figure 5.3a does not appear to be an ETE peak. The ETE peak in the data becomes weaker at higher fields, but does seem to intersect the ground state at $B = 1.5$ T without causing a change in slope – the discrepancy between the ETE peak in the data and the simulation most likely implies that the parameters in the simulation are not perfectly optimized

at this time. Since the $B = 4$ T peak does intersect the ground state without changing its slope, it is likely that it is due to a vibrational state of energy 0.5 meV belonging to the ground state of the more-negative gate-voltage state. This hypothesis is supported by the fact that every peak in the spectrum appears to have a vibrational satellite with this energy.

5.6 Summary

In summary, the transport measurements we have made on N@C_{60} single-molecule transistors exhibit magnetic signatures unique to high-spin molecules. While we find device-to-device differences, which appear to be consistent with variations in the degree to which the molecule is distorted from a sphere, nevertheless we can identify the molecular spectra as due to a transition between specific charge and spin states for the approximately isotropic N@C_{60} molecule. The magnetic signatures of the molecule include a low-spin-to-high-spin transition as a function of magnetic field and conductance peaks (ETE peaks) in the molecular spectrum that can be identified with non-equilibrium spin excitations.

REFERENCES

[1] H. Shinohara, Rep. Prog. Phys. **63**, 843 (2000).

[2] T. Akasaka and S. Nagase (Eds.), *Endofullerenes: A New Family of Carbon Clusters*, Kluwer, Dordrecht, 2002.

[3] K. Furukawa, S. Okubo, H. Kato, H. Shinohara and T. Kato, J. Phys. Chem. A **107**, 10933 (2003).

[4] K. Hirahara *et al.*, Phys. Rev. Lett. **85**, 5384 (2000).

[5] K. Suenaga *et al.*, Science **290**, 2280 (2000).

[6] M. Grobis *et al.*, Phys. Rev. Lett. **94**, 136802 (2005).

[7] H. Kato *et al.*, Chem. Phys. Lett. **324**, 255 (2000).

[8] T. Almeida Murphy *et al.*, Phys. Rev. Lett. **77**, 1075 (1996).

[9] J. E. Grose *et al.*, manuscript in preparation.

[10] S. Tarucha, D. G. Austing, T. Honda, R. J. van der Hage and L. P. Kouwenhoven, Phys. Rev. Lett. **77**, 3613 (1996).

[11] P. Jarillo-Herrero *et al.*, Nature **434**, 484 (2005).

[12] A. R. Rocha *et al.*, Nat. Mat. **4**, 335 (2005).

[13] W. Harneit, Phys. Rev. A **65**, 032322 (2002).

[14] L. Udvardi in H. Kuzmany, J. Fink, M. Mehring and S. Roth (Eds.), *Electronic Properties of Novel Materials – Molecular Nanostructures*, AIP, Melville, 2000.

[15] P. Bhyrappa, P. Paul, J. Stinchcombe, P. D. W. Boyd and C. A. Reed, J. Am. Chem. Soc. **115**, 11004 (1993).

[16] P. D. W. Boyd *et al.*, J. Am. Chem. Soc. **117**, 2907 (1995).

[17] F. Elste and C. Timm, Phys. Rev. B **71**, 155403 (2005).

[18] H. Akera, Phys. Rev. B **60**, 10683 (1999).

[19] H. B. Heersche *et al.*, Phys. Rev. Lett. **96**, 206801 (2006).

[20] M.-H. Jo and J. E. Grose *et al.*, Nano Lett. **6**, 2014 (2006).

Chapter 6

Side projects: electrochemical experiments in molecular electronics

In this chapter, I will discuss two projects which fall outside the rubric of single-molecule transistors. Both these projects involve electrochemistry and were done in close collaboration with Burak Ülgüt from the Abruña group. The second project, involving superconducting fullerenes, is still ongoing in the Abruña group.

6.1 Gold nanoparticles mimicking polyaniline transistors

The initial goal of this project, which began in 2003, was to measure "metallic" (temperature-independent) conductance through single strands of the conducting polymer, polyaniline (PANI). The best films of doped conducting polymers at the time were thought to be granular metals, in which small crystalline regions were surrounded by larger amorphous regions [1]. In 2001, N. J. Tao and collaborators made nanoscale acid-gated PANI transistors via electrochemical polymerization of aniline using STM [2, 3]. Our plan was to electropolymerize aniline between nm-spaced electrodes made from break junctions, dope the PANI chemically and measure the intrachain conductance directly at low temperature, thereby avoiding the loss of metallicity associated with interchain hopping. In retrospect, considering the difficulty reasearchers had making reproducible ohmic contact to metallic carbon nanotubes [4], our technique was unlikely to produce metallic conductivity due to contact problems at the PANI-electrode interfaces. However, we ran into

a different problem before we could cool down our sample when we attempted to reproduce Tao's results with acid-gated nanoscale PANI transistors: we observed transistor behavior in our acid-gated gold break junctions without any aniline or PANI present [5]. The physical basis for this surprising observation is discussed in detail in the following two subsections. One year after our work was published, metallic conductivity in a thin-film conducting polymer (PANI-CSA) was observed for the first time [6].

6.1.1 Acid-gated polyaniline transistors

The electrical properties of transistors based on electropolymerized thin films of PANI are nicely illustrated by the results of Wrighton and coworkers [7]. When gold electrodes are coated with a PANI film in acid solution and one sweeps a gate voltage applied to the solution, the conductance of the film initially increases by a factor of 10^6 and then decreases back to a negligible value as the voltage is further increased. The mechanism behind this modulation in conductance relies on the fact that PANI has three distinct structural forms, only one of which is conducting in an acid solution (none of the forms is conducting at neutral pH since the protons from the acid are necessary for doping). As the gate potential is swept, the potential between the solution and the drain electrode forces the PANI film to change from the insulating leucoemeraldine structure to the conducting emeraldine structure and then to the insulating pernigraniline structure.

Our devices are composed of three gold electrodes as shown in Figure 6.1: a macroscopic wire that serves as the gate electrode, and two nanoscale electrodes, supported on a silicon substrate with a thick oxide layer, that serve as the source and drain. The source and drain electrodes were initially fabricated as a continu-

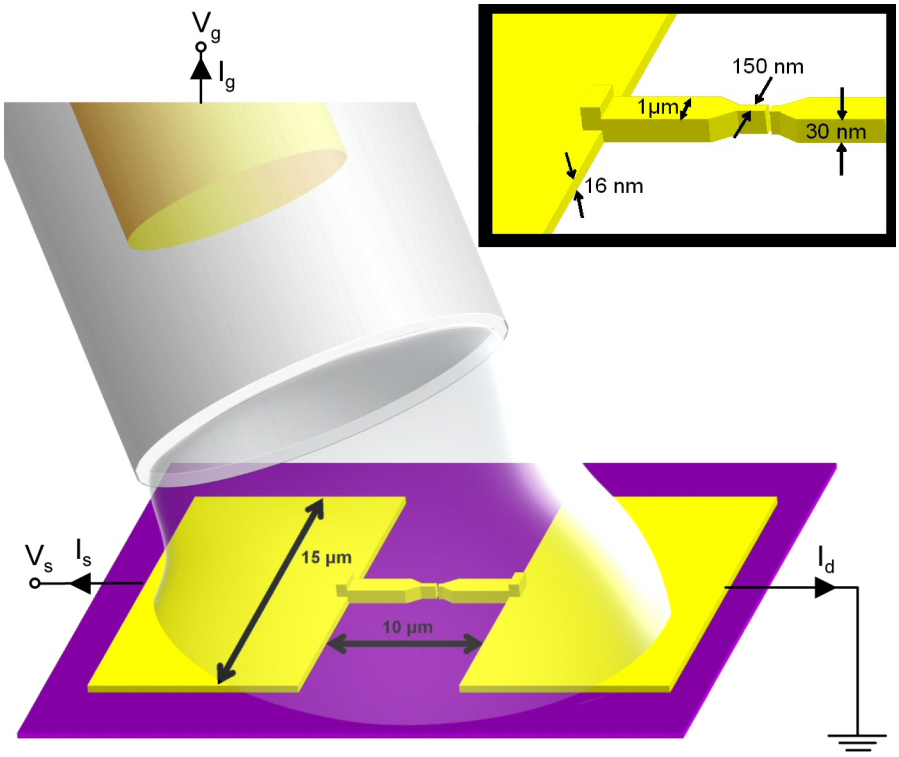


Figure 6.1: Schematic of the device geometry. Dimensions of the smaller features of the lithography are given in the inset. The electrolyte is brought into contact with the junction via a glass pipette tip a few microns in diameter. Voltages are applied to the source and gate electrodes while the drain is attached to ground. Current directions are defined as indicated.

ous wire using a combination of electron-beam lithography and photolithography, and then this wire was broken into separate contacts using electromigration. The resulting gap is a few nanometers wide at room temperature. This gap can be bridged by polyaniline via electropolymerization, although in our paper we focused on the properties of devices with bare gold electrodes. A macroscopic gold wire (gate electrode) was placed in a glass micropipette with a tip diameter of around 10 microns filled with an aqueous solution of 0.5 M $HClO_4$. The pipette was positioned over a silicon chip containing the source and drain electrodes, after the chip was pre-cleaned with an oxygen plasma. As the chip was brought up to the pipette tip, the hydrophilic surface drew the solution from the micropipette over the chip's surface forming a small drop of solution over the electrodes. The drop remained connected at all times to the reservoir of solution in the pipette and thus was in contact with the macroscopic gate electrode which controlled its potential. The drop of acid solution covered not only the thinnest regions of the source and drain electrodes, but also part of the 15-micron-wide contacts (see Figure 6.1).

6.1.2 Transistor behavior via gold nanoparticles

Experimental current-potential curves for bare gold source and drain electrodes in contact with aqueous 0.5 M $HClO_4$ are shown in Figure 6.2a,b. The data were taken during source voltage sweeps from -600 mV to 600 mV at 50 mV/s at constant V_g. As V_g is varied with V_s near 0, we find a peak in the electrical conductance near V_g = -0.8 V (although this value varies somewhat from device to device), with negligible conductances for lower and higher V_g. We observe positive drain current for positive V_s over the region -0.8 V $< V_g <$ -0.4 V and negative drain current for negative V_s over the region -1.4 V $< V_g <$ -0.8 V. Drain current levels are typically

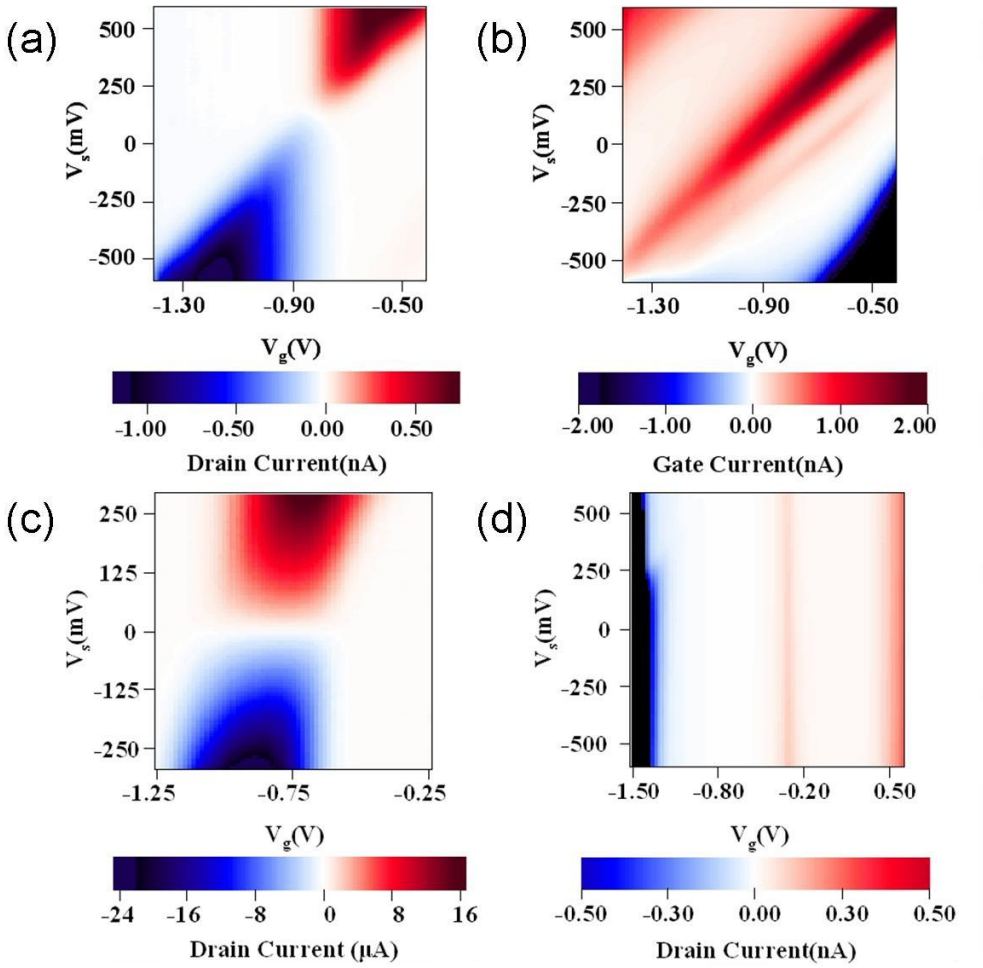


Figure 6.2: (a) Drain current and (b) gate current measured in a device with bare gold electrodes under aqueous 0.5 M $HClO_4$. The diagonal ridge of positive gate current in (b) corresponds to the diagonal threshold for the drain current to turn on in (a). In this region, the gold source electrode undergoes oxidation. (c) Drain current for a device with a 100-nm-thick PANI film grown between the source and drain electrodes, measured under pH 1 sulfuric acid solution. The pattern in which the drain current as a function of gate voltage goes from off to on to off is similar to the device with bare electrodes in (a), although the transition region is wider and the current scale is four orders of magnitude larger. (d) Drain current for a device with bare gold electrodes under a neutral-pH solution of aqueous 0.5 M $NaClO_4$, shown for a larger range of gate voltage than in (a). Note that the transistor characteristics seen in (a) are absent in (d) throughout the entire region of bias extending from oxygen evolution (region on the left) to hydrogen evolution (region on the right).

1 nA at $V_s = 600$ mV, with transconductances of 3 nS. We have observed similar characteristics for over 30 different devices. Since the drop of acid solution bridges the full 10-micron gap between our large photolithographically-defined contacts, it is likely that a significant amount of current flows through the solution over this long distance and not just through the nm-scale gap between the source and drain electrodes.

For purposes of comparison, in Figure 6.2c we plot the current-voltage characteristics for a 100-nm-thick PANI film grown over a nanoscale gap in our electrodes via electropolymerization of the monomer (the same method employed by Wrighton and coworkers [7]). Because the drain current levels are 4 orders of magnitude greater in this PANI device than in devices without the polymer, we can conclude that in Figure 6.2c the current flows through the PANI film. However, the dependence of the current on V_s and V_g is similar in both cases. In particular, the current in the devices without any PANI film present turns from off to on and then off again as a function of gate voltage just like the current in devices with PANI film.

As a first step toward understanding the mechanism of our transistor action, consider the gate current shown in Figure 6.2b for the device without PANI. This plot has three distinct regions of non-zero current, regions which are common to many metal electrodes in aqueous acid electrolytes. The steady-state currents at the corners of the graph are due to H_2 and O_2 evolution at the source electrode. The diagonal ridge in the center of the graph is a transient current due primarily to oxidation and reduction of the source electrode surface. We can be confident of this interpretation, despite the absence of a reference electrode, because these are the only reactions known to take place on gold surfaces in aqueous acid. The

oxidation and reduction of the drain electrode will not induce any measurable current at the gate electrode because the gate current should be proportional to the sweep rate of V_g with respect to V_d, and in our experiment neither the drain nor the gate electrodes are swept, but instead held at constant potentials relative to one another. Since the diagonal ridge in the gate current occurs at the same potentials as the diagonal threshold in the drain current separating the regions of high and low current (Figure 6.2a), it is clear that whatever process is causing the drain current is, in some way, related to the oxidation and reduction of the gold source electrode.

In Figure 6.2d, we have replaced the perchloric acid (0.5 M $HClO_4$) with an aqueous solution of sodium perchlorate ($NaClO_4$) at the same ionic strength (0.5 M concentration) but of essentially neutral pH, and we performed the same measurements as were shown for bare gold electrodes in Figure 6.2a,b. Note that the characteristic transistor behavior of the drain current in acid solution is completely absent in Figure 6.2d, despite the much wider window of gate potential (electrochemical window) displayed, extending from O_2 evolution on the left to H_2 evolution on the right. This demonstrates that neither the perchlorate ion nor the deionized water itself is responsible for the transistor characteristics observed, since these species are present in both the acid and salt solutions.

We claim that the transistor characteristics we observe in devices with bare gold electrodes result from the formation of gold nanoparticles etched from the source and drain electrodes by the acid electrolyte when the source voltage is swept. Without acid to etch the electrodes, no transistor characteristics are observed. Our electrodes are clearly etched during the measurement process, as shown by SEM images (Figure 6.3). In previous STM measurements on Au(111) surfaces

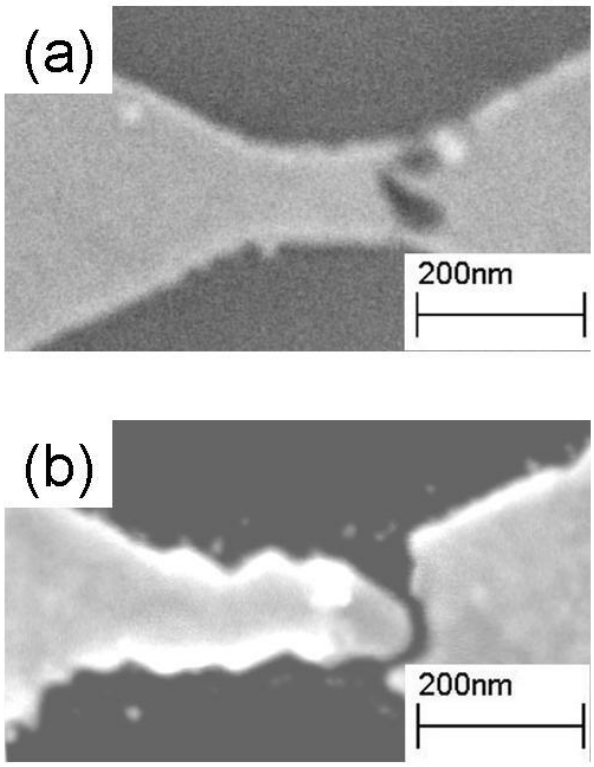


Figure 6.3: SEM images of two gold junctions (a) after being broken in air by electromigration and (b) after being broken in air by electromigration, then placed under aqueous 0.5 M $HClO_4$ at constant V_g in the region of positive current with V_s (left electrode) cycled between -600 mV and 600 mV at 50 mV/s for 10 minutes, and then dried. Note that the gold wire in the second junction has been etched by this process.

undergoing electrochemical cycling in 1 M sulfuric acid, Nieto *et al.* inferred the formation of gold clusters with diameters on the order of a few nanometers [8]. To verify the presence of gold nanoparticles in our samples, we emulated our device setup on a larger scale using macroscopic gold wires, and we applied potentials similar to those used for the nanoscale devices. The resulting acid solution was then placed on a silicon wafer and evaporated. Clusters of gold nanoparticles could be seen using SEM [5]. We confirmed that the nanoparticles were gold using EDX spectroscopy on the same sample.

We suggest that the underlying mechanism by which the current flows in our devices is the same mechanism that underlies scanning electrochemical microscopy (SECM) in feedback mode [9]. The potential of the solution can be tuned using the gate voltage to a value such that a small bias between the source and drain can allow the surfaces of gold nanoparticles to be oxidized at one electrode and reduced at the other, and as a result the nanoparticles will shuttle charge between the electrodes to generate a steady-state current (Dan christened this the "yellow-submarine" model). Current will flow whenever the applied gate voltage causes the redox potential to lie between the source and drain potentials. In standard feedback-mode SECM, one expects to be able to turn a current from off to on by sweeping V_g, but not to turn the current from off to on to off again as in our devices. This is because in most SECM applications there is a uniform solution concentration of electroactive species far away from the source and the drain. This concentration is generally high enough that, reactions at the electrodes do not significantly perturb the bulk concentration.

The unique behavior of our device can stem from the fact that since the gold nanoparticles are etched from the electrodes themselves, the local concentration

of particles between the two leads can be much greater than the concentration in the rest of the solution. This means that if all of the nanoparticles begin in the oxidized state, it is plausible that most could be reduced rather quickly if the potential of the solution were shifted so that reduction occurred on both the source and the drain. This permits the conductance to start near zero when oxidation occurs on both electrodes, rise to some finite value when oxidation occurs on one electrode while reduction occurs on the other, and then drop back to zero when reduction occurs on both electrodes.

To my knowledge, there are four papers which discuss nanoscale measurements of polyaniline using gold electrodes [2, 3, 10, 11]. While the experiments discussed above do not necessarily contradict the results of these papers, they do illustrate the importance of conducting control experiments in which the molecule under study is not present.

6.2 Electrochemical synthesis of fullerene superconductors

Superconductivity was first observed in the fullerenes in 1991 when researchers at Bell Labs found that K_3C_{60} was superconducting with $T_c = 18$ K [12]. Soon afterwards, superconductivity in other alkali-doped fullerenes was observed, with a maximum T_c of 33 K ($RbCs_2C_{60}$) at standard pressure [13]. At the time, this was the highest T_c of any known superconductor outside of the cuprates. On the down side, fullerene superconductors oxidize easily, so they are quite air-sensitive. (Once again, fraudulent reports of gate-induced superconductivity in C_{60} derivatives with T_c as high as 117 K by Jan Hendrik Schön and coworkers should be ignored. See Subsection 1.2.4.)

Today there are many known superconducting C_{60} compounds (for a review,

see [14–16]), and all of them are ionic crystals in which multiply-reduced C_{60} anions alternate with metal cations. Although one might think that any cation could be intercalculated with the C_{60} anions to produce a superconducting crystal, the synthesis of these superconductors places a severe constraint on what cations can be used: the neutral form of the cations must have the reducing power to multiply reduce the C_{60} molecules. This constraint rules out many promising cation candidates. Our idea was to develop an electrochemical synthesis for fullerene superconductors where the electrochemical circuit could provide the reducing power which the cations lack. While the eventual goal was to make new superconducting compounds using different cations, we first sought to make K_3C_{60} or Rb_3C_{60} electrochemically to prove that our synthetic method was viable. While we believe that we were able to make these compounds electrochemically, we were not able to purify them sufficiently to observe a superconducting transition. Work toward that goal will be continuing in the Abruña group after Burak and I graduate.

6.2.1 Theory

C_{60} superconductors can be made using alkali-metal cations, alkaline-earth-metal cations or rare-earth-metal cations [16]. Of these, the alkali-metal-doped C_{60} superconductors were discovered first, have the highest T_c and are the most frequently studied. Therefore, for the rest of this chapter I will limit my discussion to these materials.

The majority of alkali-doped C_{60} superconductors have the formula A_3C_{60}, with three A^+ ions for every C_{60}^{3-} ion. The crystal structure for most of these materials is pictured in Figure 6.4 where the C_{60}^{3-} ions form a fcc lattice with the metal cations filling in the octahedral and tetrahedral interstitial sites. Although almost

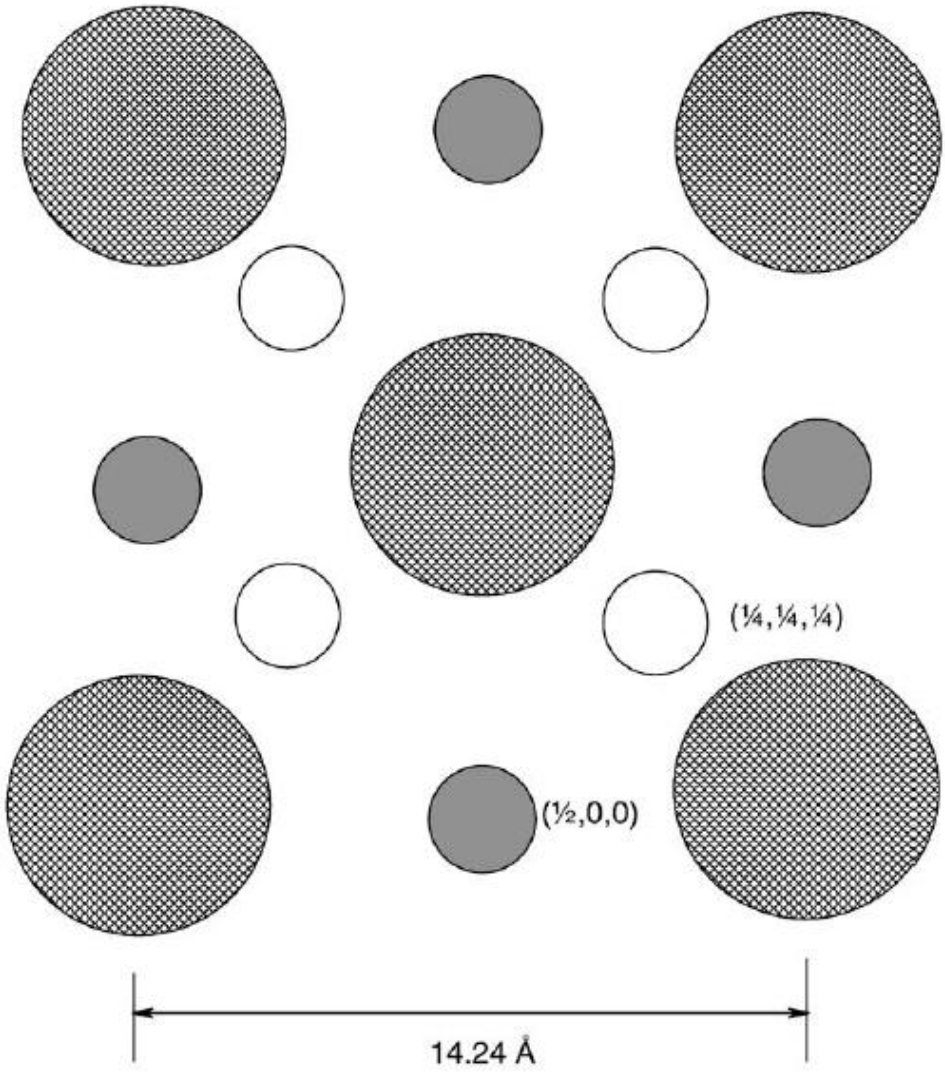


Figure 6.4: Crystal structure of alkali-doped fullerene superconductors. The shaded and open spheres represent alkali ions residing in the octahedral and tetrahedral sites, respectively. From [15].

all superconductors with the formula A_3C_{60} share this structure, the one exception is Cs_3C_{60}. Cs_3C_{60} is only superconducting at high pressure, but its T_c of 40 K is the record for fullerene superconductors.

C_{60} has a triply-degenerate LUMO (see Chapter 5), so one might think that undoped C_{60} and fully doped A_6C_{60} would be insulators while all intermediate dopings A_1C_{60} through A_5C_{60} would be metallic due to their partially-filled conduction bands. However, all intermediate dopings except A_3C_{60} are Mott insulators due to Coulomb repulsion energies on the order of $U \sim 1$ eV in the solid [15]. A_3C_{60} remains metallic at room temperature due to its relatively large bandwidth, $W \sim 0.5$ eV. Normally, if $U/W > 1$ for a given material, it is a Mott-Hubbard insulator, but the triply-degenerate Fermi level of A_3C_{60} leads to an increase in the density of states that shifts the metal-insulator transition to a value of $U/W = 2.5$.

Superconductivity in C_{60} is 3-dimensional and isotropic, unlike the lower-dimensional anisotropic superconductivity of MgB_2 and the organic radical-ion salts. Most scientists believe that the origin of superconductivity in the alkali-doped fullerenes is due to coupling between the between the electrons in the partially-filled t_{1u} band to intramolecular phonons, and thus the superconductivity can be explained using BCS theory [14]. Experiments involving the isotope effect with respect to the alkali dopants confirm that the low energy intermolecular phonons do not contribute to the superconductivity. This justifies our attempts to substitute other ions for the alkali metals: since the metal ions serve only to donate charge to the C_{60}, in theory they can be substituted for other ions of comparable size without destroying the superconductivity.

It should be noted that many BCS approximations which are valid for conventional metals are not applicable to the fullerenes for two reasons. First, for

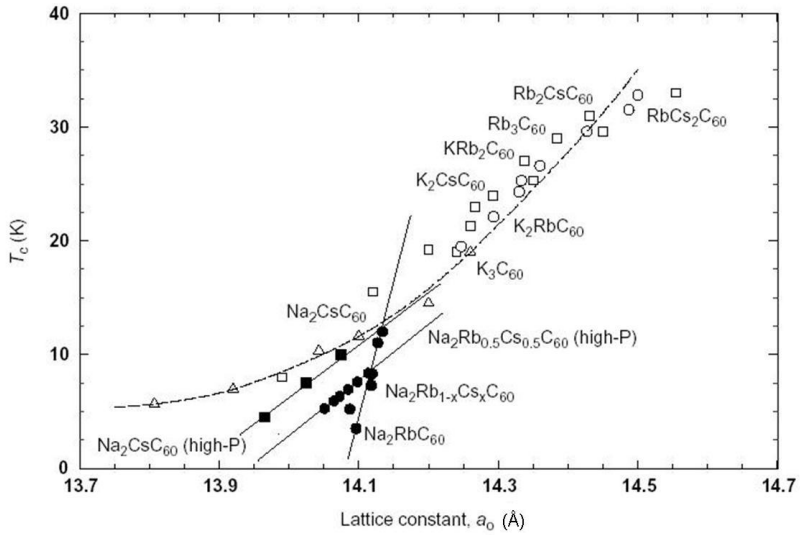


Figure 6.5: Variation of T_c with lattice parameter a_o for alkali-doped fullerenes. The dotted line is the relationship predicted from BCS theory, while straight lines are guides to the eye. From [15].

fullerene superconductors, $N(E_F)V \sim 1$ [14], where $N(E_F)$ is the density of states at the Fermi level and V is the electron-phonon coupling strength, while for classic superconductors $N(E_F)V < 0.3$ [17]. The relatively large value of $N(E_F)V$ for the fullerenes is understandable when one considers that the Fermi level of A_3C_{60} is triply degenerate and that the resonant structure of π-conjugated materials lends itself to strong electron-phonon coupling (see Subsection 1.2.3). Second, the intramolecular phonons have very high energies ($\hbar\omega \sim 0.2$ eV) due to the light mass of carbon and to the stiffness of the C-C bond [14]. Yet, since for BCS superconductors

$$T_c \propto \hbar\omega \exp\left[\frac{-1}{N(E_F)V}\right], \tag{6.1}$$

the same factors that invalidate many common BCS approximations are responsible for the high T_c of the fullerenes compared to classic superconductors.

One possible way to increase T_c in fullerene superconductors by substituting different cations for the alkali metals would be to choose cations which have molec-

ular orbitals close in energy to those of the C_{60}^{3-} ions. This would lead to an increase in the density of states at the Fermi level, which by (6.1) would lead to an increase in T_c. However, one must also make sure that the cation to be substituted is not too large. Figure 6.5 shows the relationship between the distance between C_{60} ions (the lattice parameter, a_o) and T_c for a variety of alkali-doped fullerene superconductors. In this plot, it appears that the larger the lattice spacing between the C_{60} ions, the higher T_c becomes. This makes sense when one considers that a simple tight-binding model implies the farther the C_{60} ions are from one another, the narrower the conduction band becomes, increasing the density of states at the Fermi level. Yet this trend has its limits. Since the largest alkali ion is Cs^+, Figure 6.5 would imply that the alkali-doped fullerene with the highest T_c at ambient pressure should be Cs_3C_{60}. Yet this material is so bloated that the crystal undergoes a transition from fcc to bct, and it no longer superconducts at ambient pressure. Therefore, when choosing a suitable cation for measurements at ambient pressure, one must be sure that if it is bigger than Cs^+ (ionic radius 181 pm [18]), then it must fill in the spaces between the C_{60} ions in such a way that does not distort the lattice.

6.2.2 Experiment

A standard synthesis (informally known as "shake-and-bake") of alkali-doped fullerene superconductors is described in Figure 6.6 [19]. The synthesis is very effective for dopants such as alkali metals that have the reducing power to dope C_{60} to the 3- oxidation state. Figure 6.7 shows that the potential of the C_{60}^{2-}/C_{60}^{3-} couple is roughly -2.2 V vs. Ag/AgCl, which means that any dopant used in the "shake-and-bake" synthesis must have over -2 V of reducing power. As mentioned

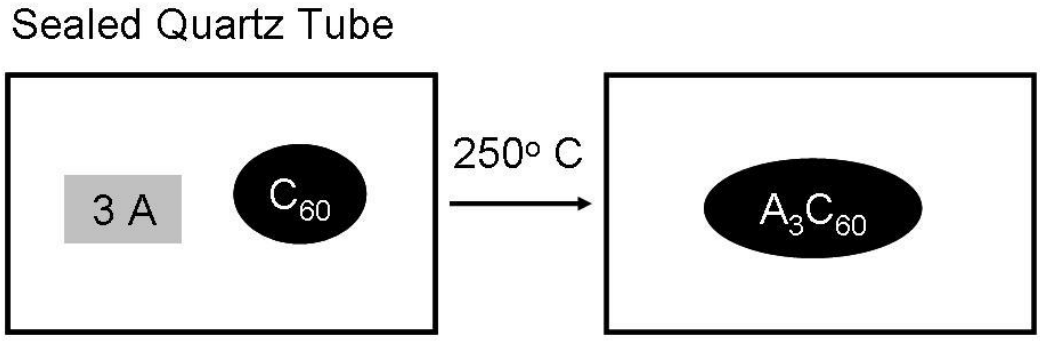


Figure 6.6: "Shake-and-bake" synthesis of alkali-doped fullerene superconductors. A 3:1 molar ratio of an alkali metal (A = K or Rb) and C_{60} is sealed in a quartz tube and heated to 250 C for 24 hours. Then the powder is mixed and heated again to 250 C for another 24 hours. The cycle of mixing and heating is repeated until the desired purity is reached. Procedure follows [19].

above, this places severe limits as to what dopants one can choose using this synthetic method.

In the electrochemical synthesis we attempted, the external circuit provides the reducing potential (see Figure 6.8), so any monocation can be used as a dopant provided that it is stable at the strongly reductive potentials applied in the electrochemical cell. The first electrochemical synthesis of a doped C_{60}^{3-} film was done by Kadish and coworkers [20], but they did not make any measurements of superconductivity. The synthesis described below is only the latest one of many similar syntheses we attempted, all of which were done in a glove box in an inert atmosphere.

1. Get your local glass-blower to make a cell with two chambers separated by a porous frit to allow ion exchange (see Figure 6.8).

2. Put two wires in the larger chamber: a platinum wire to function as a working electrode and a silver wire to function as a reference electrode. In the smaller

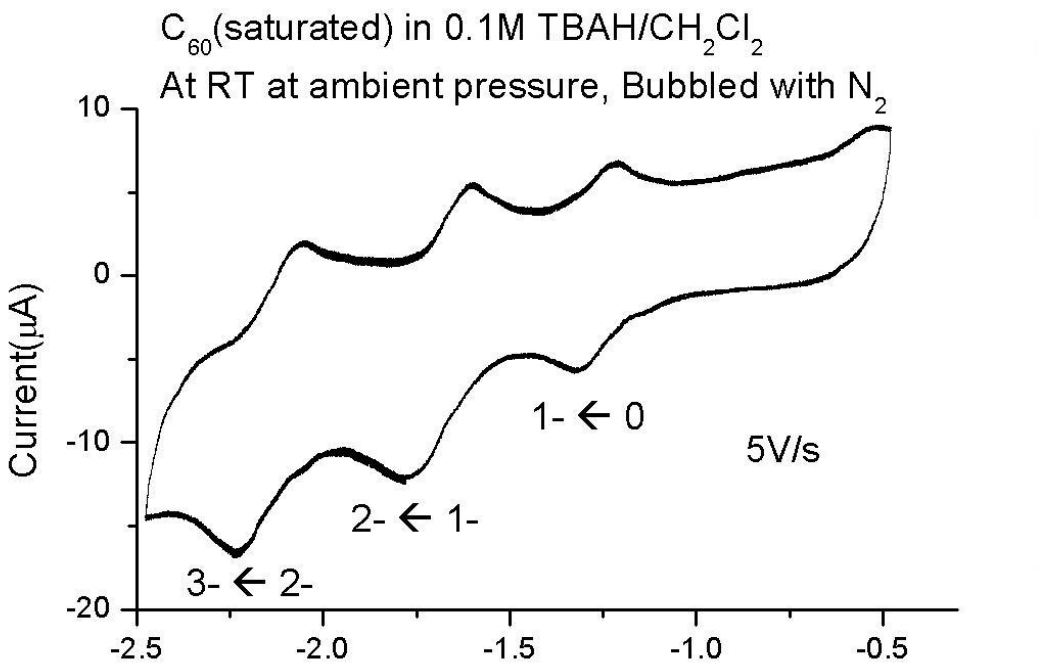


Figure 6.7: Cyclic voltammogram of C_{60} in dichloromethane. Courtesy Burak Ülgüt.

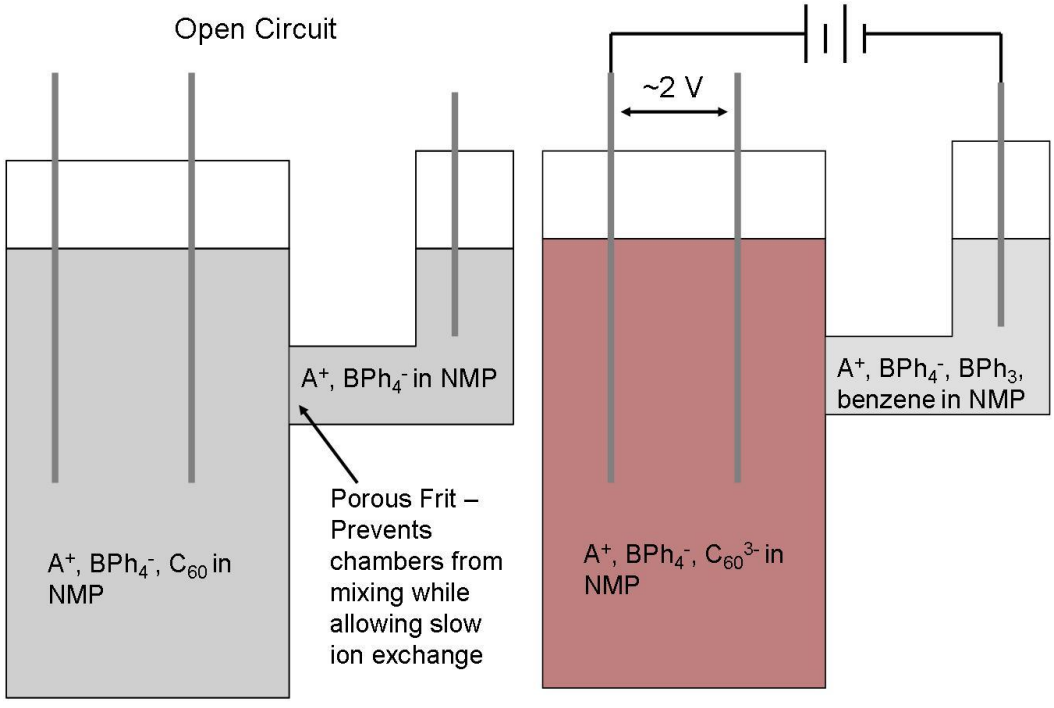


Figure 6.8: Proposed electrochemical synthesis of A_3C_{60} (A = K or Rb). See text.

chamber, put a larger platinum wire to act as a counter electrode.

3. Fill the larger chamber with NMP (a solvent with an electrochemical window larger than -2.5 V on the reductive side, and one in which both C_{60} and Rb_3C_{60} are soluble). Add $RbBPh_4$ (or a different soluble alkali salt) and C_{60} in excess of a 3:1 $RbBPh_4$:C_{60} molar ratio. Fill the smaller chamber with the same solution except leave out the C_{60}.

4. Hook up the electrodes to a potentiostat and apply a reductive potential around 100 mV in from the edge of the solvent window (around -2.4 V). Let it sit about a week until the current diminishes to roughly 1/4 of its starting value. After this time, most of the fullerene in the larger chamber should be triply reduced, and some of the BPh_4^- in the smaller chamber should be oxidized forming BPh_3 and benzene. The solution in the larger chamber should be red/brown.

5. Disconnect the electrodes from the potentiostat, pipette out the solution from the main chamber into a flask, seal the flask, remove it from the glove box and distill it under vacuum in a hot oil bath at 130 C. The powder which remains in the flask should be a mixture of Rb_3C_{60}, $RbBPh_4$ and a small amount of partially reduced fullerene species.

6. Back in the glove box, add dichloromethane to the flask, stir and let settle. Then pipette the solution into a new flask and discard the remaining insoluble fraction. Since Rb_3C_{60} is soluble in dichloromethane, while $RbBPh_4$ is not, this will have the result of purifying the Rb_3C_{60}. Seal the new flask, remove it from the glove box and and rotovap the dichloromethane solution.

7. Back in the glove box, scrape the remaining powder from the bottom of the flask and anneal at 250 C for 1 hour. Stir the powder and anneal again as necessary.

We made low-temperature (5 - 40 K) measurements (using the Quantum Design SQUID magnetometer in the van Dover lab) of the magnetic moment of both "shake-and-bake" and electrochemically-grown A_3C_{60} samples (A = K, Rb) sealed in NMR tubes in a helium atmosphere ("shake-and-bake" samples courtesy Chandrani Roychowdhury of the DiSalvo group). While the "shake-and-bake" samples showed clear superconducting transitions (magnetic moments went from slightly positive at room temperature to between -0.002 and -0.003 emu at 5 K), the temperature dependence of magnetic moments of the electrochemcally grown samples looked no different than those of the control samples (NMR tubes filled with C_{60} and $RbBPh_4$).

Since we did not observe superconductivity in any of our electrochemcially-grown samples, there is the question of whether our electrochemical synthesis produced any A_3C_{60} at all. To answer this question, we first tried X-ray diffraction, but found that the only diffraction peaks which we observed were due to the alkali salt added at the beginning of the synthesis. The lack of C_{60} diffraction peaks is likely due to the fact that carbon has a small nucleus and therefore a small X-ray cross section. To do diffraction on C_{60} effectively, one must use the Cornell High Energy Synchrotron Source, which we did not attempt to do.

We then turned to UV/vis spectroscopy [21, 22]. Figure 6.9 shows absorbance spectra of both "shake-and-bake" and electrochemically-grown samples of Rb_3C_{60} and K_3C_{60}. Although the peaks in the electrochemically-grown samples are smaller, the peak positions of the electrochemically-grown samples are very close to those

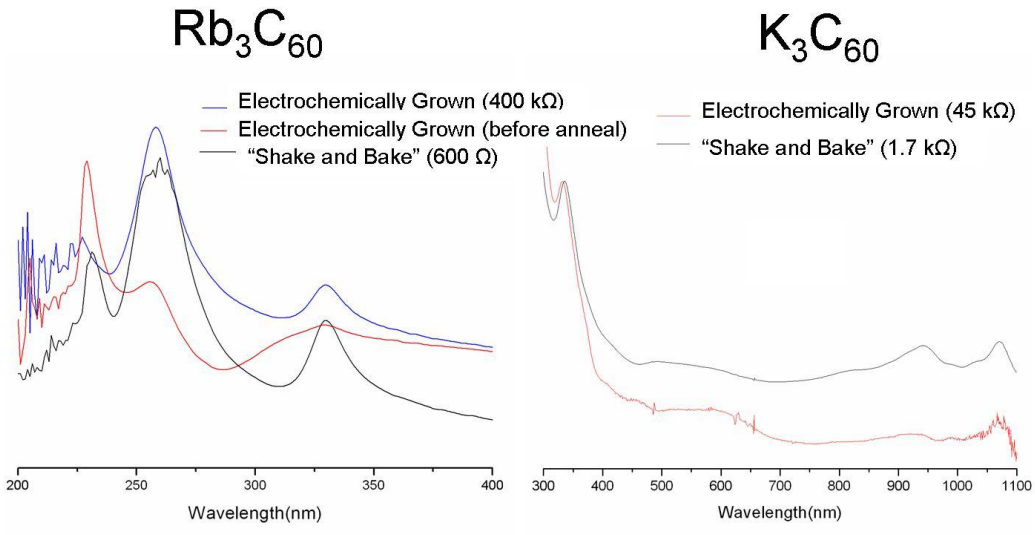


Figure 6.9: UV-vis absorbance spectra of Rb_3C_{60} (left) and K_3C_{60} (right). The electrochemcially-grown K_3C_{60} sample was annealed before the spectrum was taken. Note the similarities between the spectra from samples made using the "shake-and-bake" method and the spectra from samples made using our electrochemical method.

of the "shake-and-bake" samples. We therefore conclude that we were successful in synthesizing Rb_3C_{60} and K_3C_{60}, but not in purifying our samples.

With the help of John Read from the Buhrman group, we also performed XPS on our samples. This confirmed that there were no platinum impurities in the electrochemcially-grown samples using the synthesis described above, but we were unable to determine the precise nature of the impurities by this method. From the X-ray diffraction data, we know that in at least one of our syntheses we were unable to remove the excess salt from our sample. Excess salt is almost certainly the source of some of the impurities. Another source may be degradation products which form as a result of the electrochemistry itself, as a result of either the C_{60} or the solvent breaking down [23]. Finally, there may be unreduced or partially reduced fullerene species (e.g. C_{60}, C_{60}^{-} or C_{60}^{2-}) present.

Future work by members of the Abruña group will hopefully lead to the elec-

trochemical synthesis of pure A_3C_{60}, as well the synthesis of new superconducting fullerene compounds with different cations substituted for the alkali metals. I suggest a good cation to start with may be $N(CH_3)_4^+$, since it is commercially available, relatively small and stable at highly reductive potentials.

REFERENCES

[1] V. N. Prigodin and A. J. Epstein, Synth. Met. **125**, 43 (2002).

[2] H. X. He *et al.*, J. Am. Chem. Soc. **123**, 7730 (2001).

[3] H. X. He, C. Z. Li and N. J. Tao, Appl. Phys. Lett. **78**, 811 (2001).

[4] D. Mann, A. Javey, J. Kong, Q. Wang and H. Dai, Nano Lett. **3**, 1541 (2003).

[5] J. E. Grose, B. Ulgut, A. N. Pasupathy, H. D. Abruña and D. C. Ralph, Phys. Rev. B **71**, 035306 (2005).

[6] K. Lee *et al.*, Nature **441**, 65 (2006).

[7] E. W. Paul, A. J. Ricco and M. S. Wrighton, J. Phys. Chem. **89**, 1441 (1985).

[8] F. J. R. Nieto *et al.*, J. Phys. Chem. B **107**, 11452 (2003).

[9] A. J. Bard and L. R. Faulkner, *Electrochemical Methods: Fundamentals and Applications, 2nd ed.*, Wiley, New York, 2001.

[10] H. X. He *et al.*, Phys. Rev. B **68**, 045302 (2003).

[11] F. Chen *et al.*, Nano Lett. **5**, 503 (2005).

[12] A. F. Hebard *et al.*, Nature **350**, 600 (1991).

[13] K. Tanigaki *et al.*, Nature **352**, 222 (1991).

[14] O. Gunnarsson, Rev. Mod. Phys. **69**, 575 (1997).

[15] S. Margadonna and K. Prassides, J. Solid State Chem. **168**, 639 (2002).

[16] Y. Iwasa and T. Takenobu, J. Phys. Cond. Mat. **15**, R495 (2003).

[17] M. Tinkham, *Introduction to Superconductivity, 2nd ed.*, McGraw-Hill, New York, 1996.

[18] J. E. Huheey, E. A. Keiter and R. L. Keiter, *Inorganic Chemistry: Principles of Structure and Reactivity, 4th ed.*, HarperCollins, New York, 1993.

[19] K. Holczer *et al.*, Science **252**, 1154 (1991).

[20] W. Koh, D. Dubois, W. Kutner, M. T. Jones and K. M. Kadish, J. Phys. Chem. **97**, 6871 (1993).

[21] M. Baumgarten, A. Gügel and L. Gherghel, Adv. Mater. **5**, 458 (1993).

[22] W. L. Wilson, A. F. Hebard, L. R. Narasimhan and R. C. Haddon, Phys. Rev. B **48**, 2738 (1993).

[23] M. M. Khaled, R. T. Carlin, P. C. Trulove, G. R. Eaton and S. S. Eaton, J. Am. Chem. Soc. **116**, 3465 (1994).

Chapter 7

Future directions

In addition to the ongoing project involving superconducting fullerenes (see Section 6.2), there are a number of projects which I feel have promise, but which I did not have time to complete myself. Below, I list three of these projects. Best of luck to those who attempt them.

7.1 Hysteresis in single-molecule transistors based on single-molecule magnets

In Chapter 4, I mentioned that the reason we were not able to observe hysteresis in SMTs based on Mn_{12} was likely because the Mn_{12} molecules degraded before the tunneling spectra could be recorded. If this were indeed the problem, the most practical solution would be to use a more stable SMM in the experiment. I suggest one use the tetranickel complexes described in reference [1]. These molecules are much more thermally stable than Mn_{12} molecules, and have a relatively large zero-field splitting of roughly 0.5 meV (6 K) in the neutral state. The tetranickel complexes are made in David Hendrickson's group at the University of California, San Diego, which is the same group from which we received our Mn_{12} molecules. Therefore, it should be reasonably easy to procure some tetranickel complexes for a new experiment.

7.2 Ferromagnetic electrodes in N@C_{60}-based single-molecule transistors

Since many experiments in our group make ferromagnetic electrodes with nanoscale gaps using break junctions [2, 3], it might be interesting to study N@C_{60}-based SMTs made with ferromagnetic junctions. Before undertaking such an experiment, one should consider which aspects of the tunneling spectra would be qualitatively different if one switched from noble metal electrodes to ferromagnetic ones.

7.3 Optical experiments

Along with former Ralph group postdoc, Janice Guikema, I did some preliminary work trying to couple a laser beam to the transport in an SMT. There is a recent STM experiment [4] in which a laser was optically coupled to transport through a single-molecule, although in this work it is unclear to me that it was actually the molecule that was optically excited as opposed to the underlying oxide layer. The setup for our experiment is pictured in Figure 7.1. The setup consists of an Ar/Kr laser coupled through an optical microscope into an Oxford optical cryostat. It resides on an optical table in room D-15. These days, is it used mainly by Nathan Gabor in the McEuen group.

There are a number of obstacles to the successful completion of this experiment. I will list them below.

1. I am not exactly sure how the optical coupling will affect the transport spectra of an SMT.

2. Work by Professor Jiwoong Park indicates that the laser light may heat the electrodes in an SMT, raising the temperature at which the experiment

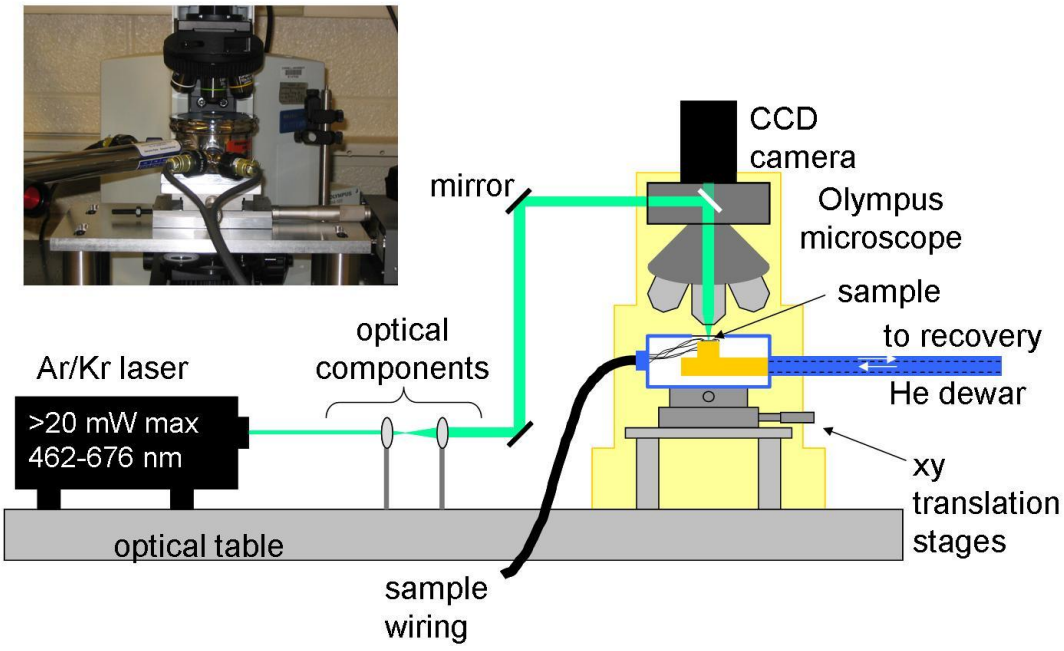


Figure 7.1: Schematic of setup for optical fridge adapted from Janice Guikema. Upper left: digital photograph of setup.

is performed. If the electrodes are gold, then absorption of light increases dramatically at wavelengths above 550 nm. Therefore, if you are using gold electrodes, you must work at wavelengths below 500 nm.

3. When choosing a molecule for this experiment, it must have a strong absorption peak at the wavelengths used in the experiment. C_{70} may be a good choice for such an experiment, as it has a strong absorption peak around 475 nm in toluene, although this peak will shift once the molecule comes in contact with the electrodes. Alternatively, one might try to use PbS nanoparticles in place of molecules, as they are much larger (leading to a larger optical cross section), more stable and have much longer optical lifetimes (between 10 ns and 2 μs in solution). If you purchase PbS nanoparticles from Evident Technologies (the leading nanoparticle supplier), be aware that they come

surrounded by long oleic acid ligands which might significantly suppress the tunneling current.

4. The molecule must be able to absorb enough photons so that photocurrent is generated at sufficient quantities to be detected. The relevant equation is $I_{photo} = \frac{\eta\epsilon(IA)}{hc/\lambda}$, where η is the quantum efficiency, I is the intensity of the incident light and A is the absorption cross section.

5. Most distressingly, when a chip is cooled in the optical cryostat, a layer of ice forms on its surface (see Figure 7.2). This ice layer leads to negative control devices (no molecules) which exhibit Coulomb blockade similar to that in SMTs. Dan and I leak checked the cryostat thoroughly, and it does not appear to have a leak to the outside. Therefore, a component of the fridge must be outgassing moisture. This component is most likely associated with the heater since the ice build-up seems considerably worse when the heater is on. Dan and I contacted Oxford, who (after a lot of cajoling) sent us a new cryostat with a heater which is not attached to the fridge with epoxy (we believed the epoxy to be the source of the outgassing). The new fridge has similar problems, but Dan believes them to be less severe than before and potentially fixable.

If one can get the optical cryostat working, another experiment one might consider has to do with "optical switch" molecules [5]. Optical switch molecules are organic molecules which toggle between a π-conjugated "conductive" form and an unconjugated "insulating" form upon application of different frequencies of light. One problem with such an experiment is that, while optical switch molecules can toggle back and forth in solution, on a metal surface they tend to get stuck in



Figure 7.2: Photographs of ice build-up in the optical cryostat. Upper left: lithography before cooldown. Upper right: lithography at base temperature (around 4 K) with thin layer of ice covering surface. Bottom: lithography during warm-up (around 273 K) with liquid from melted ice on the surface.

one form or the other. Nevertheless, the Abruña group is currently synthesizing optical switch molecules for future study.

REFERENCES

[1] E.-C. Yang *et al.*, Inorg. Chem. **45**, 529 (2006).

[2] A. N. Pasupathy *et al.*, Science **306**, 86 (2004).

[3] K. I. Bolotin, F. Kuemmeth, and D. C. Ralph, Phys. Rev. Lett. **97**, 127202 (2006).

[4] S. W. Wu, N. Ogawa and W. Ho, Science **312**, 1362 (2006).

[5] D. Dulić *et al.*, Phys. Rev. Lett. **91**, 207402 (2003).